Università degli Studi di Ferrara

DOTTORATO DI RICERCA IN
FISICA

CICLO XXX

COORDINATORE Prof. Guidi Vincenzo

Gamma radiation: a probe for exploring terrestrial environment

Dottorando
Dott. Albéri Matteo

(firma)

Tutore
Prof. Mantovani Fabio

(firma)

Anni 2014/2017

Contents

Ringrazio con tutto il mio cuore, Fabio, Ivan, Marica e Virginia e dedico questo lavoro a Sara.

Overview

Radioactivity is a natural phenomenon and has always been present in the environment where the human species has evolved: we get radiation from space, there are radionuclides in the soil we walk, in the air we breathe, in the food we eat and even in our bodies.

Discovered in 1896 by Henri Becquerel, the radioactivity and, in general, nuclear phenomena have been understood by modern physics and have allowed humanity to exploit its potential in multiple contexts (eg. medicine, energetic purpose and weapons). Radioactivity also gave the history of earth an absolute calendar thanks to the measurement of the atoms produced by radionuclide decay inside rocks.

The origin of the primordial natural radionuclides is associated with the supernovae explosions. The terrestrial environment contains several primordial long-lived radioisotopes that have survived to the present in significant amounts, radiation and particles are emitted from natural radioelements and in particular from: ^{238}U (4.5 billion year half-life) ^{232}Th (14.1 billion year half-life) decay through chains of alpha, beta and gamma decays ending at the stable ^{206}Pb, and ^{208}Pb respectively, ^{40}K (1.3 billion year half-life) has the lowest mass of these isotopes and beta decays to both ^{40}Ar and ^{40}Ca. The world average radioactivity content in the upper continental crust is 30, 40 and 720 Bq/kg for ^{238}U, ^{232}Th and ^{40}K, respectively. Energy nuclear technologies, weapons tests during the Cold War and nuclear power plants disasters such as Chernobyl and Fukushima have also added artificial radionuclides to the environment such as ^{137}Cs.

The contribution not originating from the Earth's surface comes from the atmospheric radon (^{222}Rn) one of the intermediate products of the ^{238}U decay chain (3.8 days half-life), and cosmic background originating from the cosmic rays particle (with energies extending up to few 10^{20} eV) interacting with the atmosphere atoms.

One of the most effective methods for conducting radioactivity measurements is gamma-ray spectroscopy. Gamma rays are the most penetrating electromagnetic waves and are extraordinary probes for investigating cosmic, atmospheric and terrestrial sources of radioactivity.

Radioisotopes emit gammas of differing energies, the detector identify an unknown radioisotope by identifying features on the spectrum, this allows to determine the exact radioactive element that has emitted the radiations. Gamma spectroscopy measures can be made *in situ*, with aircraft or in the laboratory with different spatial and spectral resolutions. The typical energies of the Earth's radionuclide emissions are in the order of MeV, this scale fits with the sensibility of inorganic scintillation detector designed for gamma-ray spectroscopy measurements. In particular a type of instrument widely used for these measurements is thallium-doped sodium iodide scintillators (NaI(Tl)), an excellent and versatile detector for gamma ray spectroscopy. Different volumes of these scintillators were used for this research work.

Gamma radiation allows to investigate different regions of the earth with many scientific purposes: my work explores the potential of this measurement technique in different fields. This thesis introduces a calibration of an airborne gamma-ray spectroscopy system, taking into account the uncertainty of flight height, the radiation coming from the space, the atmosphere and the Earth. It also illustrates the application of gamma spectroscopy for geophysical measurements, educational activity and, furthermore, in the field of precision agriculture.

The research activities I carried out during these years have allowed me to come into contact with experts from different disciplinary fields. I participated to conferences in the presence of different community of researchers in the nuclear physics, earth sciences and engineering.

I had the chance to give a talk at A.S.I.T.A.(Federazione delle Associazioni Scientifiche per le Informazioni Territoriali e Ambientali) National Conference in Cagliari and at 103st National Congress of the Italian Physical Society (Trento). On these occasions I had the opportunity to present my work and to get in touch with researchers coming from different disciplines receiving suggestions and helpful feedback on my research activity.

I have improved my educational methods and my communication skills during my tutor teaching activity for the Summer School in Nuclear Physics and Technologies.

The contents of this thesis are included in 5 publications, 4 already published and 1 submitted to scientific peer-reviewed journal. Each part of the thesis represents a different research topic that is explored in detail in its parts and chapters.

Research presented in Part I was developed in the field of Airborne Gamma-Ray Spectrometry (AGRS) a method that allows quantifying the abundances of natural and artificial radionuclides present in the first tens of centimetres of soil surface. AGRS has been used for many years as a lithological mapping tool and particularly as an instrument for uranium exploration. In recent years, however, gamma-ray surveys have come to be used for a broader variety of purposes. For the earth scientist, maps of the concentration of radionuclide, for an environmental physicist, maps of background radiation provide a means to measure the risk to health and a baseline against which man-made contamination can be measured. After a nuclear accident, maps of the fallout pattern are essential for planning emergency responses and for restricting the sale of agricultural produce. The opening of the method to environmental applications (e.g health risks associated with radon in houses) and to the mapping of fallout from nuclear accidents is strictly related to recent developments in multichannel processing methods and the use of statistical methods to reduce noise in multichannel spectra.

In AGRS the interpretation of acquired data requires a correct and aware understanding of the system calibration, acquisition electronics and data processing. The measured airborne gamma-ray spectrum depends from different variables: source geometry, detector characteristic and efficiency, and the distance from the source.

The uncertainty associated with the result obtained by gamma-ray spectrometry depends not only on the uncertainties of the main input parameters but also on different correction factors such as the heights correction to remove the effect of variations in distance from the ground. Attenuation of radiation with distance depends on the geometry of the source and the energy of the radiation.

Airborne gamma-ray spectroscopy measurements are affected by background radiation not originating from the Earth's: cosmic background, instrumental plus aircraft background and atmospheric radon. These contributions has to be quantified and removed during data processing. To model the background spectral components and estimate the effect of the uncertainty of flight height is necessary to perform an off-shore calibration flight at different heights with different altimetric sensors over a wide altitude range. I participated to the airborne measurement campaign and data acquisitions, I worked on setting up the instrument and on its calibration and I post-processed the acquired data.

During my PhD course I studied the application of portable scintillation gamma-ray spectrometer called ZaNaI configured in a backpack for in-situ measurements. *In situ* gamma ray spectrometry is a spectral investigation technique for the identification and quantification of radionuclides present on site. It is an extensively used technique for a wide range of applications from mineral exploration to environmental monitoring purposes. This technique measures directly the gamma radiation originating from an extended source over an area of few tens up to hundreds of square meters giving a quick real-time response.

ZaNaI is composed by a NaI(Tl) crystal with a cubic shape of a volume of 1 liter coupled with a PMT (photo-multiplier tube) base powered by battery and blue-tooth connected with a Smartphone. The instrument needs to be tested under different conditions as it is used in remote areas and must be easy to use thanks to fast connections and interfaces. For this reasons I checked ZaNaI functionality in different conditions: for geochemical purposes and for educational laboratories during the Summer Summer School in Nuclear Physics and Technologies in Ferrara. The results of this work are reported in Part II.

I have been able to apply the experience gained in the range of airborne and *in situ* gamma spectroscopy for precision agriculture applications. The high penetration of the gamma rays permits to study the water content in the soil with a greater sensitivity for the first 20 cm of depth. The variation of water content in the soil changes its overall density and, consequently, its linear attenuation coefficient. For this reason it is possible to estimate the water content in the soil studying the attenuation effects on gamma rays emitted by radionuclides. The gamma ray spectroscopy can provide, with an opportune calibration, a reliable estimation of the volumetric water content. The methods and results of this study are presented in Part III.

Part I

Studying the uncertainty of flight height and background radiation with offshore airborne gamma ray spectroscopy survey

Introduction

During my PhD course my research has been focused on Airborne Gamma-Ray Spectroscopy (AGRS). AGRS is a proximal remote sensing method that allows quantifying the abundances of natural (^{40}K, ^{214}Bi and ^{208}Tl) and artificial (e.g., ^{137}Cs) radionuclides present in the topsoil ($\sim$30 cm depth) over relatively large scales. Studying the spatial distribution of these radionuclides is strategic for monitoring environmental radioactivity [1], producing thematic maps of geochemical interest [2] [3] [4], identifying radioactive orphan sources [5] or investigating areas potentially contaminated by nuclear fallout [6].

Sodium iodide scintillation detectors (NaI(Tl)) are widely employed in AGRS measurements thanks to the high portability and high detection efficiency which allow performing surveys over extended areas in reasonable times and minimizing costs. The frontiers of AGRS and its applications are continuously pushed forward thanks to advances in multichannel processing, statistical methods for spatial resolution enhancement and data analysis procedures [7–10].

The exploration of multidisciplinary fields (e.g. landslide monitoring [11], peat thickness estimation [12], prediction models for trees' growth [13] and precision agriculture [14]), the opening scenario of real time surveys [15–18], the spreading of intercomparison exercises related to multi-regional AGRS campaigns dedicated to the homeland security [19] are a driver for going beyond standard acquisition practices.

The widening of AGRS applications is indeed reflecting in a heterogeneous interpretation of survey methodologies, detector calibration strategies and background radiation sources [20–24].

In the framework of environmental contamination assessment, the detection of artificial radionuclides emitting low energy gamma-rays (e.g. ^{137}Cs and ^{131}I) together with the employment of new unmanned aerial vehicle (UAV) devices, characterized by different detection performances compared to standard acquisition systems, are reawakening the effort in estimating detectors efficiencies and minimum detectable activities (MDA) [25–27].

In order to address the AGRS new challenges, an adequate understanding and knowledge of source of uncertainty (e.g. statistical nature of radioactivity, variable background radiation and the variable water content in soils and geometry of surrounding terrain) is mandatory for processing airborne gamma-ray spectrometric data.

During my PhD course I'm focused on two main topics in the framework of the AGRS: the effect of uncertainty of flight height and his implication on airborne measurements and the effect of background radiation in gamma spectra.

To model the background spectral components of airborne gamma ray measurements and estimate the effect of the uncertainty of flight height is necessary to perform an off-shore calibration flight at different heights with different altimetric sensors: the essential characteristics of these survey are reported in Chapter I. Flight height is a fundamental parameter for correcting the gamma signal produced by terrestrial radionuclides, the estimation of the accuracies of flight altitude, investigating statistical and systematic effects is reported in the Chapter 2.

To predicting the background in the ^{40}K, ^{214}Bi and ^{208}Tl photopeak energy windows originating from the cosmic rays is needed to explore the energies in the range 3-7 MeV to identify signals of pure cosmic origin. The models to describe the cosmic background are presented in Chapter 3. The ^{222}Rn daughter products of ^{214}Pb and ^{214}Bi are are responsible for the measured radon background, the presence of ^{222}Rn in the atmosphere and assessing its vertical profile is reported in Chapter 4.

Chapter 1

Airborne gamma-ray survey and experimental setup

In performing this study I participated to the airborne calibration surveys over the sea dedicated to the measurement of the background gamma radiation and uncertainty of flight height. The campaign consisted of in a series of 5 flights over the Tyrrhenian Sea close to Viareggio Fig 1.1. The data acquisition time is about 5 hours with high statistics measurements in a total range of elevations (35 - 3066) m. I've been involved in the calibration of gamma spectrometers and in the survey planning. In this campaign I have been working on setting up the power supply system and monitoring the acquisition instruments.

I have post-processed the GNSS raw data using dedicated software and I have calibrated the pressure and temperature sensors.

I was involved in statistical analysis of data: I analyzed ∼3 h of data collected over the sea in the (35–2194) m altitude range. I investigated the presence of systematic effects in the altimetric measurements in different altitude ranges.

I contributed to the spectral data analysis, in the treatment of raw list mode data for the conversion to airborne energy calibrated spectra to investigate the AGRS background gamma radiation

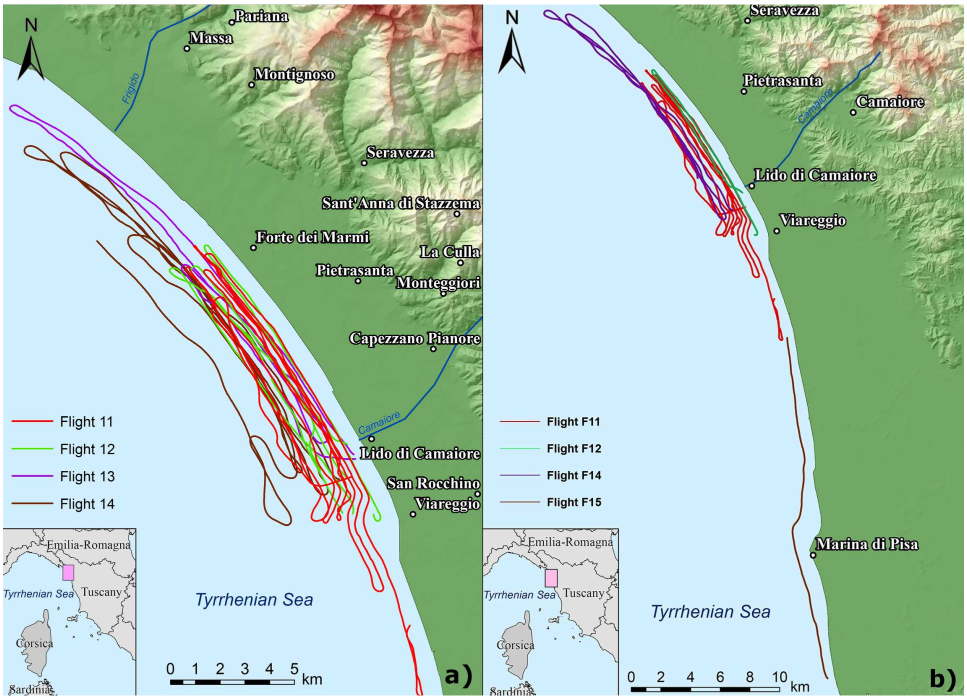

Figure 1.1: map of the effective flight lines of the surveys over the sea performed near Viareggio (Tuscany, Italy) used for cosmic radiation and atmospheric radon background study (panel a) and for estimation of height uncertainty (panel b).

1.1 The aircraft

The aircraft used for the surveys is the Radgyro (Figure 1.2) an experimental autogyro devoted to airborne multiparametric measurements, specifically designed for radiometric survey. The Radgyro is 5.20 m long and 2.8 m high, and has a 83-liter fuel tank placed above the instrumentation to avoid the attenuation of gamma signals coming from the ground due to the interaction with the fuel material. The fuselage has been modified to house the experimental setup for an overall instrumental payload capacity of 120 kg which corresponds to a flight autonomy of approximately 3 hours. Moreover, the Radgyro has two lateral aerodynamic compartments hosting infrared, thermal and visible cameras and an Inertial Measurement Unit (IMU). The Radgyro needs air through its rotor to generate lift so it cannot hover or take off vertically.

Figure 1.2: Radgyro, the autogyro used for described surveys.

1.2 The modular NaI(Tl) scintillation detector

Gamma-ray measurements are performed with a modular NaI(Tl) scintillation detector arranged in the middle of the Radgyro hull, The Airborne Gamma Ray Spectrometer (AGRS_16L), which is made up of 4 4L crystals having dimensions equal to 10 cm × 10 cm × 40 cm [28], for a total detection volume of 16L. Each detector has a 1 mm thick stainless steel shielding and is coupled with a PMT base which receives the voltage supply from a power unit shared among all the sensors mounted on the aircraft. Scintillation light is amplified by means of a 14 pin PMT base whose output signal is processed by a CAEN DT5740 digital pulse charge integrator, a 12 bit 62.5 MS/s waveform digitizer able to provide for 32 separate channels the list mode readout, i.e. an ASCII file for each channel reporting, for each energy deposition inside the specific crystal, the time stamp in units of digitizer clock and the acquisition ADC channel. The PMT high voltage and the gain of the electronics are set in order to acquire gamma-ray spectra for the 4 NaI(Tl) crystals having comparable dynamics and reaching an energy of 7 MeV.

The output list mode files are offline processed in order to generate for each detector gamma spectra corresponding to 1 second acquisition time. For each detector a 600 second spectrum acquired on the ground before the take off is also produced which is used for spectral energy calibration. ^{40}K and ^{208}Tl

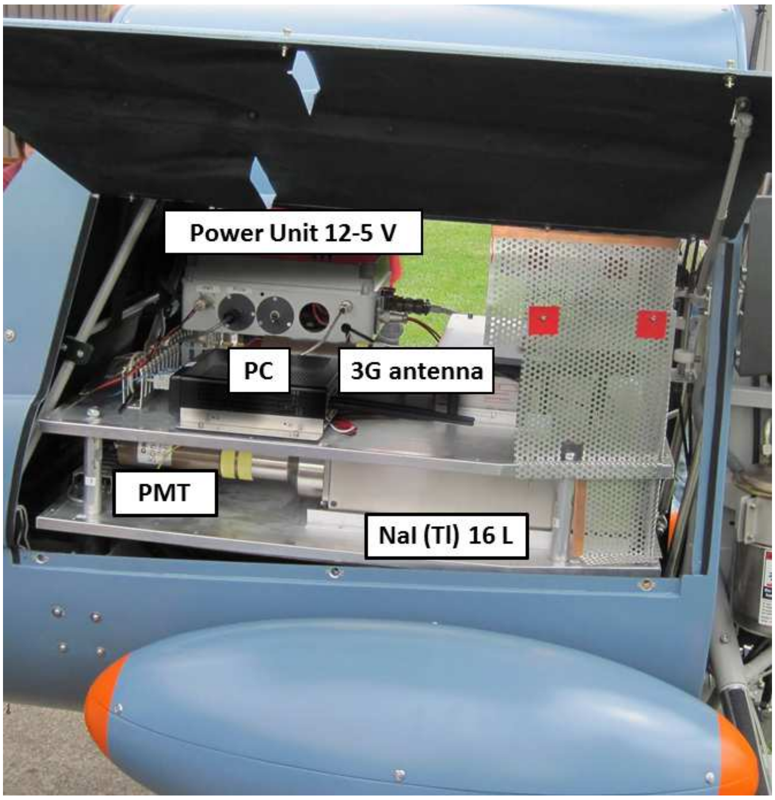

Figure 1.3: the modular NaI(Tl) scintillation detector AGRS_16L, the power unit and the computer hosted in the central region of the aircraft

photopeaks at 1460 keV and 2614 keV are fitted with Gaussian functions whose means are the ADC channels corresponding to the photopeak energies. Once the charge-energy coordinates of the two points have been determined, the slope and intercept of the fitting linear function provide respectively the spectral gain (keV/channel) and the energy corresponding to the first acquisition channel (keV). On the base of the individual linear energy calibration curves, the four 1 second gamma-ray spectra are aligned and summed up in order to obtain the gamma-ray spectrum resulting from the whole 16L detection volume.

Chapter 2

Study of accuracy of flight altitude and his implications in gamma spectroscopy measurements

2.1 Background

A precise evaluation of flight altitude is mandatory for avoiding systematic effects in the gamma signal corrections in AGRS measurements. In the last decade sophisticated analytical techniques based on inverse problem methods [29] as well as Monte Carlo simulations [30] have been proposed for studying Digital Elevation Model (DEM) effect corrections together with corresponding uncertainties in airborne gamma-ray spectrometry. The study presented in this chapter addresses these topics improving the analysis of data collected from seven altimeters and reducing a source of uncertainty like DEM. In particular altitude measurements have been performed with four low-cost GNSS receivers, one radar altimeter and two low-cost barometric sensors in a series of flights over the sea exploring a wide range of altitudes (from 35 to 2194 m; Table 2.1 and Figure 2.1). The goal of this study was to estimate the accuracies of flight altitude, investigating statistical and systematic effects due to calibration methods, post-processing analysis and sensor performances.

Table 2.1: main parameters of the four flights. Hmin and Hmax (minimum and maximum height) refer to the flight height above sea level calculated by averaging the measurements of the different sensors. Average horizontal and vertical speeds are calculated using the data from GPSABC.

Flight ID	Date	Time	H min [m]	H max [m]	Acquisition time [s]
11	30/03/2016	17:42:11 19:29:38	79	2018	6447
12	31/03/2016	18:13:55 18:33:12	129	237	1158
14	05/04/2016	16:37:15 17:33:04	464	2194	3350
15	05/04/2016	19:15:19 19:27:39	35	66	740
Global			35	2194	11695

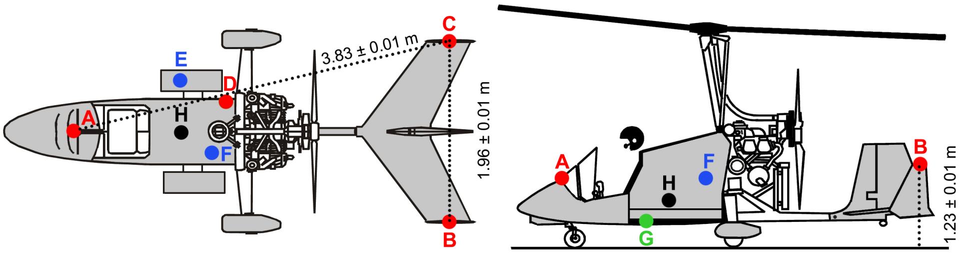

Figure 2.1: scheme of the placement of the different devices on the Radgyro: A) GNSS antenna (GPSA), B) GNSS antenna (GPSB), C) GNSS antenna (GPSC), D) GNSS antenna connected to IMU (GPSIMU), E) pressure and temperature sensors of IMU (PTIMU), F) pressure and temperature sensors (PT), G) radar altimeter (ALT), H) gamma spectrometer NaI(Tl). GPSA, GPSB and GPSC are placed at the following relative distances: dGPSAB = dGPSAC = (3.83 ± 0.01) m and dGPSBC = (1.96 ± 0.01) m.

2.2 Sensors used for the survey: technical features, post processing and calibration methods

The Radgyro is equipped with 7 altimetric sensors, belonging to 3 different instrumental classes: 4 GNSS antennas (GPSABC, GPSIMU), 2 pressure and temperature sensors (PT and PTIMU) and 1 radar altimeter (ALT) (Figure 2.1). In this study the height of Radgyro is referred to the GNSS antenna locations, which are located at the same vertical position with respect to the ground (1.08 ± 0.01 m). Taking into account that the radar altimeter accuracy is of the order of 3 % of the measured altitude, the difference in distance from the ground between ALT and GNSS antennas (0.71 m) is negligible. The pressure sensors are calibrated using the GNSS and therefore the barometric altitude is referred to GNSS antenna position.

2.2.1 The Inertial Measurement Unit (IMU)

The right lateral compartment of the Radgyro houses the Inertial Measurement Unit MTi-G-700 GPS/INS (IMU) (Figure 2.1), which is equipped with a GNSS receiver acquiring the GPS signal with a maximum frequency of 4 Hz, a barometer providing the atmospheric pressure readout with a maximum frequency of 50 Hz (PTIMU) and inertial sensors retrieving the roll, pitch and yaw angles with a maximum frequency of 400 Hz. The IMU provides height values by combining the data from the GNSS, the barometer and the accelerometers with a maximum frequency of 400 Hz (GPSIMU). Dynamic and barometric measurements allow for height estimation even with weak GNSS signal and the nominal accuracy on the vertical position is 2 m (1σ) [31].

2.2.2 The radar altimeter

The Smartmicro ® Micro Radar Altimeter (ALT), placed under the Radgyro fuselage (Figure 2.1), measures the flight altitude at $\sim$ 60 Hz by using a radar sensor operating at a frequency of 24 GHz. The estimate of the minimum distance is declared reliable within a cone having 20° opening angle and the declared accuracy on altimetric measurements is 33 % , with a minimum value of 0.5 m. Although the flight altitude range declared by the seller is (0.5 - 500) m, the data analysis on the ALT dataset revealed a significativer presence of outlier at heoghts above 340 m (Figure 2.2). Neglecting effects related to wave motions and tidal variations, which are typically <0.4 m in the surveyed area [32], in this study two different datasets named α and β are considered, corresponding respectively to H <340 m and H >340 m respectively. The α database is populated by data acquired in 4803 seconds by all 7 sensors, while the β database refers to the remaining 6892 seconds in which the ALT sensor is excluded (Table 2.2).

Figure 2.2: a typical situation of flight over the sea with Radgyro

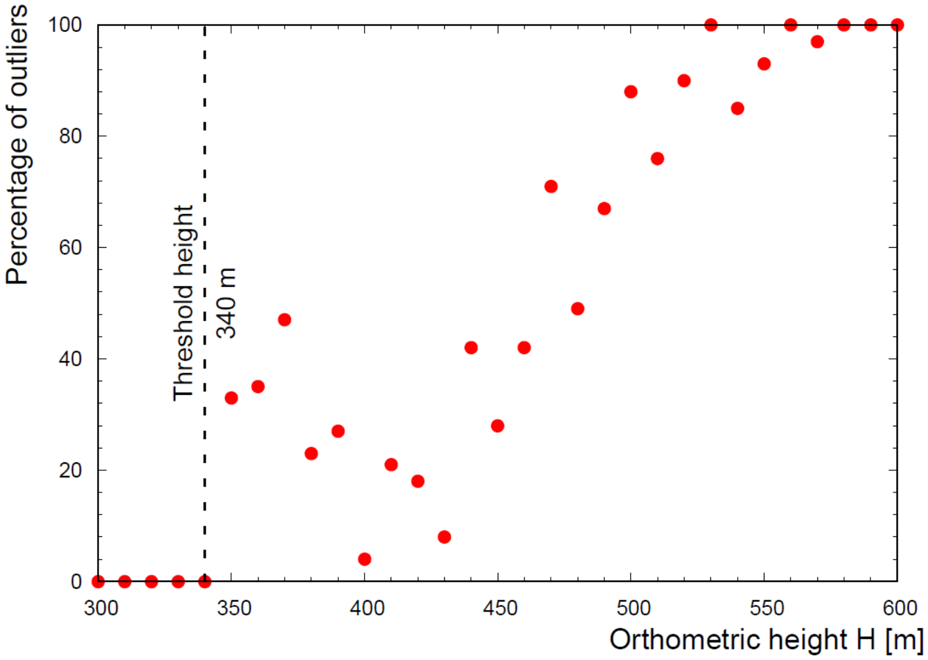

Figure 2.3: percentage of outliers in the ALT dataset as a function of the orthometric height. The altitude of 340 m has been identified has a threshold above which the ALT dataset has been excluded from the global analysis

2.2.3 The three GNSS receivers

The Radgyro is equipped with 3 single frequency u-blox EVK-6 receivers each of them coupled with a GPS ANN-MS active antenna having 100 g weight and dimensions equal to 48 mm × 40 mm × 13 mm, one located on the aircraft cockpit (GPSA) and the others on the tail wings (GPSB and GPSC) (Figure 2.1). A low noise amplifier is implemented on each receiver which is intended to compensate the loss of signal due to cables and connectors. Each GPS receiver is able to directly deliver a real-time solution, using NMEA GGA sentences, and raw data to be post-processed in standard RINEX format, both with a sampling frequency of 1Hz. Moreover, the logging software records the GPS acquisition time coupled with the absolute computer time in order to correctly synchronize GPS with the other sensors present onboard. GPS raw observations were post-processed following two different analyses with the open source goGPS software [33]

- code-only stand-alone solution (1 Hz), using a Kalman filter with constant-velocity dynamics;
- code and phase double differences solution (0.2 Hz) with respect to the permanent station Madonna Dell'Acqua (Pisa) (43.747° 5 N, 10.3660° E, 2 a.s.l), using a Kalman filter with constant-velocity dynamics.

These different methods produce two datasets that that are defined as DATASET 1 and DATASET 2 at 1 Hz and 0.2 Hz respectively (metti tabella datasets). The orthometric heights are calculated using the EGM2008 global geoid model [34]. The identification of GNSS data outliers has been performed by studying the distribution of the distances reconstructed between the three GPS antennas dGPSAB, dGPSAC, dGPSBC with respect to reference values (Figure 2.1). Following [35], an outlier is a data point that lies out of the ranges (Q1 − 1.5 IQR) and (Q3 + 1.5 IQR), where Q1, Q3 and IQR are first quartile, third quartile and interquartile range respectively. Outlier data have been typically recognized when flying close to the sea (Figure 2.1) and at an altitude range of [35 - 900] m (Figure 2.5 and 2.7). The analysis of outlier highlights that their percentage generally decreases with increasing altitude and that the median dGPSBC, dGPSAC and dGPSAB approach the reference distances. We note that in F15 the dGPSAB erraticity decreases drastically crossing the border between sea and land (Figure 2.4). The average reconstructed dGPSAB varies from (5.86 ± 7.18) m (over water) to (3.77 ± 0.28) m (over land), to be compared with the (3.83 ± 0.01) m reference distance. In F15, characterized by a (35 – 66) m flight altitude range, it is possible to observe a noise amplification due to the multipath effect over the sea. This phenomenon is well known in literature and has been studied in different environmental scenarios [36], investigating also applications like the monitoring of coastal sea levels and of the periodicity of ocean tides [37] [38] [39].

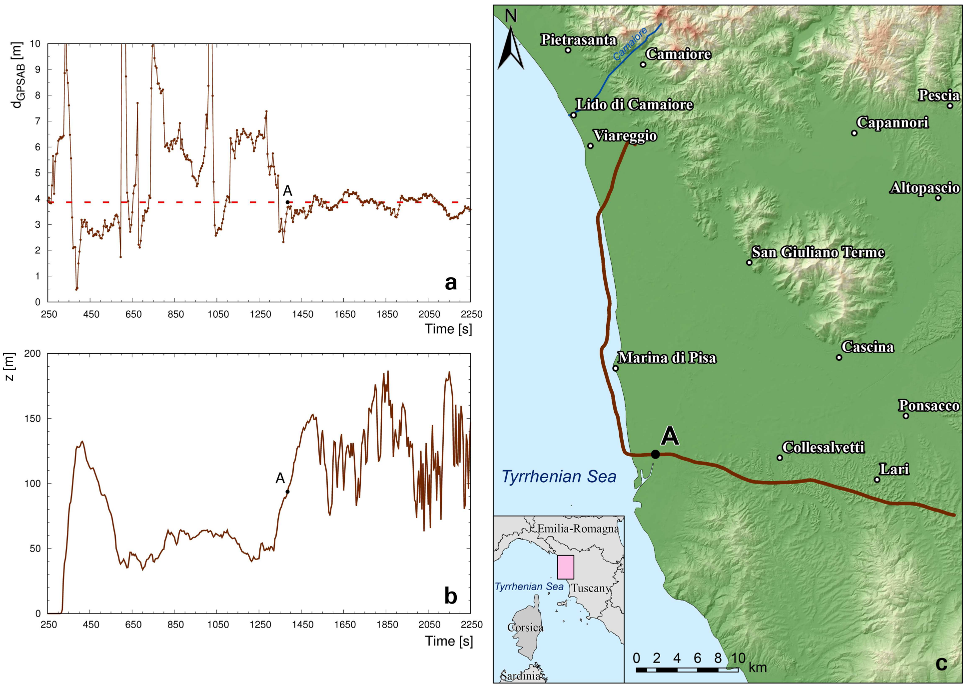

Figure 2.4: a) Reconstructed distance between GPSA and GPSB as a function of time during a portion of F15. The dashed red line represents the (3.83 ± 0.01) m reference distance and the brown line represents the average reconstructed dGPSAB during the flight. The large fluctuations observed in the reconstructed distance when flying over the sea are strongly reduced when flying over land, in particular when flying more than 3 km far from the coast (point A). b) Mean height above the ground level z[m] (digital elevation model is subtracted) measured by GPSABC.

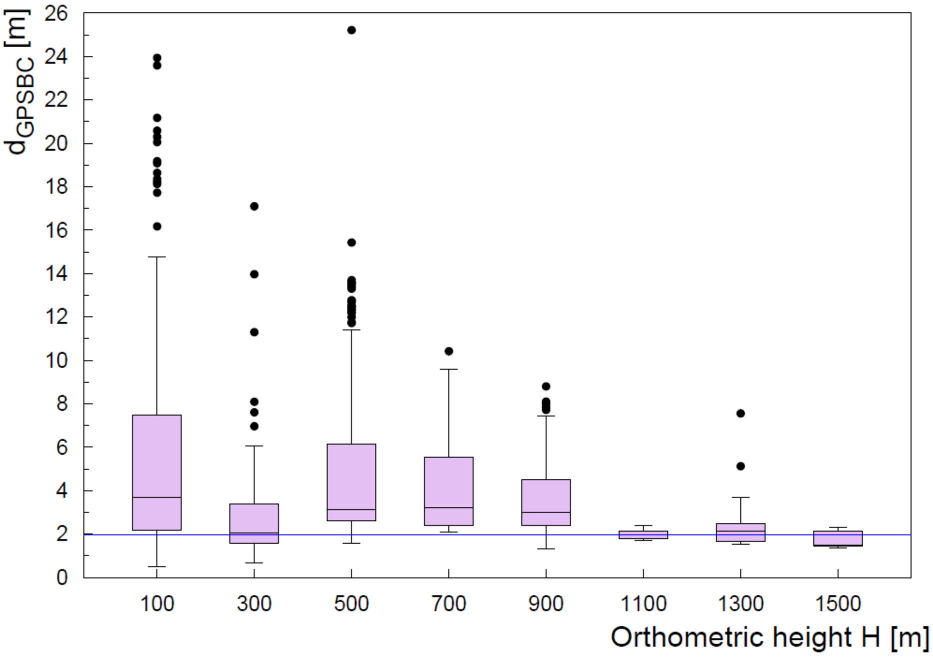

Figure 2.5: boxplot of the distribution of dGPSBC as a function of the orthometric height H for entire 0.2 Hz dataset. The blue line represents the (1.96 ± 0.01) m reference distance between GPSB and GPSC. Black points represent outlier data.

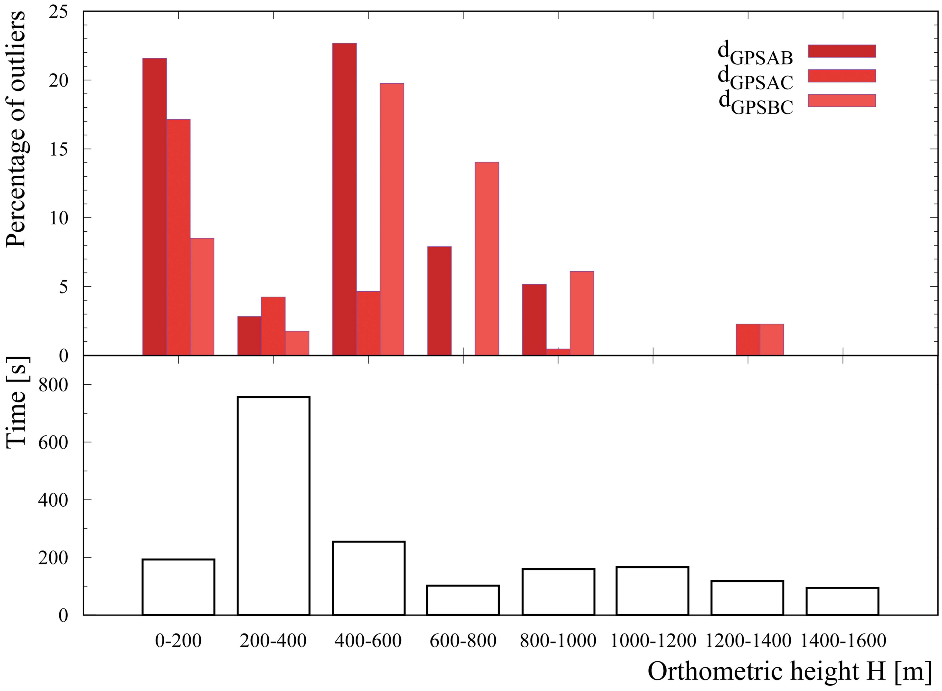

Figure 2.6: in the upper panel are shown the percentages of outliers identified in the dGPSAB, dGPSAC and dGPSBC datasets as a function of the orthometric height H. In the bottom panel are displayed the temporal statistics as a function of the orthometric height.

2.2.4 The two pressure and temperature sensors

The Toradex Oak USB Sensor Atmospheric Pressure (PT), hosted inside the Radgyro fuselage (Figure 2.1), acquires with a sampling frequency of 2 Hz the temperature and pressure with a 10 Pa resolution (corresponding to approximately 0.8 m in height) and a ± 2° C accuracy, respectively. The pressure and temperature datasets provided by both the PT and the PTIMU devices have been processed by applying the hypsometric formula, which allows estimating the orthometric heights HPT and HPTIMU on the basis of the decreasing exponential trend of the atmospheric pressure with respect to the altitude and accounting for the tiny variations of the temperature in the lower atmosphere:

$$H_{PT} = \frac{T_0}{L}\left[\frac{P(H)}{P_0}^{\frac{-LR}{g}} - 1\right] \tag{2.1}$$

GOCE-based geopotential model described in [40], R = 287.053 J/(kg K) (gas constant for air), T_0 is the temperature at sea level (K), P_0 is the pressure at the sea level (Pa) and L = ΔT/ΔH = $-6.5 \cdot 10^{-3}$ K/m (temperature lapse rate), constant below 11 km orthometric height [41]. Thanks to the fact that PT and PTIMU are located respectively inside the Radgyro fuselage and inside one lateral compartment (Figure 2.1), it has been possible to investigate how the Radgyro dynamics affects the pressure readout of both devices, which can be influenced by variations in the air fluxes, by the aircraft velocity as well as by depressions caused by the rotor motion, especially during the take off stage (Figure 2.7). Barometric altimeters are not able to provide absolute height without a prior knowledge of the local sea level pressure P_0. A calibration of the pressure at sea level P_0 is necessary in order to take into account the variation of air fluxes related to the Radgyro dynamics as well as possible variations of the atmospheric conditions during the flight [42]. The calibration of PT and PTIMU has been performed applying the inverse hypsometric formula (Eq.2.1), where HPT is obtained by averaging the heights measured by GNSS receivers and ALT (at altitude less than 340 m) during 120 s of flight. This interval is chosen on the base of general agreement among sensor data, minimizing the standard deviations during the flight. Since F11 and F14 are characterized by longer acquisition times, this process has been applied during the flight in two different separated intervals. After these calibrations an internal consistency check shows that all systematic discrepancies of altitude measured by PT and PTIMU have been removed. The successful correction is confirmed by the excellent agreement between HGPSABC and HPT data (Figure 2.8).

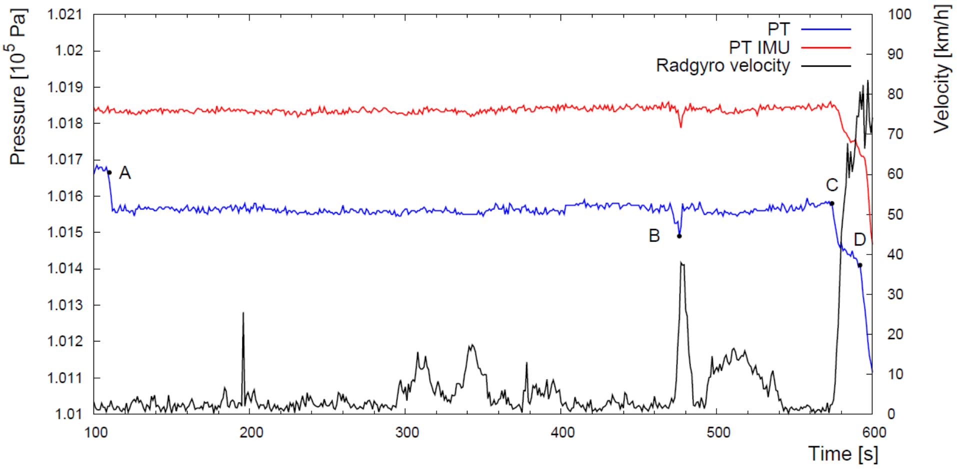

Figure 2.7: temporal profile of the pressure measured by PT (in blue) and PTIMU (in red) not calibrated, and of the Radgyro horizontal velocity (in black) before the take-off. When the back screw is turned on, the PT sensor most exposed to the air flux measures a depression (point A). The pressure variation registered by both sensors in B is due to short increase of velocity during the taxiing. The accelerating run along a runway starts in C and in D the aircraft takes off.

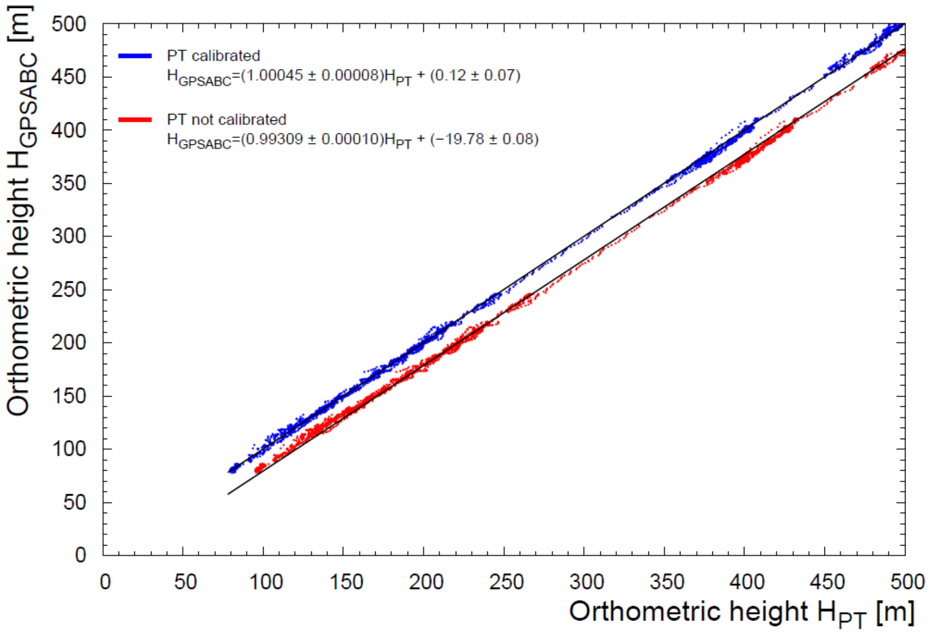

Figure 2.8: linear regression between HGPSABC and HPT data for F11. In blue and red are reported the calibrated and not-calibrated barometric data respectively. The black straight lines are the linear fits to data: in both cases $r^2 = 0.999$.

2.3 Result and discussion

This section discusses the comparison and the accuracy of the orthometric heights derived by GNSS, radar altimeter and barometers. The metric adopted is based on the root mean square RMS(δH^J) of the discrepancy between H^J measured by the J-th sensor and the averaged height obtained from all the sensors:

$$RMS(\delta H^J) = \sqrt{\frac{\sum_{i=1}^{N} (\delta H^J{}_i)^2}{N}} \tag{2.2}$$

where N is the total numbers of data. For each i-th measurement obtained by J-th sensor, the residual around the mean δH^J is given by:

$$\delta H^J = H^J{}_i - \overline{H^J} \tag{2.3}$$

where $\overline{H^J}$ is the average height measured by M sensors:

$$\overline{H_i} = \frac{\sum_{J=1}^{M} H^J{}_i}{M} \tag{2.4}$$

Note that correlations among observations are here ignored, e.g. those derived from the fact that the GNSS receivers practically "see" the same set of satellites. Moreover, the M available sensors are assumed to have the same accuracy in the combination of Eq. 4. Comparing RMS(δH^J) with the mean of the residuals of the J-th sensor:

$$\overline{\delta H}^J = \frac{\sum_{i=1}^{N} \delta H^J{}_i}{N} \tag{2.5}$$

it is possible to highlight potential systematic biases related to the J-th sensor dataset, which can be distinguished from the variance of the residuals on the base of the following relationship:it is possible to highlight potential systematic biases related to the J-th sensor dataset, which can be distinguished from the variance of the residuals $\sigma^2(H^J)$ on the base of the following relationship:

$$RMS(\delta H^J) = \sqrt{\sigma^2(H^J) + \left(\overline{\delta H}^J\right)^2} \tag{2.6}$$

where $\sigma^2(H^J$ is defined as:

$$\sigma^2(H^J) = \frac{\sum_{i=1}^{N} \left(\delta H_i^J - \overline{\delta H}^J\right)^2}{N-1} \tag{2.7}$$

This metric allows emphasizing the systematic height shift related to a specific sensor dataset with respect to the dispersion of values around the average height (see Table 2.3 and Table 2.4). In other words from Eq. 6 we learn that when the $RMS(\delta H^J) \approx |\overline{\delta H}^J|$ then $RMS(\delta H^J) \ll |\overline{\delta H}^J|$ i.e. the measurement is affected by a systematic bias which dominates the dispersion of data $\sigma(H^J)$. With the perspective of evaluating an overall uncertainty on the height measurement for airborne gamma ray applications, the distribution of standard deviations $\sigma_i(H)$ for each i-th entry of the dataset are calculated:

$$\sigma_i(H) = \sqrt{\frac{\sum_{J=1}^{M} \left(H_i^J - \overline{H}_i\right)^2}{M-1}} \tag{2.8}$$

The analysis has been performed on 4 different datasets (Table 2.1), which have been distinguished according to a spatial selection cut and a GPS processing method cut, corresponding respectively to the 340 m altimeter outlier cutoff and to the 0.2 Hz frequency double-differences dataset of GPSA, GPSB and GPSC post-processing, as described in section 2.2 and section 2.3.

2.3.1 DATASET 1

The main results of the analysis of the 1 Hz stand-alone DATASET 1α and 1β (Table 2.2) are summarized for each sensor in Table 2.3 in terms of average of the residuals δH^J and of the root mean square of the residuals $RMS(\delta H^J$.

Table 2.2: number of entries of the datasets used in the analysis of the orthometric height values from GNSS, altimetric and barometric measurements. The 340 m height cutoff has been identified on the base of altimeter outlier data, the 0.2 Hz frequency is related to the availability of the Madonna Dell'Acqua master station data for the GNSS post-processing.

		α (H < 340 m)	β (H > 340 m)
DATASET 1	1.0 Hz (stand-alone)	4803	6892
DATASET 2	0.2 Hz (double-difference)	960	1378

Table 2.3: average residuals δH and $RMS(\delta H^J)$ for data acquired at 1Hz in the range [35 - 340] m (DATASET 1α) and in the range [340 – 2194] m (DATASET 1β)

DATASET 1 α														
	GPSA [m]		**GPSB** [m]		**GPSC** [m]		**GPSIMU** [m]		**ALT** [m]		**PTIMU** [m]		**PT** [m]	
	$\overline{\delta H}$	RMS	H	RMS	$\overline{\delta H}$	RMS	$\overline{\delta H}$	RMS	$\overline{\delta H}$	RMS	$\overline{\delta H}$	RMS	$\overline{\delta H}$	RMS
F11	-0.1	1.8	0.7	2.7	0.4	1.9	0	1.7	0	1.5	-0.8	1.7	-0.2	1.4
F12	-0.2	1.8	-0.1	2.1	0.2	2.3	0.8	1.4	-0.7	2.9	0	1.9	0.1	2
F15	1.9	2.3	0.5	2.1	1.7	2.5	5.8	5.9	-3.2	3.3	-4.1	4.3	-2.7	3
DATASET 1 β														
	GPSA [m]		**GPSB** [m]		**GPSC** [m]		**GPSIMU** [m]		**ALT** [m]		**PTIMU** [m]		**PT** [m]	
	$\overline{\delta H}$	RMS	H	RMS	$\overline{\delta H}$	RMS	$\overline{\delta H}$	RMS	$\overline{\delta H}$	RMS	$\overline{\delta H}$	RMS	$\overline{\delta H}$	RMS
F11	0.4	2.5	0.6	2.1	1.3	2.1	-1.4	2.3	/	/	-0.8	2	-0.1	1.6
F14	0.7	1.7	1	2	1.5	2.2	-3.1	3.4	/	/	-0.2	1.5	-0.1	1.7

The poor accuracy of data from GNSS at low altitude mentioned in section 2.3 is confirmed in this analysis. In particular, for H < 66 m (F15) there is not only a dispersion of values, but also a clear systematic shift of altitude measured by this class of sensors with respect to those obtained by radar and barometric altimeters. This evidence shows that the multipath effect at low altitude produces severe interferences for cheap GNSS receivers. In the range [79 – 340] m the agreement among values of altitude measured by all 7 sensors is good (Figure 2.10). The median of the distribution of standard deviations is 1.7 m and the values of δH^J reported in Table 2.3 do not highlight any significant systematic effect (i.e. $\delta H^J < 1$m). Finally in the range [340 - 2194] m the median of the distribution of standard deviations is 2.1 m. The comparison of different values of δH^J calculated for GNSS receivers seems to show two clusters of data characterized by positive and negative values of δH^J for GPSABC and GPSIMU respectively. This feature is evident in Figure 2.9 where the values closest to zero for PT and PTIMU highlight how these barometric sensors give the best performance when they are calibrated with redundant measurements from GNSS receivers.

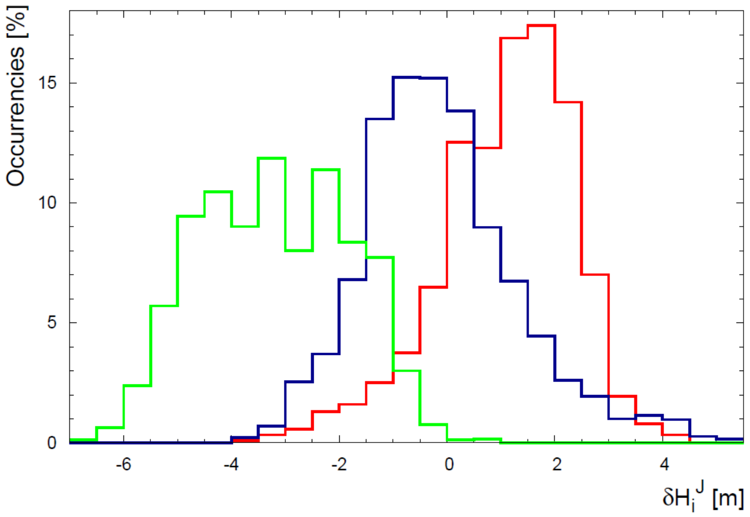

Figure 2.9: distribution of the residuals in the [464 - 2194] m range of altitude: GPSIMU dataset in solid green line, PTIMU and PT dataset is reported in solid blue line, and GPSABC dataset in solid red line.

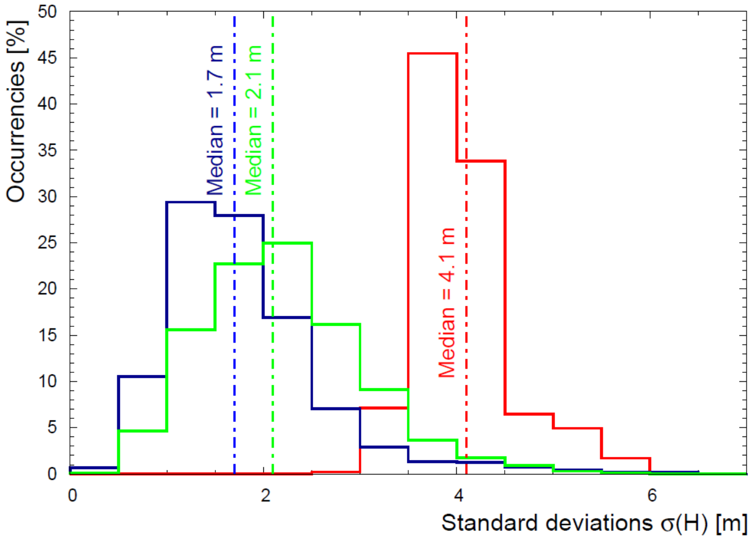

Figure 2.10: distribution of $\sigma(H)$ (standard deviations of heights) in the range [35 – 66] m (red solid line), [79 – 340] m (blue solid line) and [340 – 2194] m (green solid line) measured at 1 Hz.

2.3.2 DATASET 2

In this section the analysis of the 0.2 Hz double-difference DATASET 2α and DATASET 2β is presented, in which the GPSA, GPSB and GPSC acquisitions have been post-processed using the double differences method with respect to the master station observation data. PT and PTIMU are calibrated with the criteria described in section 2.4 using the GNSS double-difference data. The double differences post-processing increases the quality of GPSA, GPSB and GPSC data which reflects in a shrinking of the $\sigma_i(H)$ distribution towards low standard deviation values at altitude [79 – 2194] m (Figure 2.11 Panel b), making the median value of the distribution decrease from 1.5 m (stand-alone) to 0.8 m (double-differences). It is possible to notice that the major benefit of the data treatment affects the GPSABC accuracy at high altitude [340 - 2194] m, where the values of $\overline{\delta H}^J$ are comparable to those obtained for [79 – 340] m (i.e. $\overline{\delta H}^J$ < 1m) (Table 2.3). On the basis of $\overline{\delta H}^J$ and $RMS(\delta H^J)$ calculated in Table 2.4 it is possible to assert that double differences post-processing does not produce any evident improvement of the altitude accuracy at H < 66 m (Figure 2.11 Panel a). The severe multipath noise which affects the calculation of relative distances between the three GPS antennas and the altitude measured at 1 Hz, is not healed by double-differences post processing at heights lower than 66 m. On the other hand, the non-GNSS sensors give excellent results in terms of linear correlation and negligible systematic effects. Observing linear regression data in (Table 3 for PT, PTIMU, and ALT the slope and the intercept are compatible with 1 and 0 at 2σ-level respectively. The performance of all sensors in the altitude range [79 – 2194] m is essentially similar: the $RMS(\delta H^J)$ varies from 1.3 m to 2.5 m and the maximum $\overline{\delta H}^J =$ 1.6 m (Table 2.3). The distribution of standard deviation of heights reported in Figure 2.12 does not show any peculiar feature: for ranges of altitude of [79 – 340] m and [340 – 2194] m the median is 1.6 m and 1.5 m respectively. In particular the Pearson correlation coefficients calculated for all the couples of sensors highlight perfect linear correlation in [340 – 2194] m range of altitude (Tables 4 and 4 in appendix C).

Table 2.4: average residuals δH and $RMS(\delta H^J)$ for for DATASET 2)

	GPSA [m]		**GPSB** [m]		**GPSC** [m]		**GPSIMU** [m]		**ALT** [m]		**PTIMU** [m]		**PT** [m]	
DATASET 2 α														
	$\overline{\delta H}$	RMS	H	RMS	$\overline{\delta H}$	RMS	$\overline{\delta H}$	RMS	$\overline{\delta H}$	RMS	$\overline{\delta H}$	RMS	$\overline{\delta H}$	RMS
F11	-0.5	1.9	0.6	1.8	-0.2	1.9	0.2	1.9	0.2	1.3	-0.5	1.8	0.1	1.4
F12	-0.2	1.7	0	1.4	0.2	1.6	1.1	1.5	-0.5	2.5	0.2	1.6	-0.8	1.8
F15	2.1	2.4	0	1.7	0.4	1.1	6.8	6.9	-2.4	2.5	-3.8	4.1	-3.1	3.6
DATASET 2 β														
	GPSA [m]		**GPSB** [m]		**GPSC** [m]		**GPSIMU** [m]		**ALT** [m]		**PTIMU** [m]		**PT** [m]	
	$\overline{\delta H}$	RMS	H	RMS	$\overline{\delta H}$	RMS	$\overline{\delta H}$	RMS	$\overline{\delta H}$	RMS	$\overline{\delta H}$	RMS	$\overline{\delta H}$	RMS
F11	0.1	2.3	0.6	1.3	0.9	1.7	-0.1	1.3	/	/	-1.4	2.4	-0.1	1.6
F14	0.6	1.3	0.4	1.3	0.6	1.3	-1.6	2	/	/	-0.1	1.3	0.1	1.7

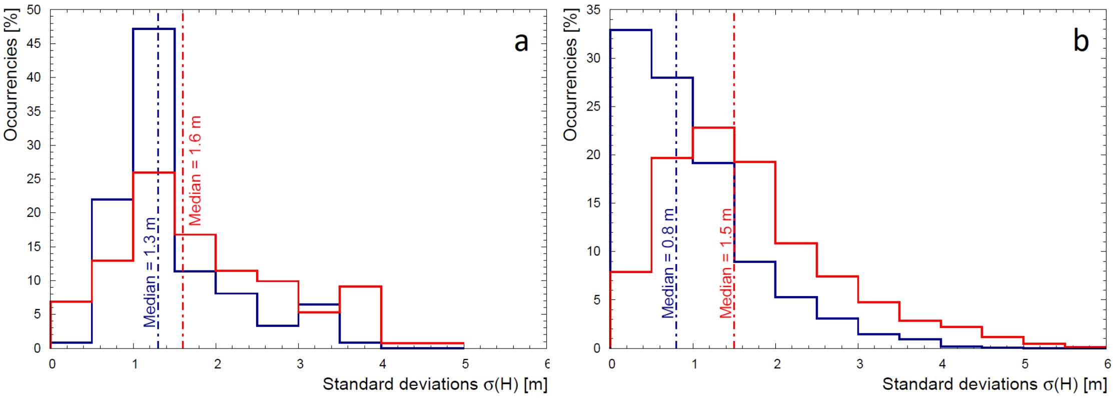

[H]

Figure 2.11: distribution of $\sigma(H)$ (standard deviations of heights) calculated for GPSABC built-in solution (red solid line) and with double-difference post-processing (blue solid line), in the altitude ranges [35 - 66] m (panel a) and [79 - 2194] m (panel b).

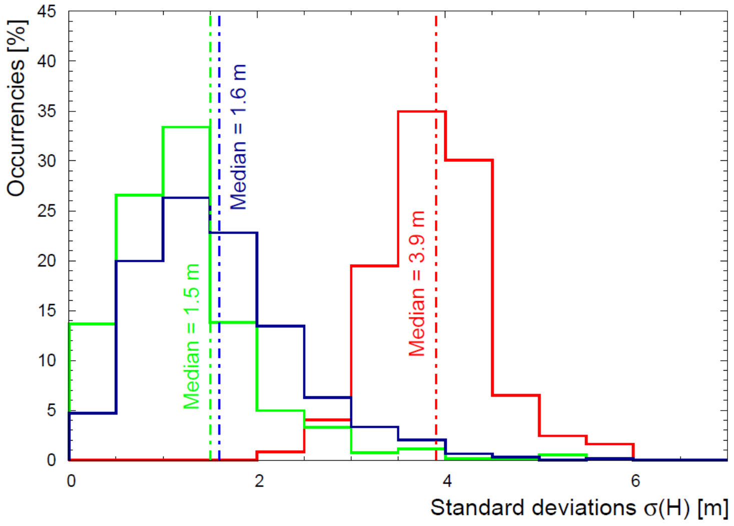

[H]

Figure 2.12: distribution of $\sigma(H)$ (standard deviations of heights) in the altitude ranges [35 – 66] m (red solid line), [79 – 340] m (blue solid line) and [340 – 2194] m (green solid line) measured at 0.2 Hz.

2.4 Effect of the accuracy of the flight altitude on AGRS measurements

In airborne gamma-ray spectroscopy measurements, knowing the survey altitude above the ground is of crucial importance in order to model the exponential attenuation photons having different characteristic energies suffer when traversing the air material. This aspect has implications on the determination of the height correction factors which are separately calculated for each radionuclide in order to reconstruct the counting statistics at ground level in case of flat morphology. In fact, neglecting possible systematic uncertainties originating from the calibration of the instrumental setup, the main source of uncertainty in AGRS measurements is related to the counting statistics, which result from the statistical nature of both radioactive decay and photon attenuation in traversing materials.

The count rate measured in a given energy window by a detector that is flying at altitude z above ground level and which originates from a homogenous infinite half-space soil volume source is given by the following equation:

$$N(E,z) = \frac{A_\gamma S}{\mu_s(E)} \int_0^1 dcos\theta e^{\frac{-\mu(E)z}{cos\theta}} \tag{2.9}$$

where A_γ is the density of photons isotropically emitted by the homogeneous volume source $[\gamma/m^{-1}]$, S is the detector cross-sectional area $[m^2]$, $\mu_s(E)$ $[m^{-1}]$ and $\mu(E)$ $[m^{-1}]$ are the soil and air linear attenuation coefficients, corresponding to the inverse of the mean free path traveled by a photon having energy E and traversing the soil and air materials, respectively. Starting from 2.9 it is possible to write the following relation between the count rate measured at altitude z N(E,z) and the count rate that one would have measured by placing the detector on the ground N(E,0):

$$N(E,z) = N(E,0)k(\mu(E),z) \tag{2.10}$$

where the function $k(\mu(E),z)$ is given by:

$$k(\mu(E),z) = \int_0^1 dcos\theta e^{\dfrac{-\mu(E)z}{cos\theta}} \tag{2.11}$$

Gamma-ray spectrometers typically undergo a ground efficiency calibration procedure for the determination of the sensitivity constants, which allow for the conversion of measured count rates into ground radionuclide abundances. The ^{40}K, ^{238}U, ^{232}Th ground abundances are therefore predicted by dividing the estimated ground level count rate N(E,0) by the specific ground sensitivity constant, which represents the count rate per unit radioisotope concentration. In the hypothesis of negligible uncertainty on the sensitivity constants, the relative uncertainty on the ground abundance is equal to the relative uncertainty affecting the counting statistics N(E,0), inferred from the measured N(E,z) according to 2.10. We therefore apply the standard propagation of uncertainty for uncorrelated variables to the quantity N(E,0) in order to estimate the contribution given by the uncertainty on the survey altitude σ_z to the ground concentration estimation, which can be expressed according to the following equation:

$$\sigma_N(E,0)^2 = \left(\left|\frac{\partial N(E,0)}{\partial N(E,z)}\right|\sigma_k(\mu(E),z)\right)^2 + \left(\left|\frac{\partial N(E,0)}{\partial k(\mu(E),z))}\right|\sigma_k(E,z)\right)^2 = \tag{2.12}$$

$$\left(\left|\frac{\partial N(E,0)}{\partial N(E,z)}\right|\sigma_N(E,z)\right)^2 + \left(\left|\frac{\partial N(E,0)}{\partial k(\mu(E),z))}\right|\left|\frac{\partial k(\mu(E),z)}{\partial z}\right|\sigma_z\right)^2 \tag{2.13}$$

Starting from the inverse of 2.10 it is possible to determine all the terms of 2.12 as follows:

$$\left|\frac{\partial N(E,0)}{\partial N(E,z)}\right| = \frac{1}{k(\mu(E),z))} \tag{2.14}$$

$$\sigma_N(E,z) = \sqrt{N(E,z)} \tag{2.15}$$

$$\left|\frac{\partial N(E,0)}{\partial k(\mu(E),z)}\right| = \frac{N(E,z)}{k(\mu(E),z)^2} \tag{2.16}$$

$$\left|\frac{\partial k(\mu(E),z)}{\partial z}\right| = \int_0^1 dcos\theta e^{\frac{-\mu(E)z}{cos\theta}} \tag{2.17}$$

where the absolute uncertainty on the observed counting statistics given by 2.15 comes from the Poissonian nature of the radioactive decay process. By combining all the obtained terms into 2.12 it is possible to write the relative uncertainty on the inferred ground counting statistics as the sum of two terms as stated in the following equation:

$$\left(\frac{\sigma_{N(E,0)}}{N(E,0)}\right)^2 = \left(\frac{\sigma_{N(E,z)}}{N(E,z)}\right)^2 + (\beta(\mu(E),z)\mu(E)\sigma_z)^2 = \tag{2.18}$$

$$\left(\frac{\sigma_{N(E,z)}}{N(E,z)}\right)^2 + \left(\mu(E)\sigma_z\frac{\int_0^1 dcos\theta\frac{1}{cos\theta}e^{\frac{-\mu(E)z}{cos\theta}}}{\int_0^1 dcos\theta e^{\frac{-\mu(E)z}{cos\theta}}}\right)^2 \tag{2.19}$$

The first term in the summation corresponds to the relative uncertainty on the measured counting statistics, while the second term contains the product of the absolute height uncertainty σ_z times the air linear attenuation coefficient $\mu(E)$ which is in turn weighted by an adimensional factor $\beta(\mu(E),z)$ that depends on the linear attenuation coefficient itself and on the absolute survey height z. The $\beta(\mu(E),z)$ function contains an energy dependence as the attenuation suffered by photons is stronger for decreasing energy (i.e. the $\mu(E)$ linear attenuation coefficient decreases for increasing energy) and has also a z dependence according to which, for a fixed energy, the value of $\beta(\mu(E),z)$ decreases for increasing height asymptotically approaching 1. Figure 2.13 shows the profile of the $\beta(\mu(E),z)$ function for the characteristic emission energies of ^{40}K, ^{214}Bi and ^{208}Tl (see Table 2.6), the profile of the relative uncertainty $\frac{\sigma_{N(E,0)}}{N(E,0)}$ as function of $\sigma_{z)}$ (is show in Figure 2.14. The adopted values for the linear attenuation coefficient ($\mu(E)$) are show in Table 2.5.

Table 2.5: values for the $\mu(E)$ gamma linear attenuation coefficients for gamma photons propagating in air. These values have been estimated using an air density of 1.225 kg/m^3 and gamma mass attenuation coefficients taken from the National Institute of Standard and Technology website [43], where an air composition of 78% N_2, 21% O_2 and 1% Ar by weight has been given for the description of the composite traversed material.

Nuclide	**Energy [keV]**	**Linear-Attenuation Coefficient in Air $\mu(E)$ $[m^{-1}]$**
^{40}K	1460	0.00643
^{214}Bi	1765	0.005829
^{208}Tl	2614	0.004717

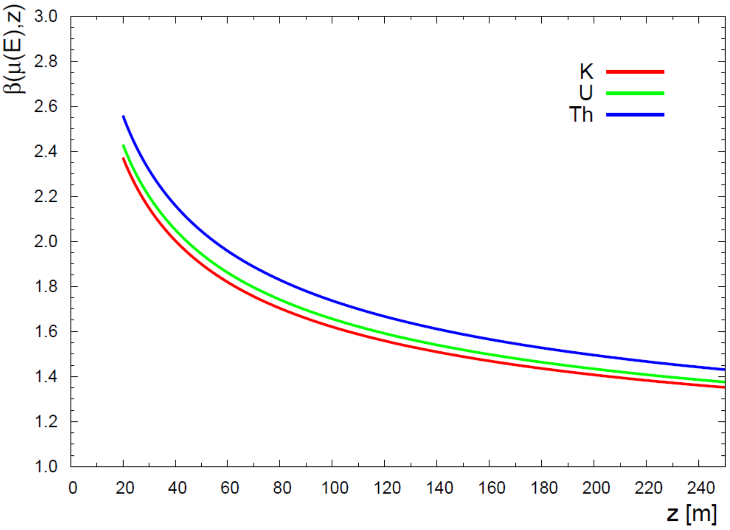

Figure 2.13: plot of the $\beta(\mu(E), z)$ factor as function of the survey altitude z: the red, green and blue line refer respectively to the ^{40}K, ^{214}Bi (^{238}U) and ^{208}Tl (^{232}Th) gamma emission energies.

Considering a NaI(Tl) detector having a volume of 16L described in Chapter 1.2 and flying at a height of 100 m over a terrain characterized by K, U and Th abundances respectively equal to 0.02 g/g, 2.5 μg/g and 9.0 μg/g, the statistics in counts per second (cps), recorded in the three energy windows typically used to quantify the content of the three radionuclides 2.6 are respectively (103.2 ± 10.2) cps, (12.4 ± 3.5) cps and (26.5 ± 5.1) cps, where the uncertainty is estimated according to the Poisson distribution describing the nature of the radioactive decay.

Table 2.6: typical energy intervals for gamma ray spectrometry in environmental [44]

Radioisotope	Daughter nuclide	Photopeak energy [keV]	Region Of interest [keV]
Potassium	^{40}K	1460	1370 – 1570
Uranium	^{214}Bi	1765	1660 - 1860
Thorium	^{208}Tl	2614	2410 - 2810

Assuming that the uncertainty on the height above ground level is exclusively given by the uncertainty on the orthometric height (i.e. neglecting any contribution that can potentially arise from the Digital Elevation Model (DEM) of the terrain) it is possible to estimate by choosing as σ_z the 2.1 m median value of the standard deviation distribution of DATASET 1β for [340 - 2194] m that the relative uncertainty on the ^{40}K, ^{238}U, ^{232}Th ground abundances at 100 m are 2.2%, 2.0% and 1.7% respectively, which result only from the uncertainty on the height above the ground (i.e. neglecting the uncertainty on the counting statistics $\left(\frac{\sigma_{N(E,0)}}{N(E,0)}\right) = 0$).

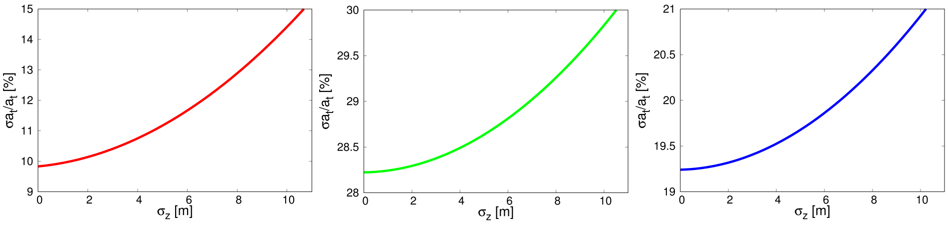

Figure 2.14: plot of the percent relative uncertainty $\frac{\sigma_{N(E,0)}}{N(E,0)}$ on the counting statistics as function of the uncertainty of flight height $\sigma_{z)}$ (for z=100 m): the red, green and blue line refer respectively to the ^{40}K, ^{214}Bi (^{238}U) and ^{208}Tl (^{232}Th) gamma emission energies.

2.5 Final remarks

During radiometric surveys, it is common to measure the altitude from different sensors operating simultaneously on board of the aircraft. This chapter shows how this redundancy can improve the quality of flight height accuracy and the implication on the correction of gamma signal for estimating the K, Th and U ground abundances. Since the increasing use of UAV in airborne gamma ray spectroscopy implies necessarily lower altitude fight regimes together with reduced payload and power consumption, the performances of 7 altimetric sensors are analysed: 3 single frequency GNSS light antenna, 1 IMU coupled to a GNSS antenna, 2 barometric sensors and 1 radar altimeter. In the range [35 - 66] m the altitude measured by GNSS antennas suffers the severe noise due to the multipath effect which is significant when flying over the sea. Even after a double differences post-processing, the median of the distribution of standard deviations of heights is 1.3 m (Figure 2.9 Panel a). This observed erraticity is confirmed comparing the distances reconstructed between GPS antennas A and B (dGPSAB = 5.86 ± 7.18 m) with its reference value (dGPSAB = 3.83 ± 0.01 m). Crossing the border between sea and land a significant reduction of this effect permits to estimate a value of (3.77 ± 0.28) m in agreement at 1σ level with the reference distance. Although the IMU sensor provides the flight altitude by combining the data from the GNSS, the barometer, and the accelerometers, the values of and are greater than 5 m, highlighting how the external correction is not effective in mitigating the noise due to the multipath GPS signal. On the base of this study, it is possible to conclude that the most accurate measurement of flight altitude over the sea in the range [35-66] m has been performed by two barometric altimeters together with the radar altimeter. In this altitude regime the linear regressions (Table 3 in appendix B) show slopes and intercepts compatible with 1 and 0 at 2σ-level, and the median of the distribution of standard deviations of heights is 1.1 m. Adopting this altitude error at 50 m, the relative uncertainties on the ^{40}K, ^{238}U, ^{232}Th ground abundances are equal to 1.3%, 1.2% and 1.1% respectively. According to this investigation the reliability of radar altimeter is in agreement with its declared accuracy (3% of the altitude value) up to 340 m: beyond this height the number of outliers increases drastically, preventing the inclusion of these data for the comparative analysis. In the range [79 - 340] m the median of the distribution of standard deviations of altitude acquired by all the 7 sensors is 1.6 m, with double differences post-processing of the signal recorded by three single frequency GNSS antennas. Adopting conservatively this uncertainty for a 100 m flight altitude, is it possible to estimate a relative uncertainty of 1.7%, 1.5% and 1.3% associated to ^{40}K, ^{238}U, ^{232}Th ground abundances respectively. At altitude higher than 79 m, the GNSS double-difference post-processing enhanced significantly the data quality obtained by the 3 cheap and light antennas. This is proved by a reduction of the median value of the standard deviations (from 1.5 m with stand-alone analysis to 0.8 m with double-difference processing) and by an increasing precision in the reconstruction of median distance of the three antennas with increasing altitude. Since the computation of double differences does not solve the multipath problem, the use of better performing antennas with size and cost compatible with AGRS survey is strongly recommended. At altitude higher than 1000 m where the radar and barometric altimeters can provide data affected by relevant bias, the height estimated by GNSS sensors is the most reliable. Finally with the perspective of an increasing diffusion of cheap, light and real-time airborne gamma-ray surveys it is suggested to increase the quality of the altitude evaluation by means of redundant complementary sensors based on different acquisition methods. According to this study, the best integration of data from GNNS antennas, radar and barometric altimeters allows reaching an accuracy better than 2% at flight altitude higher than ∽80 m, which affect the estimation of ground total activity measured at 100 m with an uncertainty resulting from the sole uncertainty on the flight height of the order of 2%.

The content of this chapter is based on the following publication:

Alberi M., Baldoncini M.,Bottardi C., Chiarelli E., Fiorentini G., Raptis K.G.C., Realini E.,Reguzzoni M., Rossi L., Sampietro D., Strati V., Mantovani F.“*Accuracy of flight altitude measured with cheap GNSS, radar and barometer sensors: implications on airborne radiometric surveys*” Sensors (Basel) (2017) 17(8), 1889. DOI: 10.3390/s17081889. (IF: 2.964)

Chapter 3

Study of background gamma radiation originating from cosmic rays

3.1 Background

Airborne gamma-ray spectroscopy measurements are affected by background radiation, which can be considered as radiation not originating from the Earth's surface and which has to be removed during data processing. The three major sources of background radiation are cosmic background, instrumental plus aircraft background and atmospheric radon (^{222}Rn) (see Chapter 4).

Galactic cosmic ray particles, with energies extending up to few 10^{20} eV [45, 46], are produced outside the Solar System and are constituted by a nucleonic component (98%) and electrons (2%). The nucleonic component is primarily made up by protons (∼85% of the flux) and alpha particles (∼12%), with a remaining fraction comprising heavier nuclei [47]. In entering the Earth's atmosphere, these particles collide with atoms of air constituents, giving rise to cascades of secondaries, including neutrons, pions, muons and gamma radiation. In airborne gamma-ray spectroscopy counts collected in the range 3-7 MeV allow to identify the gamma component of cosmic rays, as the end point of gamma-rays of terrestrial origin corresponds to the ^{208}Tl emission at 2.614 MeV. This information can be used not only for predicting the cosmic background in the ^{40}K, ^{214}Bi and ^{208}Tl photopeak energy windows, but also for assessing the cosmic radiation dose to the human population.

The annual effective dose rate due to cosmic ray exposure averaged over the world's population has been estimated to be 0.38 mSv/y by [47], although recent efforts have been done in order to give more accurate evaluations on the base of advanced cosmic-ray fluxes calculation and refined grid databases of population and terrain elevation models [48]. These estimations take into

Table 3.1: summary of the main parameters for each of the 4 surveys over the sea. For each flight the ID, date, time, minimum and maximum altitude and acquisition time are reported, respectively. In the case of flights 11 and 14, 83 seconds and 30 seconds have been cut due to some radiofrequency interference between the PMT and the aircraft transponder. The long interruption of the data taking of flight 12 (2531 seconds) has been imposed by civil traffic of the Pisa airport.

Flight ID	Date	Time	z min [m]	z max [m]	Acquisition time [s]
11	30/03/2016	17:42:10 19:29:43	77	2019	6370
12	31/03/2016	18:13:55 19:46:47	126	2070	3041
13	05/04/2016	11:39:53 12:28:36	348	1144	2924
14	05/04/2016	16:37:16 18:05:43	461	3066	5277
Global			77	3066	17612

account the amount of time people spend indoor (80% of the day) and the mean thickness of the walls acting as a shield for the cosmic radiation. Cosmic dosimetric measurements are generally focused on the assessment of air crew members exposure. There are also regional measurement campaigns addressing the question of outdoor population dose exposure [49–51]. In this context, the calibration of an airborne gamma-ray detector for the assessment of cosmic dose rates can provide a supplementary technique for the cosmic exposure assessment with respect to in-situ measurements.

This section presented the results of a ∼5 hours AGRS survey over the sea dedicated to the measurement of the gamma radiation originating from the aircraft materials and cosmic rays, which constitute a background source for the estimation of the gamma radiation of terrestrial origin coming from ^{40}K, ^{214}Bi (eU) and ^{208}Tl (eTh). The AGRS non-geological background radiation is investigated with 17612 1 second measurements in a wide range of elevations (77-3066) m. The acquisition of spectra over water at a number of different heights indeed provides a way to split the constant contribution coming from the radioactivity of the aircraft from the height dependent contributions associated with cosmic radiation and, if present, with atmospheric radon [52]. Moreover, it is studied a linear calibration curve which allows to convert count rates into the electromagnetic shower component of the cosmic effective dose (CED$^{\mathrm{EMS}}$) based on two cosmic ray dosimetry software tools: CARI-6P [53] and EXPACS [54]. A procedure for the calculation of cosmic effective dose to human population (CED) is finally proposed.

According to the purpose of the experiment, the flight paths have been

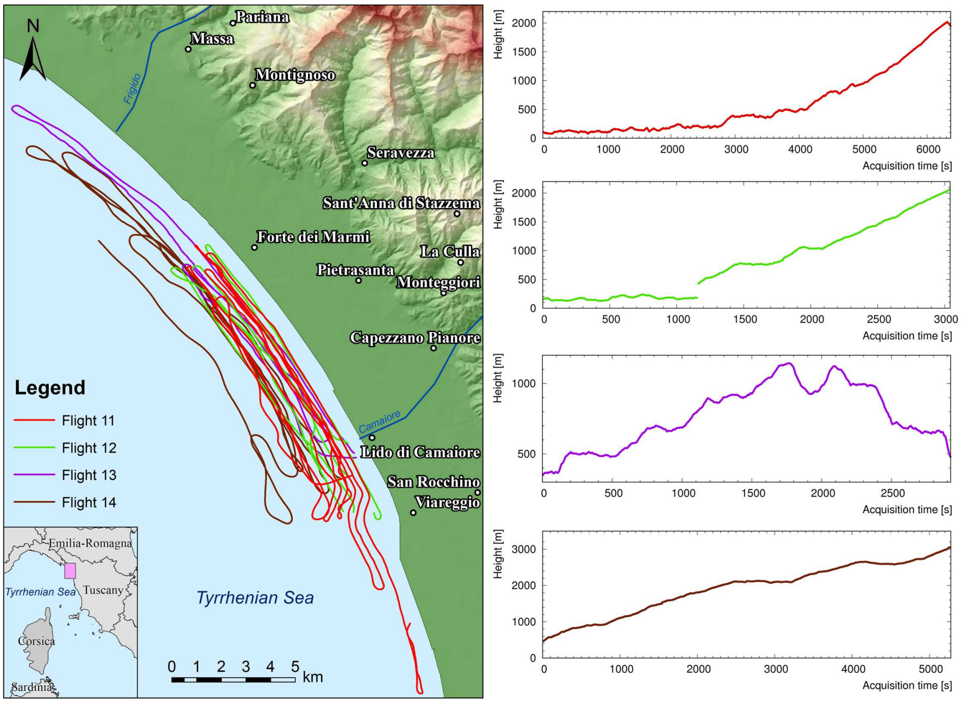

Figure 3.1: the left panel shows a map of the effective flight lines of the surveys over the sea 1). The acquisition tracks are the ones corresponding to data points acquired at a minimum distance from the coast of 300 m. The four panels on the right show the altitude profiles for the different flights.

planned with the aim of investigating the entire reported range of heights with enough statistics for well constraining the analysis of the altitude dependent gamma-ray cosmic component. This strategy, together with the flight conditions and the non feasibility for the Radgyro to hover at a given elevation, allowed us to collect the elevation flight statistics shown in Fig. 3.2.

3.2 Theoretical modeling and data analysis

The cosmic gamma background resulting from the interaction of cosmic secondary radiation interaction with the air, the aircraft and the detector materials is foreseen to monotonically increase with increasing altitude. Concerning the energy dependence, the cosmic-induced gamma-ray energy spectrum is expected to have a polynomial dependence with respect to gamma-ray energy [23]. The count rate (CR) energy dependence of the cosmic component is reconstructed according to a polynomial function having the following expression:

$$CR(E) = aE^b + c \tag{3.1}$$

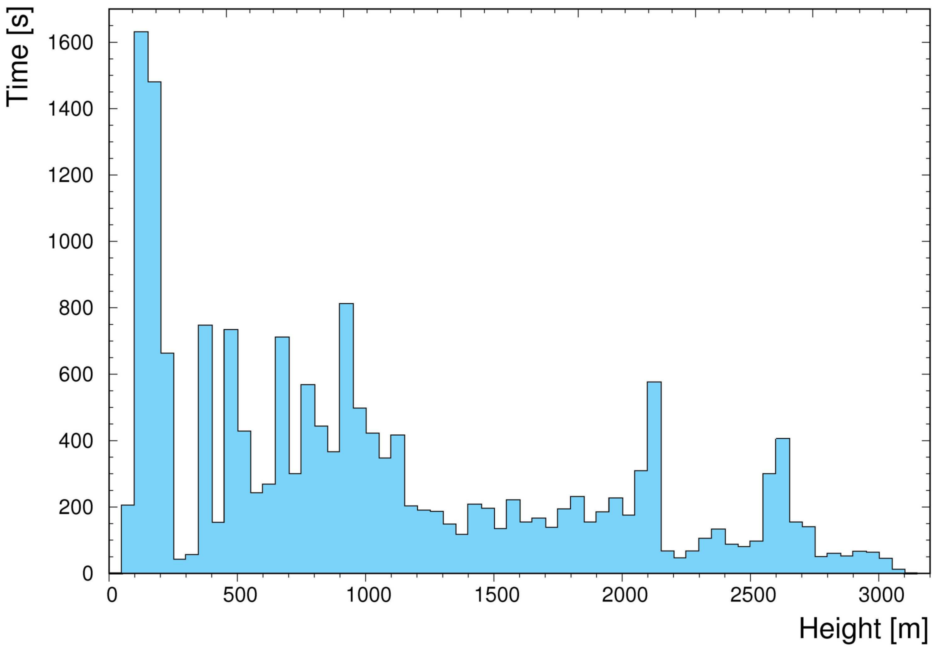

Figure 3.2: histogram describing the effective overall temporal statistics: the data taking time at a given survey altitude is shown, with an altitude binning of 50 m.

where E is the gamma-energy in MeV and a, b and c are constants for a spectrum measured at a given altitude. The energy dependence of the CR has been estimated by fitting the measured spectrum with the above model function both in the 0.8-7 MeV energy range and in the 3-7 MeV energy range, called respectively the Full Energy Window (FEW) and the Cosmic Energy Window (CEW). A third fit has been performed using as input data points the measured CRs in the CEW, plus the three points corresponding to the estimated CRs due to cosmic radiation in the ^{40}K, ^{214}Bi and ^{208}Tl photopeak energy windows (see Table 3.3), which have been determined on the base of the linear regression parameters reported in Table 3.5.

In Table 3.2 the results of this analysis in two different ranges of altitudes is reported. In both cases radiometric data have been acquired above 2000 m, where the presence of atmospheric radon is negligible (see Section 4). Fig. 3.3 shows an example of background airborne gamma-ray spectrum measured with the AGRS_16L together with the three curves resulting from the different fitting procedures. From this exercise it is possible to evince that the fitting of the measured spectrum is dependent on the energy range chosen, as the spectral shape under reconstruction contains different pieces of information in the CEW and in the FEW. Using only the CEW for constraining the cosmic spectral shape from one side assures the pure cosmic nature of the counting statistics, but on

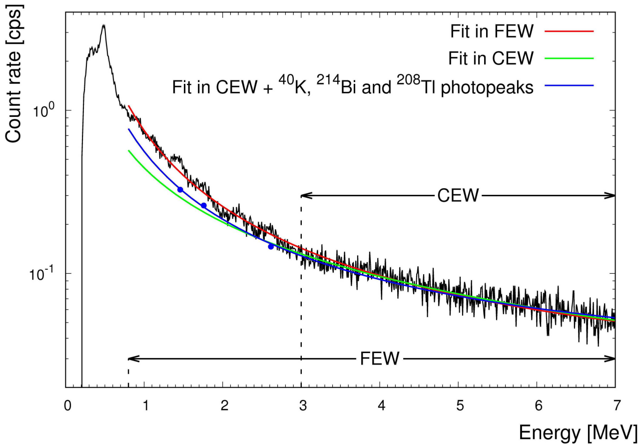

Figure 3.3: gamma-ray spectrum composed of 870 1 second spectra acquired in the elevation range 2050-2150 m (black solid line). The red solid line shows the fitting curve obtained using as model function Eq. 3.1 and as energy fitting range the FEW, the green solid line shows the curve obtained by fitting the measured spectrum in the CEW. The blue points correspond to the CRs in the KEW, BEW and TEW associated with the cosmic induced background and obtained on the base of the linear relation having as parameters the ones reported in Table 3.5. The blue solid line is the result of the fit of the measured spectrum in the CEW and of the blue points.

the other side the sole reconstruction of the spectral high energy tail prevents a correct estimation of the curve slope in the low energy range as emphasized by the large uncertainties on the best fit parameters. By fitting in the FEW the steep behavior at low energies is reproduced: however in this case the measurement under reconstruction contains not only the cosmic contribution to the signal, but also the signal coming from the equipment radioactivity and in particular from the ^{40}K, ^{214}Bi and ^{208}Tl decay series. On the other hand, the idea behind the third fitting approach is to reinforce the fit performed by using the sole count rates in the CEW with the addition of three relatively well separated points corresponding to the cosmic CRs in the ^{40}K, ^{214}Bi and ^{208}Tl photopeak energy windows. Among the above mentioned three strategies this is the one providing the most reliable estimation of the cosmic spectral shape in the FEW.

Instrumental and aircraft background correspond to the constant gamma signal generated by trace amounts of K, U and Th contained in the detector materials and ancillary equipment, together with the aircraft material itself. ^{222}Rn, the only gaseous daughter product of the ^{238}U decay chain, can escape from rocks and soils and, considering its 3.8 days half-life, can accumulate in the lower atmosphere. Its gamma-emitting daughter nuclei ^{214}Bi and ^{214}Pb can attach to airborne aerosols and dust particles, giving rise to the atmospheric

Table 3.2: fit parameters of the CR energy dependence modeled with Eq. 3.1 for two spectra measured at 2100 m and 2650 m for respectively 870 seconds and 550 seconds. For each measured spectrum the fit has been performed in the FEW, in the CEW and in the CEW plus the ^{40}K, ^{214}Bi and ^{208}Tl photopeaks.

z range [m]	Fit energy range	(a ± δa) [cps]	b ± δb	(c ± δc) [cps]
2050 - 2150	FEW	0.73 ± 0.10	-1.62 ± 0.40	0.02 ± 0.03
	CEW	0.44 ± 0.42	-1.11 ± 1.60	0.00 ± 1.40
	CEW + ^{40}K, ^{214}Bi and ^{208}Tl photopeaks	0.54 ± 0.04	-1.49 ± 0.05	0.02 ± 0.01
2600 - 2700	FEW	0.90 ± 0.11	-1.53 ± 0.33	0.02 ± 0.04
	CEW	0.62 ± 0.61	-1.14 ± 1.66	0.00 ± 1.87
	CEW + ^{40}K, ^{214}Bi and ^{208}Tl photopeaks	0.71 ± 0.05	-1.45 ± 0.03	0.02 ± 0.01

Table 3.3: energy windows for natural and cosmic radiation used for the background calibration of the AGRS_16L system. The last two columns report for each energy window the measured CR for gamma-ray spectra acquired at the altitude range 2050-2150 m and 2600-2700 m, respectively.

Energy Window	Emission line [keV]	Energy range [keV]	Measured CR [cps] (2050 - 2150) m	Measured CR [cps] (2600 - 2700) m
KEW	1460	1370 - 1570	12.2	15.0
BEW	1765	1660 - 1860	8.7	11.1
TEW	2614	2410 - 2810	8.8	11.9
CEW	/	3000 - 7000	41.9	54.8

radon background gamma signal [55]. The determination of the K, U and Th ground concentrations during an airborne gamma-ray survey relies on the estimation of the background corrected CRs recorded in the ^{40}K, ^{214}Bi (eU) and ^{208}Tl (eTh) photopeak energy windows, called KEW, BEW and TEW, respectively (see Table 3.3).

Aircraft and cosmic background calibration flights are usually performed offshore for a typical altitudes range of (1500 - 3000) m above the ground level in order to avoid the contamination from terrestrial radiation and radon decay products [56]. In this scenario, as the instrumental background is supposed to be constant and the gamma cosmic background is expected to exponentially increase with increasing height, the measured CRs in the $i'th$ energy window during a calibration flight over the sea is predicted to follow the subsequent equation:

$$n^i(z) = A^i e^{\mu^i z} + B^i \tag{3.2}$$

where n^i is the CR in the $i'th$ energy window (with i = KEW, BEW, TEW and CEW) A^i, μ^i and B^i are constants [52, 56].

The CR in the natural radionuclides energy windows are expected to be linearly related to the count rate in the CEW, as stated in the following equation:

$$n^i = a^i + b^i n^{\text{CEW}} \tag{3.3}$$

where n^i is the CR in the $i'th$ energy window (with i = KEW, BEW, TEW), a^i is the aircraft background CR in the $i'th$ energy window, b^i is the cosmic stripping ratio (i.e. the cosmic background CR in the $i'th$ energy window normalized to unit counts in the CEW) and n$^{\text{CEW}}$ is the CR in the CEW. The parameter a^i is the expected CR for null cosmic CR and therefore represents the constant background component generated by the Radgyro and by the detectors materials. Determining these linear functions for the natural radionuclides energy windows allows to correct the CRs measured at a given height during regional AGRS surveys for the aircraft and height dependent cosmic ray backgrounds, provided the monitoring of the CR in the CEW.

Eq. 3.2, as well as Eq. 3.3, holds in the absence of any terrestrial and atmospheric radon radiation component. A potential radon contamination in any case would act on the CRs in the KEW and BEW but not on the CRs in the TEW and CEW as they are not affected by the lower energy gamma emissions of radon daughter nuclei. The presence of a radon background component in the measured CRs can be generally identified as a breakdown of the linear relationship between the cosmic and the ^{214}Bi CRs at low elevations (see Chapter 4). The estimated CRs in the energy windows of interest have been clustered according to an altitude binning of 15 m, which is conservative with respect to the estimated accuracy on the vertical position resulting from the combination of all the altimeters present on board of the Radgyro 2. The CRs used as input for the background modeling are therefore estimated summing all the input CRs acquired in the same elevation bin and dividing by the number of 1 second spectra entering the summation.

The parameters of the exponential curves A^i, μ^i and B^i have been determined via the minimization of the χ^2 function:

$$\chi^2_{\text{exp}} = \sum_{j=1}^{\text{nbin}} \left[\frac{n^i_j - \left(A^i e^{\mu^i z_j} + B^i \right)}{\sigma_{n^i_j}} \right]^2 \tag{3.4}$$

where nbin is equal to the number of elevation bins entering the χ^2 minimization, n^i_j is the average CR obtained for the $j'th$ elevation bin in the $i'th$ energy window, z_j is the average elevation obtained for the $j'th$ elevation bin and $\sigma_{n^i_j}$

is the 1 sigma uncertainty associated to the counting statistics, corresponding to the square root of the total counts recorded at z_j in the $i'th$ energy window divided by the acquisition time at z_j.

The objective χ^2 function to be minimized for determining the linear curve parameters has instead to be built taking into account not only the statistical error associated to the quantity n^i but also the uncertainty on the "independent variable" $\mathrm{n}^{\mathrm{CEW}}$. Therefore, the adopted definition for the χ^2 function is:

$$\chi^2_{\mathrm{lin}} = \sum_{j=1}^{\mathrm{nbin}} \frac{\left[n^i_j - \left(a^i + b^i n_j^{\mathrm{CEW}}\right)\right]^2}{\left(\sigma_{n^i_j}\right)^2 + \left(b^i \sigma_{n_j^{\mathrm{CEW}}}\right)^2} \tag{3.5}$$

Monitoring the CEW in principle can be used for estimating the CED to human population. Gamma-ray spectrometers for dosimetric measurements are generally calibrated by exposing them to certified radiation fields, which can be collimated beams at irradiation facilities, calibrated radioactive point sources with known activities covering both high and low energy ranges or calibration pads generally made of concrete and doped with radionuclides of known gamma dose-rates [57–59].

In the last decades various codes devoted to the calculation of the aircraft crew's exposure to cosmic radiation have been developed on the base of Monte Carlo techniques, analytical solutions and empirical data fitting [60–62]. Since most of them are user friendly and well tested, their adoption for the calibration of an AGRS detector for cosmic dose estimation can be a valid option with respect to traditional characterization procedures. The popular software CARI-6P allows to calculate the different components of the cosmic effective dose received by an individual at typical cruise altitudes by relying on analytic calculations of particle transport through the atmosphere [53]. The EXcel-based Program for Calculating Atmospheric Cosmic ray Spectrum (EXPACS) dosimetry tool permits to model the fluxes of different cosmic particles in the lower atmosphere thanks to air shower simulation performed by Particle and Heavy Ion Transport code System (PHITS) [54].

Both codes require information on the altitude, the geographic location and the time period, the latter related to changes in the Earth's magnetic field and in solar activity. Since the count rate in the CEW measured by a gamma spectrometer during a calibration flight is related to the electromagnetic shower ($\mathrm{CED}^{\mathrm{EMS}}$), knowing the temporal and spatial coordinates of the survey it is possible to characterize a calibration curve, which depends on the detector and on the dosimetry software tool. Once the calibration parameters have been calculated, subsequent AGRS acquisitions can provide a direct experimental measurement of the $\mathrm{CED}^{\mathrm{EMS}}$, which can be checked a posteriori with the estimation given by the dosimetry code.

Table 3.4: fit parameters of the model curve formulated by Eq. 3.2 describing the CR dependence with respect to the elevation for the CRs measured in the TEW and in the CEW. The last column reports the value of the reduced χ^2 obtained at the end of the minimization procedure.

Energy Window	(A ± δA) [cps]	(μ± $\delta\mu$) [m^{-1}]	(B ± δB) [cps]	Reduced χ^2
TEW	2.4 ± 0.2	(5.5 ± 0.2) $\cdot 10^{-4}$	1.6 ± 0.2	0.94
CEW	11.4 ± 0.3	(5.9 ± 0.1) $\cdot 10^{-4}$	2.0 ± 0.4	1.12

3.3 Results and discussions

In this section is reported the results regarding the background calibration of the AGRS_16L spectrometer performed via the analysis of 1 second gamma ray spectra acquired during a 17612 seconds airborne survey over the sea. For ^{40}K and ^{214}Bi the relation between n^i and the altitude above the sea level is not guaranteed to be purely exponential down to low elevations, as the CRs in the ^{40}K and ^{214}Bi photopeaks may be contaminated by the presence of atmospheric radon. As already mentioned, this potential contamination also translates in a deviation from a purely linear relation between n^i and n$^{\mathrm{CEW}}$ at low elevations. The concentration of ^{222}Rn in the atmosphere can change considerably according to the different diffusion conditions. Nevertheless, above 1000-1500 m, mean ^{222}Rn concentrations of the daytime atmosphere drop sharply to values compatible with zero (around 2 ± 2 Bq/m^3) and then slowly reduce further with height until they reach 0.3 ± 0.4 Bq/m^3 above 3000 m [63]. In this analysis the CRs in the KEW and in the BEW is conservatively studied only for altitudes greater than 2000 m.

Fig. 3.4a shows the experimental CRs in the CEW, distinguished by colour according to the different flight IDs: the homogeneity of this partial datasets assures that there are no systematic effects related to the different acquisition times. Fig. 3.4b shows the experimental data for the CRs in the CEW obtained from the entire dataset, with the superimposed curve resulting from the minimization of the χ^2 function described by Eq. 3.4. The values of the fitting curve parameters are reported in Table 3.4.

The 1.12 reduced chi-square value denotes a good agreement between the model function and the experimental data. Although the parameters A and B in the CEW (Table 3.4) are affected by uncertainties having different order of magnitudes, at the nominal 100 m survey height of an airborne survey the two uncertainties separately produce approximately the same variation on the estimated CRs, which is below 3%. Thanks to the high acquisition statistics and to the wide range of investigated altitudes, the fit well constraints the value of the μ parameter entering the exponential dependency, which is estimated with an uncertainty of 2%.

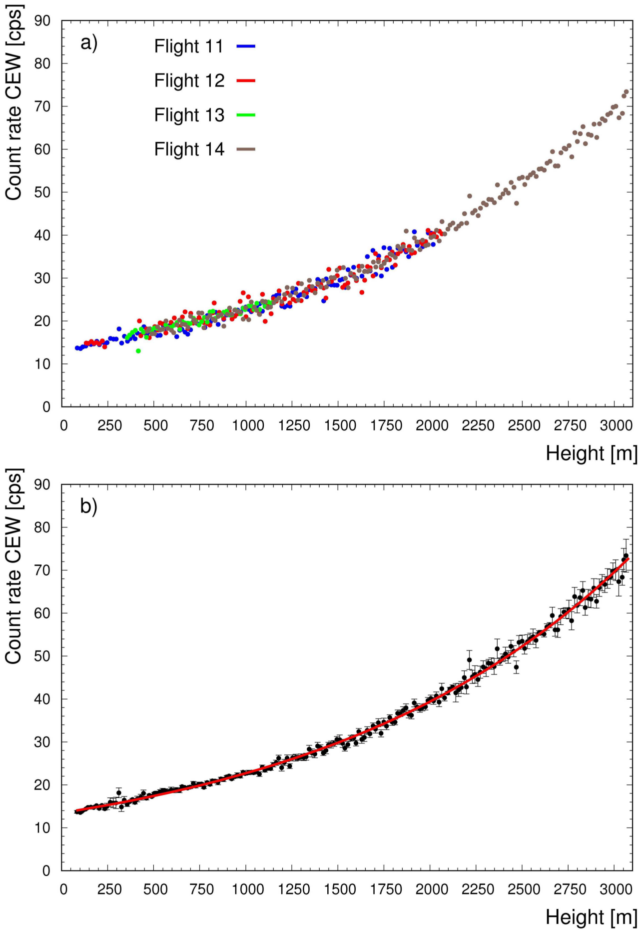

Figure 3.4: Panel a) displays the CR in the CEW as function of the altitude for the four different flights carried out during the background calibration survey over the sea. Data from different flights sit on top of each other, excluding systematic effects associated to the different acquisition times. Panel b) shows the CR in the CEW obtained from the entire dataset (black points) as function of the altitude with the superimposed exponential fit function (red solid line). Each point populating the global dataset has been obtained by clustering with an altitude binning of 15 m the spectra measured in that specific height range, disregarding any flight ID classification.

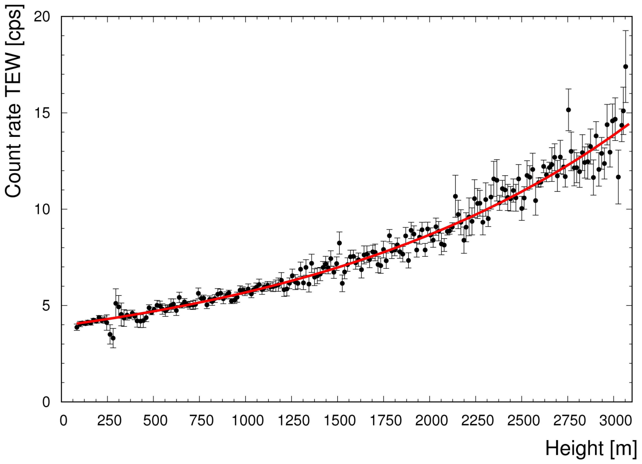

Figure 3.5: plot of the experimental CR in the TEW as function of the altitude (black points) together with the corresponding fitting curve (solid red line).

Fig. 3.5 shows the experimental CRs in the TEW evaluated on the entire dataset, together with the best fit exponential curve, whose parameters values are listed in Table 3.4. Also in this case the reduced chi-square value reflects the high data quality as well as the goodness of the model function in interpreting the measured CRs. The impact of the fitting parameter uncertainties on the estimated CR is negligible for what concerns μ while the uncertainties on A and B in the TEW individually give rise to a 5% variation of the predicted CR at 100 m.

For both the CEW and the TEW, the minimization of the χ^2 functions defined by Eq. 3.4 has been performed over the whole altitude range, corresponding to 200 height bins having a 15 m width. In both cases it is possible to recognize the presence of high statistics experimental points for height values below 200 m and around approximately 900, 2100 and 2650 m, which reflect the time flight statistics illustrated in Fig. 3.2. As a result of the definition of the objective χ^2 function, the discrepancy between the fitting function and the data is minimum in correspondence of the experimental points having the smallest statistical uncertainty.

In [56] and [55] an analogous study of the CR in the TEW as function of altitude is shown: this kind of reconstruction is carried out in both cases with a NaI spectrometer having 33.6 L volume, which precludes the possibility of a direct comparison with the results of this study. However, from a qualitative point of view, it emerges that the μ coefficient entering the exponential dependence (and essentially quantifying the rate of increase of the counting statistics) is for the three cases in the range (4 - 6) $\cdot 10^{-4}$ m^{-1}. Previous studies focused on a different altitude range, from around 1500 m to 4500 m: in this framework, this study demonstrates that the CR both in the CEW and in the TEW

Table 3.5: fit parameters of the model curve formulated by Eq. 3.3 describing the dependence of the count rates in the KEW, BEW and TEW with respect to the CR in the CEW. The last column reports the value of the reduced χ^2 obtained at the end of the minimization procedure.

Energy Window	(a ± δa) [cps]	(b ± δb) [cps/cps in CEW]	Reduced χ^2
KEW	3.7 ± 0.4	0.20 ± 0.01	1.00
BEW	2.0 ± 0.4	0.16 ± 0.01	1.02
TEW	1.58 ± 0.04	0.179 ± 0.002	1.02

maintains its exponential behavior down to tens of meters above sea level.

The analysis of the exponential trend of the CRs with respect to the altitude could have been done in principle also for the CRs in the KEW and in the BEW, restricting the fitting domain to the range of altitudes greater than 2000 m. However, as the slope of the CR increase with respect to the altitude is small in the 2000 m to 3000 m height domain, fitting in the 2000 - 3000 m height domain would suffer the lack of the low altitude tail, producing incorrect extrapolations down to sea level. This point can be a trigger for a deeper investigation, as it can potentially be a way for exploring the content of ^{222}Rn in the lower atmosphere 4.

Fig. 3.6 shows the experimental data with the superimposed linear curve resulting from the minimization of the χ^2 function described by Eq. 3.5, where the number of bins is equal to 200 for the TEW and is equal to 72 for the KEW and the BEW. Table 3.5 lists the fitting parameters together with the associated uncertainties and the reduced χ^2 value, which is almost 1 for all the three energy windows. In the perspective of using the linear relations for applying the Window Analysis Method [44] to airborne gamma-ray spectra, the uncertainties estimated in Table 3.5 are relevant for attempting an evaluation of systematics associated with aircraft and cosmic background corrections. With the hypothesis of flying at 100 m height, the mentioned background CR is (6.5 ± 0.5) cps in the KEW, (4.3 ± 0.6) cps in the BEW and (4.1 ± 0.1) cps in the TEW.

For the CR in the TEW, as both the exponential and linear curve reconstructions have been performed, it is possible to check the consistency of the obtained results according to the existing relations among the fit parameters. On the base of the expected value of the CRs in the CEW and in the TEW at zero altitude, it is also possible to establish the following relationship among fit parameters:

$$A^{TEW} + B^{TEW} = a^{TEW} + b^{TEW} \left(A^{CEW} + B^{CEW} \right) \tag{3.6}$$

Adopting the parameters reported in Table 3.4 one can calculate the left hand side of Eq. 3.6, which corresponds to (4.0 ± 0.4) cps.The right hand side of

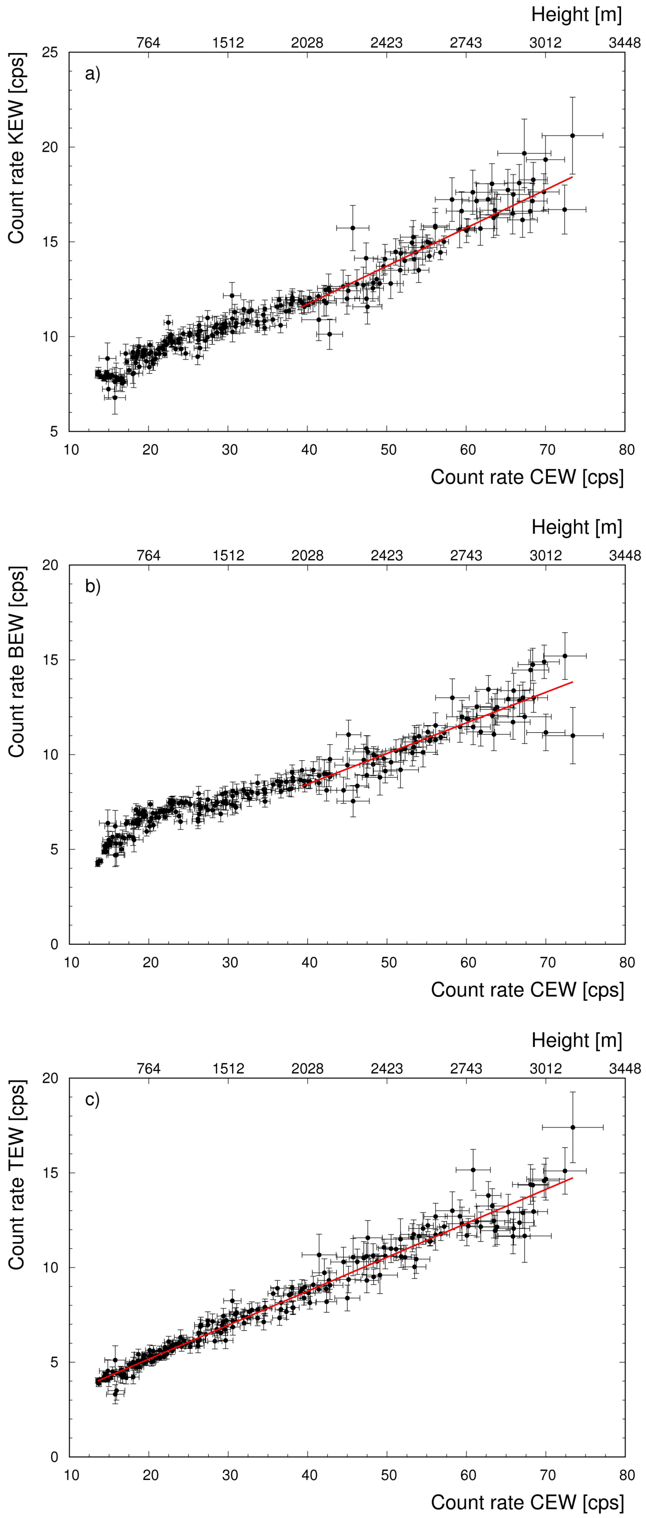

Figure 3.6: panels a), b) and c) report respectively the experimental CRs (black points) in the KEW, in the BEW and in the TEW as function of the CR in the CEW, together with the corresponding fitting curve (solid red line).

the equation can be estimated using the parameters listed in Table 3.4 and in Table 3.5, which provide a count rate of (4.0 ± 0.2) cps. The perfect agreement gathered from this analysis is an important internal consistency check of the goodness of both the exponential and linear model function in interpreting the experimental data.

Eq. 3.6 describes the sum of the constant aircraft CR plus the minimum cosmic CR component, corresponding to the one determined at zero altitude. As the right hand side of Eq. 3.6 can be calculated not only for the TEW, but also for the KEW and for the BEW, it is possible to estimate the minimum detectable CRs for the three energy windows of interest. These counting statistics can be naively converted to equivalent K, U and Th abundances homogeneously distributed across an infinite flat earth by means of sensitivity coefficients obtained from a dedicated ground calibration campaign on natural sites. According to this approach it is possible to estimate that the AGRS_16L detector can not measure K, U and Th concentrations lower than $0.05 \cdot 10^{-2}$ g/g (15.7 Bq/kg), 0.4 μg/g (4.9 Bq/kg), 0.8 μg/g (3.2 Bq/kg), respectively.

In Fig. 3.7 the $\mathrm{CED}^{\mathrm{EMS}}$ calculated with the CARI-6P and EXPACS dosimetry tools shows an evident linear relation with the measured $\mathrm{n}^{\mathrm{CEW}}$ values. By fitting the scatter plots with:

$$CED^{EMS} = a_{CED^{EMS}} + b_{CED^{EMS}} n^{CEW} \tag{3.7}$$

an excellent (more than 0.99) r^2 coefficient of determination has been obtained in both cases. On the base of the $a_{CED^{EMS}}$ and $b_{CED^{EMS}}$ parameters reported in Fig. 3.7 caption, the AGRS_16L detector is calibrated for future measurements of $\mathrm{CED}^{\mathrm{EMS}}$. Although the described calibration method is clearly model dependent, the average discrepancy among $\mathrm{CED}^{\mathrm{EMS}}$ estimations is ∼10%, which is not so far from the typical uncertainties obtained with traditional methods.

For fixed detector and dosimetry tool, the slope and intercept parameters of Eq. 3.7 are not expected to vary significantly for different geomagnetic latitude and solar activity. On the other hand, the total CED comprises also a muon and a neutron component (respectively dominant at sea level and at high altitudes), together with additional minor contributions due to protons and He and heavy ions. Appendix 9.3 presented the study of the relation between CED and $\mathrm{n}^{\mathrm{CEW}}$ (see Fig. 1): in the temporal and spatial domain of the data taking, a linear relation between these two quantities is clearly observed for both CARI-6P and EXPACS calculations. Since the CED varies with geomagnetic latitudes and solar activities, the obtained linear curve parameters change for different data taking conditions. However, in the typical altitude range of AGRS surveys ($z < 200$ m), the maximum variation of the CED due to solar activity rarely exceeds 5%.

in different solar activity scenarios, i.e. medium (March 2016, corresponding to the data taking period), high (June 2013) and low activity (May 2009) shows a maximum variation lower than 10%.

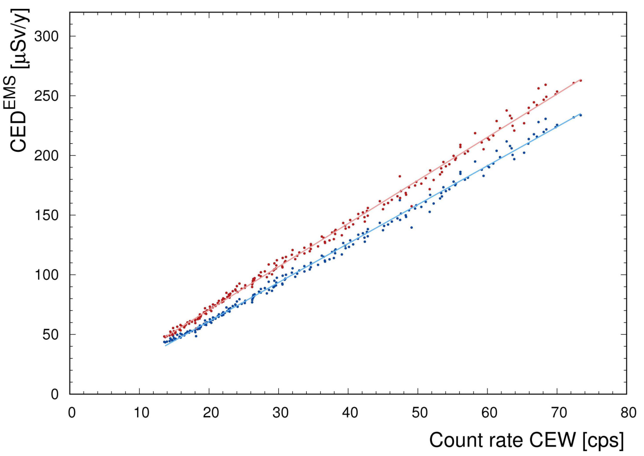

Figure 3.7: $\mathrm{CED}^{\mathrm{EMS}}$ obtained by running the CARI-6P (blue points) and the EXPACS (red points) softwares with fixed location (Viareggio, 43°56'N - 10°14'E) and fixed date (31 March 2016) corresponding to the data taking conditions versus the experimental CR in the CEW. The linear fitting curves (see Eq. 3.7) have best fit parameters equal to $a_{CED^{EMS}}$ = (-4.16 ± 0.59) μSv/y and $b_{CED^{EMS}}$ = (3.26 ± 0.02) μSv/(y·cps) for CARI-6P (light blue solid line) and $a_{CED^{EMS}}$ = (-1.67 ± 0.67) μSv/y and $b_{CED^{EMS}}$ = (3.62 ± 0.02)μSv/(y·cps) for EXPACS (light red solid line).

In Fig. 2 of Appendix 9.3 the ratio $\mathrm{CED}^{\mathrm{EMS}}$/CED is shown as function of the geographic latitude for four different altitudes, for a medium solar activity. As expected, the $\mathrm{CED}^{\mathrm{EMS}}$/CED ratio increases with increasing altitude, going from ∼14% at 0 m to ∼17% at 3000 m. A rule of thumb that can be formulated is that the ratio $\mathrm{CED}^{\mathrm{EMS}}$/CED∼0.15, where it has to be kept in mind that changing location, solar activity and dosimetry tool could bother this estimation.

Considering that the typical flight altitude of an AGRS survey is less than 200 m, the estimated variability of the CED with respect to different solar activity scenarios, i.e. medium (March 2016, corresponding to the data taking period), high (June 2013) and low activity (May 2009) shows a maximum variation lower than 10%. Considering a normal solar activity, in Fig. 2 the ratio $\mathrm{CED}^{\mathrm{EMS}}$/CED is shown as function of the geographic latitude for four different altitudes. As expected the $\mathrm{CED}^{\mathrm{EMS}}$/CED ratio increases with increasing altitude, going from ∼14% at 0 m to ∼17% at 3000 m.

It was estimated the variability of the $\mathrm{CED}^{\mathrm{EMS}}$ in the (0 - 3000) m altitude range with respect to different solar activity scenarios, i.e. medium (March 2016, corresponding to the data taking period), high (June 2013) and low activity (May 2009). The variation of the $\mathrm{CED}^{\mathrm{EMS}}$ associated with minimum and maximum solar activities is almost negligible at sea level and is of the order of 15 μSv/y for a 3000 m height, which would result in a marginal variation of the

CR in the CEW in the high altitude range.

As the absolute value of the CED together with the fractional contribution given by each component change with solar activity and geomagnetic latitude, a separate model is in principle required to assess the total CED from the CEDEMS fraction (see Appendix 9.3).

indeed, the parameters obtained by using $\mathrm{CED}^{\mathrm{EMS}}$ values from the EXcel-based Program for Calculating Atmospheric Cosmic ray Spectrum (EXPACS) [54] are: $a_{CED^{EMS}} = (1.3 \pm 0.6)$ μSv/y and $b_{CED^{EMS}} = (3.54 \pm 0.02)$ μSv/(y·cps). While the intercepts are in agreement at 1σ level, the slopes differ by about 15% (see Appendix 9.3). A refined dose calibration could be done by studying the linear fit parameters obtained with different dosimetric tools.

By establishing a relation between the measured $\mathrm{n}^{\mathrm{CEW}}$ and the dose rate values predicted by the CARI-6 code it is possible to determine a semi-empirical calibration curve to estimate the CED on the base of the CRs recorded in the CEW of airborne gamma-ray spectra.

The CED values as function of altitude in the range 77 - 3066 m have been determined by running the CARI-6 code using the geographic location and the acquisition time corresponding to the performed airborne surveys, which are 43°56' North 10°09' East and March 2016. The semi-empirical calibration curve allowing to convert the CRs in the CEW $\mathrm{n}^{\mathrm{CEW}}$ to the CED has been estimated via a linear fit of the type (see Appendix 9.3):

The CED profile has been reproduced by multiple runs of the CARI-6 code for different elevations, from which an exponential trend of the CED with respect to the altitude has been determined (see Appendix 9.3). In Appendix 9.3 a comparison between CED values obtained from CARI-6 runs and estimated according to different analytical models is shown. Fig. 3.7 shows a scatter plot of the CARI-6 CED versus $\mathrm{n}^{\mathrm{CEW}}$ values, which has been fitted according to the model linear relation of Eq. 17, depicted with the solid blue line. The best linear relation has been determined with a r^2 coefficient of determination equal to 0.99 and with linear regression parameters respectively equal to $a_{CED} = (58.5 \pm 3.2)$ μSv/y and $b_{CED} = (20.6 \pm 0.1)$ μSv/(y·cps).

3.4 Final remarks

This section illustrates the results of a ~5 hour airborne offshore survey dedicated to the AGRS_16L detector calibration for the gamma background signal originating from cosmic radiation and equipment radioactivity and for the assessment of cosmic effective dose to human population. This airborne campaign has been conducted with the Radgyro, an ultra-light aircraft dedicated to multispectral airborne surveys, and has the peculiarity of having investigated a wide range of altitudes above sea level (77-3066 m). The acquisition of 17612 1 second spectra over the sea at different altitudes allowed to separate the background count rate into a constant aircraft component and a cosmic component exponentially increasing with increasing height.

A statistical analysis has been performed to determine the parameters that linearly relate the count rate (CR) in the energy windows associated to the K, U and Th photopeaks and the counting statistics recorded in the cosmic energy window (CEW) in which no event coming from terrestrial radioactivity is expected. By monitoring the CR in the CEW and by applying the obtained linear relations it is possible to calculate for every airborne gamma-ray spectrum the background CRs in the photopeaks of interest that need to be subtracted prior the implementation of the height and stripping corrections before finally convert corrected elemental CRs to ground abundances. Minimum detectable K, U and Th abundances have been inferred from the minimum detectable CRs in the KEW, BEW and TEW, which correspond to the overall background CRs at zero altitude. On the basis of ground sensitivity coefficients, it is possible to assess that the minimum detectable abundances of the AGRS_16L detector are $0.05 \cdot 10^{-2}$ g/g, 0.4 μg/g, 0.8 μg/g, for K, U and Th respectively.

For the CRs in the CEW and in the TEW the exponential increase of counting statistics with respect to the altitude has been reconstructed, providing as argument for the exponential function a μ coefficient of $6 \cdot 10^{-4}$ m^{-1} which is comparable with the values published in [56] and [55]. Moreover, the analysis of the CRs in the TEW highlighted a perfect internal consistency among linear fit and exponential fit parameters. The exponential analysis for the CRs in the KEW and in the BEW was unfeasible due to the application of a low altitude cut to the dataset ($z>2000$ m), which allowed to exclude potential contamination caused by atmospheric ^{222}Rn. This point, however, deserves a deeper investigation as deviations from purely exponential/linear behaviors could in principle be used to quantify the atmospheric ^{222}Rn abundance at different elevations 4.

The AGRS_16L has also been calibrated for assessing the electromagnetic shower component of the cosmic effective dose ($\mathrm{CED}^{\mathrm{EMS}}$) to human population by using as calibrating reference the dose rate values obtained separately with the CARI-6P and EXPACS softwares. The relation between the CR in the CEW and the $\mathrm{CED}^{\mathrm{EMS}}$ has been found to be linear. Although this approach for calibrating an AGRS detector for $\mathrm{CED}^{\mathrm{EMS}}$ is clearly model dependent, the results are in agreement at ~10% level. This quality of this estimation is comparable with traditional approaches. Finally, it is observed a good linear relation between the cosmic effective dose (CED) and the count rate in the CEW (Fig. 1) as well as an almost constant profile of the $\mathrm{CED}^{\mathrm{EMS}}$/CED ratios at different latitudes of about 15% for typical AGRS survey altitudes.

The relation between the CR in the CEW and the annual cosmic effective dose has been found to be linear with a r^2 coefficient of determination equal to 0.99, and linear regression parameters respectively equal to $a_{CED} = (58.5 \pm 3.2)$ μSv/y and $b_{CED} = (20.6 \pm 0.1)$ μSv/(y·cps).

The content of this chapter is based on the following publication:

Baldoncini M., **Alberi M.**, Bottardi C., Mantovani F., Minty B., Raptis K.G.C., Strati V.“*Airborne gamma-ray spectroscopy for modeling radiation and* *effective dose in the lower atmosphere.*" IEEE Transactions on Geoscience and Remote Sensing (2017) DOI: 10.1109/TGRS.2017.2755466. (IF: 4.942)

Chapter 4

Study of radon vertical profile at lower tropopause height

4.1 Background

Atmospheric Radon is one of the major sources of background radiation together with cosmic rays (see Chapter 3) in AGRS measurements.^{222}Rn is a naturally occurring noble gas produced via alpha decay of ^{226}Ra and it is the only gaseous daughter product of the decay chain of ^{238}U, which is present in the majority of soil and rock types and which has a half-life of $\sim$4.5$\cdot$10^{9} yr, comparable to the Earth's age. As ^{222}Rn is inert and hardly soluble in water, it exhales from soils and rocks into the atmosphere and migrates by diffusion and convection almost without being subject to atmospheric removal processes, therefore running out mainly through radioactive decay [64]. ^{222}Rn atmospheric abundance is strictly connected with its exhalation rate from soils, which is typically on the order of 0.8 - 1.2 atoms/(cm$^{2}\cdot$s) and which is in turn affected by soil type, granulometry and moisture content, as well as by porosity and permeability [65], [66], [67].

Radon gas is responsible for the largest human exposure to natural ionizing radiation, the majority of which takes place in the home [68,69]: in this context, the characterization of building materials and drinking water is considered a relevant topic in the field of radiation protection [70–74]. In the light of assessing human exposure to radon radiation, strong efforts are being devoted to combine informations coming from indoor radon measurements, airborne gamma-ray (AGRS) spectroscopy measurements and geological mapping [75, 76].

The poor chemical reactivity, together with the 3.82 days half-life, makes ^{222}Rn a conventional and widespread atmospheric tracer. Indeed, ^{222}Rn has a relatively long half-life for being connotative of events related to turbulence (having a typical 1 hour time scale), but it also lasts shortly enough to have a high concentration gradient through the lower troposphere that can give insights into air vertical mixing mechanisms and help in tracing air transport processes. Monitoring atmospheric ^{222}Rn has a variety of applications in climate, air quality and pollution studies, including tracing air mass transport, tracing diurnal mixing in the lower atmosphere, calibrating seasonal regional emissions of climatically sensitive tracers including CO_2, CH_4, N_2O, and validating transport and mixing schemes in climate/weather models [77]. In the past a great effort has been dedicated in modeling the radon flux and air transport in the atmospheric boundary layer over land disregarding the contribution coming from the ocean, but recently it has been found that radon from the ocean can dominate that from land for specific wind condition [78].

Measurements of the vertical distribution of ^{222}Rn can be conducted as tower-based studies, which generally have high vertical resolution but altitude limited to 5 - 40 m, as well as via airborne ^{222}Rn or ^{222}Rn progeny measurements, which can span a larger height range (from hundreds of m to more than 10 km) but typically resolve few altitudes [63]. Direct ^{222}Rn measurements are generally carried out by laboratory extraction of ^{222}Rn absorbed by activated charcoal after the exposure to sampled air, while indirect measurements are generally made by alpha counting of ^{222}Rn progeny. The former provides direct radon concentrations, even if having an extracting and counting apparatus at short distance is necessary in order to reduce the time available for ^{222}Rn to decay as much as possible. On the other hand, ^{222}Rn progeny measurements rely on the assumption of secular equilibrium between ^{222}Rn and its daughter products.

Variations in the vertical radon concentration profiles produce changes in the natural background gamma-ray flux which, in turn, can be responsible for perturbations and contaminations in aerial monitoring results [79]. ^{214}Pb, having a half-life of 26.8 minutes, and ^{214}Bi, having a half-life of 19.8 minutes, are the two principal gamma-emitting daughters of ^{222}Rn, which, thanks to their short decay time, are usually in equilibrium with each other (i.e., their activities are about the same at all elevations). When the vertical mixing conditions are not characterized by quick variations (as instead happens close to sunrise and sunset), the steady state is generally reached which means that the concentration profiles of radon and its daughters tend to be near secular equilibrium, except near ground ($h < 25$ m) [80].

In this Chapter the results of a $\sim$4 hours AGRS survey over the sea is presented: when flying offshore no geological gamma signal is detected and the measured spectra result from the superposition of a constant contribution coming from the radioactivity of the equipment and of the height dependent contributions associated with the cosmic radiation and with atmospheric radon (see Chapter I, and 3. The AGRS campaign has been conducted over a wide range of altitudes, from 77 m up to 3066 m. Thanks to this large elevation extent, it has been possible to explore the presence of radon in the atmosphere via the modeling of the expected count rate in the ^{214}Bi photopeak energy window according to two analytical models which respectively exclude and account for the presence of atmospheric radon.

4.2 Data analysis

The overall effective acquisition statistics for the three flights is 14688 seconds, as reported in Table 4.1 along with the main features referred to the single surveys.

The estimated count rates in the energy windows of interest have been clustered according to an altitude binning of 15 m, which is conservative with respect to the estimated accuracy on the vertical position resulting from the combination of the altimetric data acquired by the instrumental setup mounted on board of the Radgyro (see Chapter 2 and Chapter 3). The count rates are estimated summing all the input count rates acquired in the same elevation bin and dividing by the number of 1 second spectra entering the summation. Figure 4.1 shows the count rates measured respectively in the ^{214}Bi Energy Window BEW,TEW, and CCEW, (see table 3.3) as function of the altitude above sea level, distinguished according to the different flights. In the TEW and CEW the variation of the count rates in different flights is compatible with the statistical fluctuation of the count rates: there is no systematic effect related to the different flight times and the exponential behavior is maintained down to low elevations. For the count rates in the BEW there is some evidence of data clustering for different flights, in particular at low elevations, which is a hint of the presence of ^{222}Rn gas in the atmosphere.

4.3 Theoretical model

^{222}Rn daughter products ^{214}Pb and ^{214}Bi are the main gamma-emitters in the ^{238}U decay chain and, since they bind to airborne aerosols, they are responsible for the measured radon background. Estimates of the ^{238}U content via AGRS measurements rely on the evaluation of background subtracted count rates in the ^{214}Bi photopeak energy window (BEW), which corresponds to the (1660-1860) keV energy range centered on the 1765 keV ^{214}Bi gamma emission line. Background correction involves the removal of gamma signal of non-geologic nature, which consists of three components resulting respectively from the decay of ^{214}Bi in the atmosphere, the radioactivity of the aircraft and its equipment due to presence of trace amounts of ^{238}U and ^{232}Th, and the interaction of secondary cosmic radiation with the air, the aircraft and the detector [81]. AGRS detectors are generally calibrated for the aircraft and cosmic background by performing high-altitude offshore flights in an area where atmospheric radon is at minimum. [44] suggests to measure spectra at a range of heights, typically

Table 4.1: summary of the main parameters for each of the 3 surveys over the sea. In the case of flights 11 and 14, 83 seconds and 30 seconds have been cut due to some radiofrequency interference between the PMT and the aircraft transponder. For each flight the ID, date, time, minimum and maximum altitude and acquisition time together with ground temperature (T), ground pressure (P) and ground wind velocity (W) at the take off and at the landing and sky conditions is reported. Globally the weather conditions during the flights were stable and without precipitations.

Flight ID	Date	Time	z min [m]	z max [m]	Acquisition time	T [°C]	P [hPa]	W [km/h]	Sky conditions
11	30/03/2016	17:42:10 19:29:43	77	2019	6370	18.6 14.9	1016.8 1015.3	17 15	Mostly clear
12	31/03/2016	18:13:55 19:46:47	126	2070	3041	22.2 19.7	1010.3 1009.9	17 11	Mostly clear
14	05/04/2016	16:37:16 18:05:43	461	3066	5277	24.6 20.7	1007.2 1015.7	17 2	Clear
Global			77	3066	14688				

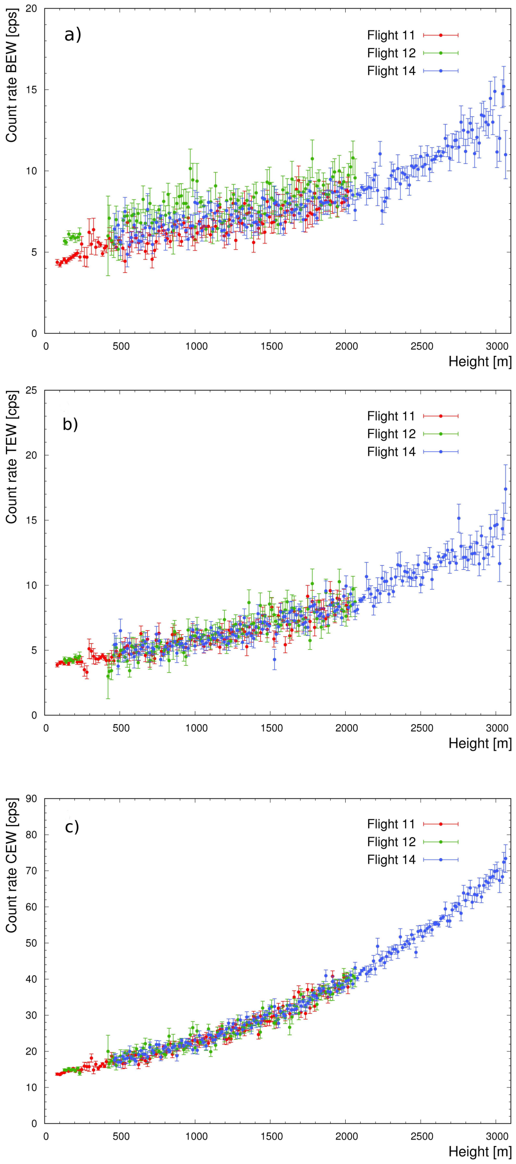

Figure 4.1: panels a), b) and c) show the count rate respectively in the BEW, TEW and CEW as function of the altitude for the 3 different flights carried out during the survey over the sea. In the TEW and CEW experimental data from different flights sit on top of each other, excluding systematic effects associated to the different acquisition times. In the BEW it is possible to recognize the effect of atmospheric radon contamination for the 3 different flights.

from 1.0 - 1.5 km up to 3.0 - 3.5 km over water with a 300 - 500 m step, for generally 10 - 15 minutes accumulation time at each height. In the absence of radon gas, the count rate in the BEW can be described as a superposition of a constant aircraft component and a cosmic component which is expected to exponentially increase with increasing height above sea level as stated by the following equation:

$$n_{BEW}^{aircraft+cosmic}(z) = A_{BEW}e^{\mu_{BEW}z} + B_{BEW} \tag{4.1}$$

where $n_{BEW}^{aircraft+cosmic}(z)$ is the count rate in the BEW and A_{BEW}, μ_{BEW} and B_{BEW} are constants [55, 56]. This radon free model is expected to accommodate experimental measurements, generally at altitudes greater than 2000 m. Indeed, although the atmospheric concentration of ^{222}Rn and of its daughter products can vary significantly with different diffusion conditions, mean ^{222}Rn concentrations are (4 ± 3) Bq/m^3 in the lowest 30 - 1000 m, while above 1000 - 1500 m mean ^{222}Rn concentrations generally show a steep decrease to values compatible with zero (around (2 ± 2) Bq/m^3), dropping even further to (0.3 ± 0.4) Bq/m^3 above 3000 m [63]. When looking to experimental data acquired at low altitudes, a deviation from the mentioned exponential behavior can be observed due to radon accumulation in the atmosphere. Traditionally, the presence of atmospheric radon is identified as a breakdown of the linear relation that is supposed to hold between the count rates in the BEW and the count rates measured in the CEW, the latter having exclusively cosmic origin since the maximum terrestrial gamma energy corresponds to the 2614 keV ^{208}Tl emission [55].

An alternative model can be developed with the aim of covering the entire altitude range and of recognizing and possibly quantifying the presence of the radon gas in the atmosphere via the detection of the gamma-signal generated by the ^{214}Bi decay. In presence of atmospheric radon, the overall count rate recorded in the BEW $n_{BEW}(z)$ comprises not only the aircraft plus cosmic component $n_{BEW}^{aircraft+cosmic}(z)$ (see Eq. 4.1) but also an altitude dependent component arising from atmospheric ^{214}Bi ($n_{BEW}^{Rn}(z)$) whose modeling requires a radon vertical profile, which is in turn directly connected with the dynamics of the atmospheric boundary layer.

The diurnal evolution of the atmospheric boundary layer, i.e. the ∼1-2 km thick layer where the atmosphere feels the contact with the ground surface, is governed by the mechanical and thermal surface-air interactions which are respectively driven by wind and solar radiation. Under clear sky conditions, after sunrise the warmed ground heats the air touching the ground, creating thermals that rise and cause intense motions which gradually create a convective boundary layer (or mixed layer), generally characterized by high homogeneity. As time passes, the growing convective region reaches higher altitudes till at sunset thermals cease and convection terminates, leading to the formation of a residual layer containing near zero turbulence and the residual moisture, heat, and pollutants that were mixed during the day. As long as the weather remains fair the cycle repeats on a daily timescale, with a mixing efficiency that partially depends on the amount of cover due to clouds which can intercept portions of the sunlight and reduce the amount of heat delivered to ground level [82].

In cases of fair weather, for convective boundary layers a very marked drop in radon concentrations is generally observed in crossing the separation between the mixed layer and the free troposphere, where radon abundances reach typically near-zero values [63]. In the case of mixed layers topped with residual layers radon exhibits a fairly constant profile in the mixed layer and tends to reduce linearly with height in the residual layers.

As the airborne campaign was conducted under clear sky conditions in a narrow range of days and always in the late afternoon, the simplified radon vertical profile adopted in this study is a discrete model according to which the radon concentration is uniform up to a cutoff altitude s, basically corresponding to the depth of the mixed layer, and null above the cutoff height. Figure 4.2 shows a schematic example of the behavior of the field of view of the gamma-ray detector to ^{214}Bi gamma signal as it moves to increasing altitude, starting from sea level up to the separation height between the two radon gas layers, till it reaches the radon free zone.

In the lower layer where the radon activity is uniform, the contribution to the count rate in the BEW originated by the atmospheric ^{214}Bi has a monotonic increase with increasing altitude. Indeed, at altitude zero the detector field of view can be approximated by a half-sphere as the gamma photon flux has only a downward incoming direction; when the detector starts lifting from sea level an upward incoming photon flux will start being visible enhancing the detected gamma signal. At an altitude equal to half the separation height $n_{BEW}^{Rn}(z)$ will reach its maximum. If the cutoff altitude s is high enough (for $s > 400$ m, corresponding to ~2.3 photon mean free paths, the count rate is essentially constant), the maximum count rate will reach a saturation value almost equal to double the count rate recorded at sea level, corresponding to the full-sphere field of view. Approaching the separation height s, the $n_{BEW}^{Rn}(z)$ count rate will start monotonically decreasing till it vanishes when the detector is far enough from the lower radon layer.

From the theoretical point of view it is necessary to model the propagation of unscattered photons from the source to the detector position (Figure 4.3). By integrating in spherical coordinates and by taking into account the azimuthal symmetry of the model, the flux of unscattered 1765 keV photons emitted by atmospheric ^{214}Bi is given by the following equation:

$$\Phi = \frac{A_v P_\gamma}{2\mu_a} \int_0^1 dcos\theta e^{\frac{-\mu_a h}{cos\theta}} \left[1 - e^{\frac{-\mu_a t}{cos\theta}} \right] \tag{4.2}$$

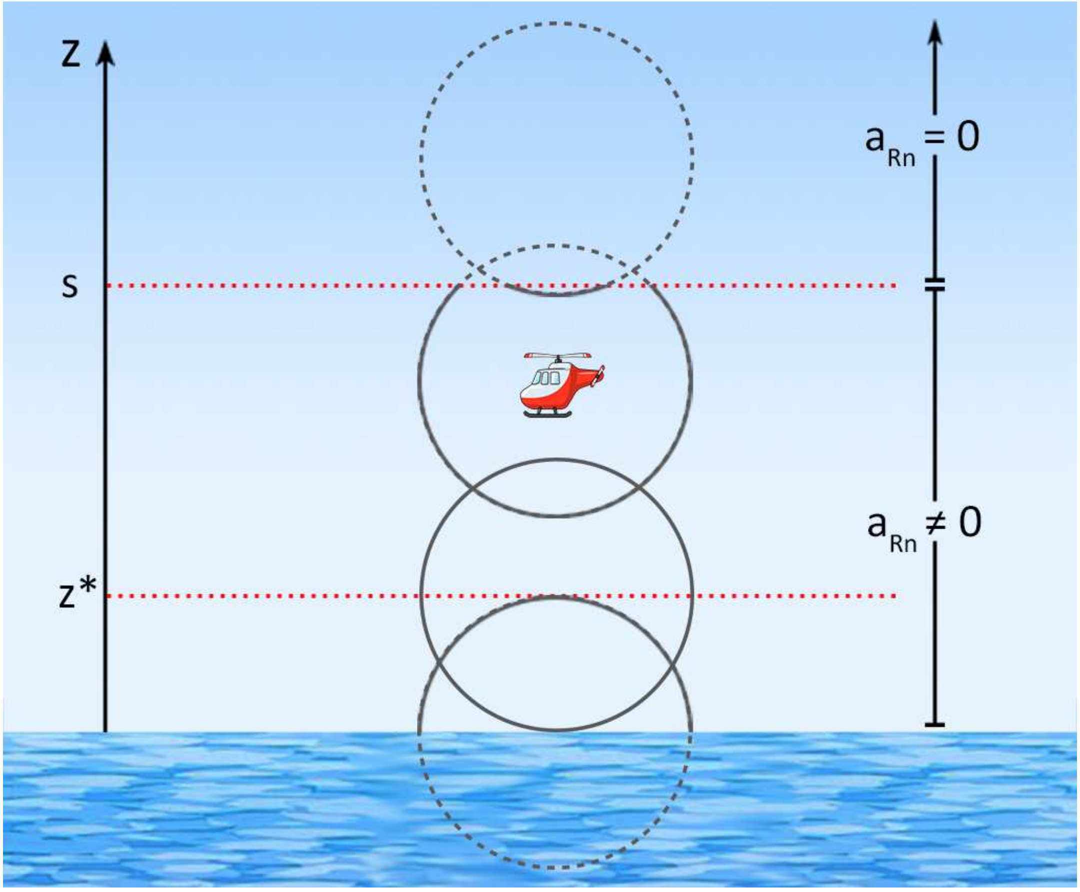

Figure 4.2: schematic illustration of the variation of the detector field of view to the atmospheric ^{214}Bi gamma signal with respect to the height. When the detector is at sea level, the field of view will be that of a half-sphere. With increasing height the detector starts seeing the upward photon flux till the field of view reaches saturation at the altitude z*, corresponding to the full-sphere case. Approaching the separation altitude s between the two radon layers the field of view starts shrinking and finally vanishes when the detector is completely immersed in the radon free layer.

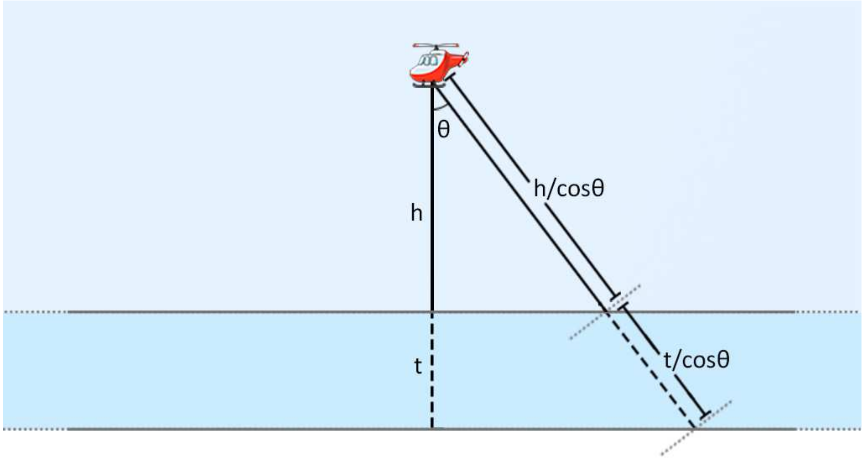

Figure 4.3: schematic diagram of the geometrical model adopted for estimating the unscattered photon flux reaching a detector situated at a vertical distance h from a source having infinite lateral extension and thickness t. In this context the source of thickness t corresponds to an air layer in which a homogeneous radon concentration is present.

where A_v is the volumetric activity in [Bq/m^3] of the uniformly distributed ^{214}Bi, P_γ is the γ-ray intensity for 1765 keV photons in [# of emitted γ/Bq], μ_a is the air linear attenuation coefficient referred to 1765 keV photons, t is the thickness of the air layer in which gamma photons are homogeneously and isotropically emitted, h is the vertical distance of the detector from the source layer [83]. By scaling for the detector cross sectional area and by some efficiency factor, Eq. 4.2 directly translates into the expression describing the variation of the count rate as a function of altitude.

The $n^{Rn}_{BEW}(z)$ vertical profile can be modeled by distinguishing the case in which the detector vertical position z is below or above the cutoff altitude s. In both scenarios the air layer at an altitude greater than s does not give any contribution to the signal as it has zero activity volume concentration. As illustrated in Fig. 4.4a, when the detector position z is below the cutoff altitude s, two air source layers having thickness respectively equal to z and $s - z$ contribute to the radon count rate with $n_1(z)$ and $n_2(z)$ as stated by the following equation:

$$\begin{aligned} n^{Rn}_{BEW}(z) &= n_1(z) + n_2(z) \\ &= C\int_0^1 dcos\theta \left[1 - e^{\dfrac{-\mu_a z}{cos\theta}}\right] + C\int_0^1 dcos\theta \left[1 - e^{\dfrac{-\mu_a (s-z)}{cos\theta}}\right] \quad (z < s) \end{aligned} \tag{4.3}$$

where C is the count rate in cps measured at zero distance from a semi-infinite homogeneous air volume source, i.e. the count rate obtained for $h = 0$ and $t \to \infty$ (see Eq. 4.2). If the detector position is above the cutoff altitude ($z > s$), the count rate arises only from layer number 3 (see Fig. 4.4b), where the air source layer thickness is s and the detector vertical distance from the source is $z - s$, corresponding to:

$$n_{BEW}^{Rn}(z) = n_3(z) = C \int_0^1 dcos\theta e^{\frac{-\mu_a(z-s)}{cos\theta}} \left[1 - e^{\frac{-\mu_a s}{cos\theta}} \right] \tag{4.4}$$

Therefore, the theoretical expression for the count rate in the BEW $n_{BEW}^{Rn}(z)$ can be summarized according to the following equation:

$$n_{BEW}^{Rn}(z) = \Theta(s - z)\left[n_1(z) + n_2(z)\right] + \Theta(z - s) n_3(z) \tag{4.5}$$

where $\Theta(x)$ represents the Heaviside step function.

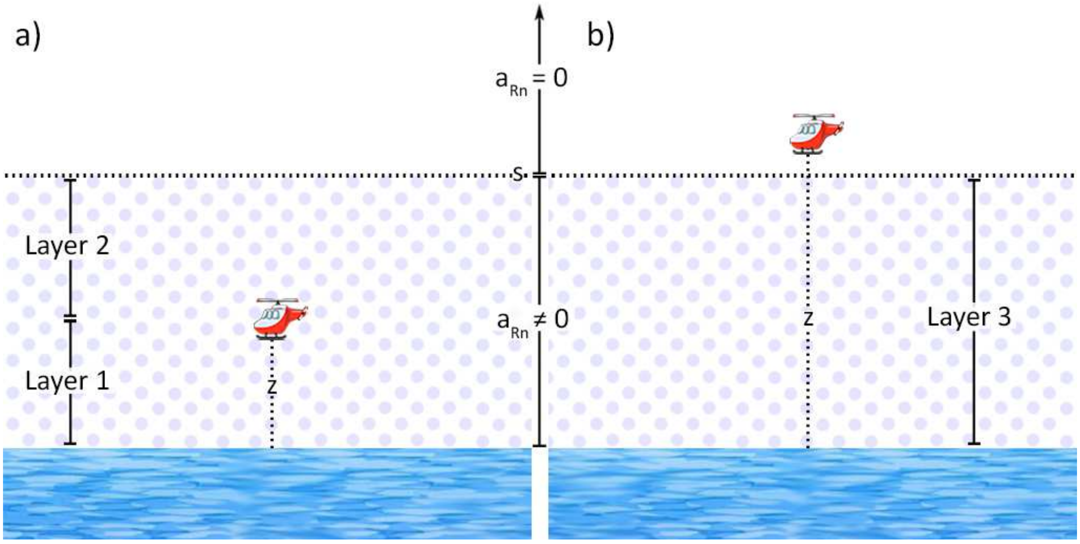

Figure 4.4: schematic illustration of the air layers generating the radon contribution to the count rate in the BEW. When the detector vertical position z is below the cutoff altitude s (which separates the lower atmospheric portion having uniform radon concentration from the upper one which has null radon abundance), there are two layers generating the ^{214}Bi gamma signal (a). When the detector vertical position z is above the cutoff altitude s, there is only one layer generating the ^{214}Bi gamma signal (b).

Figure 4.5 shows a representative example of the $n_{BEW}^{Rn}(z)$ curve. As expected, the curve is symmetrical with respect to an altitude value equal to half the separation height s. The separation altitude s corresponds to ~8.7 photon mean free paths, which is a long enough distance for the count rate at sea level $n_{BEW}^{Rn}(0)$ to reach the C value, corresponding to the count rate associated to a semi-infinite volume source. Similarly, $n_{BEW}^{Rn}(z)$ gets to reach and maintain the saturation value equal to $2C$ before starting to decrease when the altitude approaches s.

The overall count rate in the BEW can be therefore expressed according to the following equation:

$$n_{BEW}(z) = A_{BEW}e^{\mu_{BEW}z} + B_{BEW} + \Theta(s-z)\left[n_1(z) + n_2(z)\right] + \Theta(z-s)n_3(z) \tag{4.6}$$

Figure 4.6 shows the global behavior of $n_{BEW}(z)$, together with the separate components associated with the aircraft plus cosmic background and with the radon background. The radon contribution produces a curvature in the model function which is evident in the low altitude range ($z < 200$ m) where the initial half-spherical field of view approaches a full-spherical field of view. After the radon component has reached the plateau, the model curve grows in parallel to the radon free curve just shifted upward by the radon saturation count

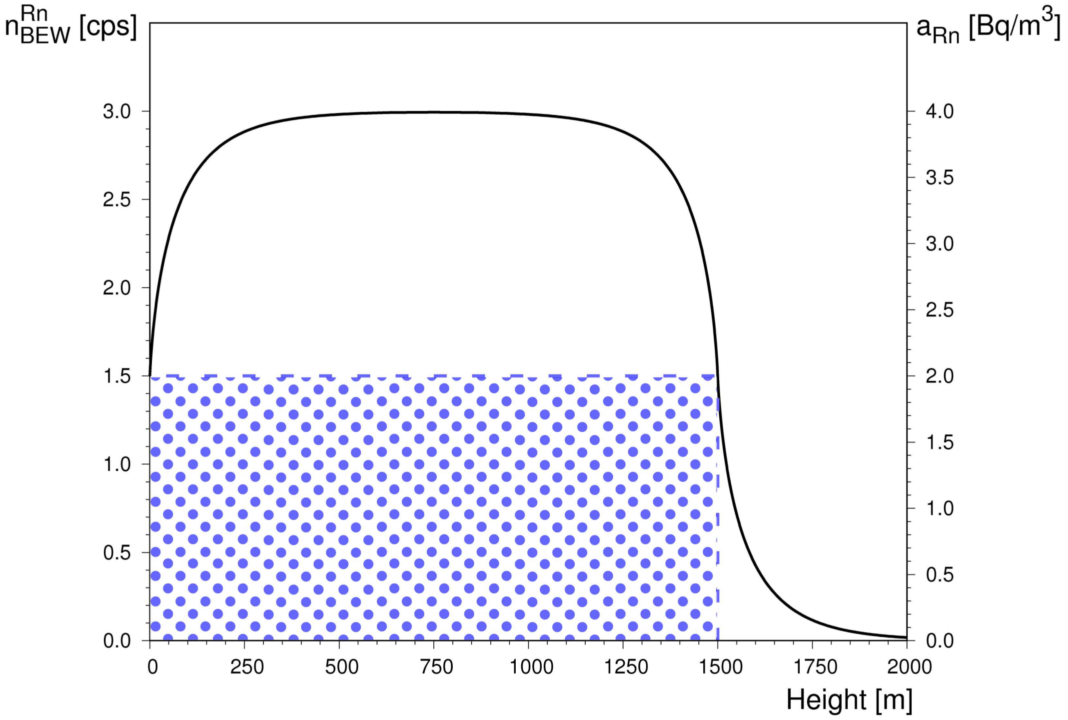

Figure 4.5: the black solid line illustrates the $n_{BEW}^{Rn}(z)$ count rate (left y axis) as function of the altitude for a C count rate value equal to 1.5 cps, a gamma linear attenuation coefficient μ_a equal to 0.005829 m^{-1} and a cutoff altitude s equal to 1500 m (see Eq. 4.5). The blue polka-dotted pattern represents the 2 Bq/m^3 homogeneous radon concentration (right y axis) in the atmospheric layer below 1500 m. In the air layer at altitude larger than 1500 m the radon concentration vanishes.

rate. In approaching the separation altitude between the two radon layers the model curve exhibits a kink, whose vertical extent depends on the values of the exponential function parameters and of the radon concentration gradient between the two layers. This kink translates into a local count rate decrease till the model curve matches the curve obtained in the radon free scenario at an altitude which is ~400 m higher than the cutoff altitude.

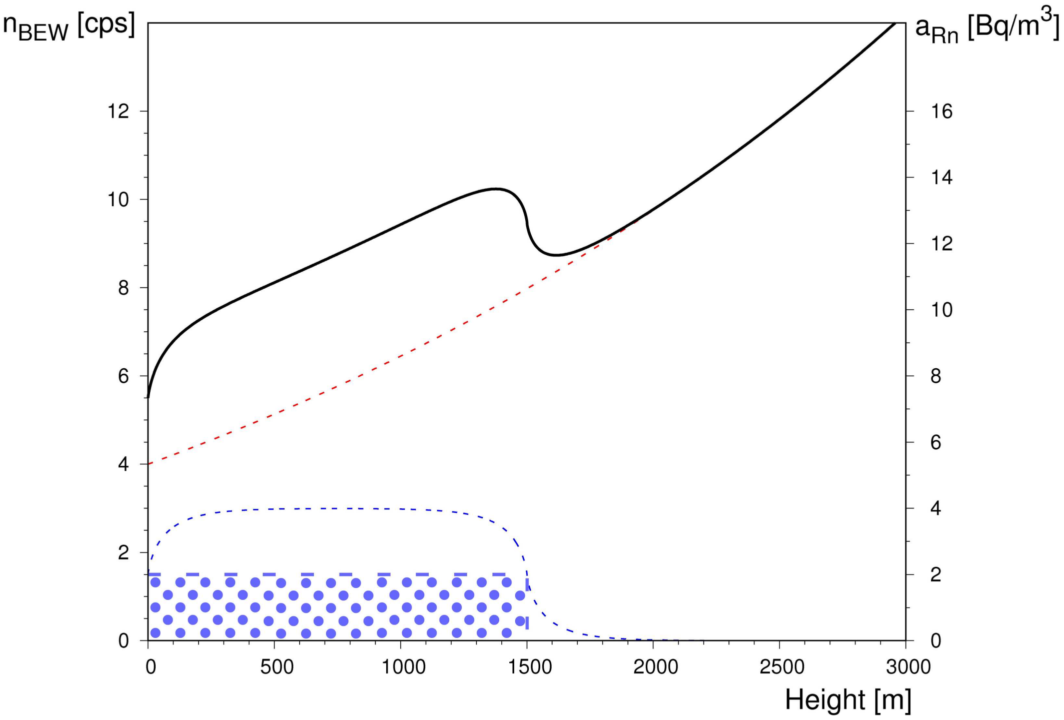

Figure 4.6: the blue dashed line shows the curve for the count rate in the BEW (left y axis) due to the presence of atmospheric radon $n_{BEW}^{Rn}(z)$ obtained for a cutoff altitude s equal to 1500 m and a C value of 1.5 cps (see Eq. 4.5). The blue polka-dotted pattern represents the 2 Bq/m^3 homogeneous radon concentration (right y axis) in the atmospheric layer below 1500 m. In the air layer at altitude larger than 1500 m the radon concentration vanishes. The red dashed line shows the aircraft plus cosmic contribution obtained with A_{BEW} = 7 cps, μ_{BEW} = 3 $\cdot 10^{-4}$ m^{-1} and B_{BEW} = -3 cps (see Eq. 4.1). The black solid line represents the overall count rate in the BEW, determined as the sum of the aircraft plus cosmic contribution and the atmospheric radon contribution (see Eq. 4.6).

4.3.1 Determination of the count rate vertical profile parameters

The two theoretical models described in the previous section (i.e. i) a radon free model defined by Eq. 4.1 and a 1 layer uniform radon model defined by Eq. 4.6) have been used in order to reconstruct the observed count rate in the BEW as a function of altitude. The parameters of the theoretical curves have been determined via the minimization of a χ^2 function. For the radon free model the χ^2 minimization has been performed for the count rates measured at elevations greater than 2000 m, where the condition of absence of radon is supposed to hold. On the basis of Eq. 4.1, the following definition of the χ^2 function has been used:

$$\chi^2 = \sum_{j=1}^{N} \left[\frac{n^j_{BEW} - (A_{BEW} e^{\mu_{BEW} z_j} + B_{BEW})}{\sigma_{n^j_{BEW}}} \right]^2 \tag{4.7}$$

where N is 79, equal to the number of experimental data measured at z_j >2000 m, n^j_{BEW} is the count rate in the BEW measured at z_j, z_j is the average elevation obtained for the $j-th$ elevation bin and $\sigma_{n^j_{BEW}}$ is the 1 sigma uncertainty associated to the counting statistics, corresponding to the square root of the total counts recorded at z_j in the BEW divided by the acquisition time. For the model containing the radon contribution, the χ^2 minimization has been performed over the entire altitude range corresponding to the 14688 seconds of data taking. On the basis of Eq. 4.6, the following definition of the χ^2 function has been used:

$$\chi^2 = \sum_{j=1}^{N} \left[\frac{n^j_{BEW} - (A_{BEW} e^{\mu_{BEW} z_j} + B_{BEW} + \Theta(s - z_j) \left[n_1(z_j) + n_2(z_j) \right] + \Theta(z_j - s) n_3(z_j))}{\sigma_{n^j_{BEW}}} \right]^2 \tag{4.8}$$

where N is 423, equal to the number of experimental data measured in the entire altitude range, and n^j_{BEW}, z_j, $\sigma_{n^j_{BEW}}$ defined as previously described. The best fit solutions have been found using a fixed value for the 1765 keV gamma linear attenuation coefficient μ_a equal to 0.005829 m^{-1} [1].

4.4 Results and discussion

Figure 4.7a) and Figure 4.7b) show respectively the fitting curves obtained by minimizing the χ^2 function for the radon free model (see Eq. 4.7) and for the

---

[1] National Institute of Standard and Technology website, http://physics.nist.gov/PhysRefData/Xcom/html/xcom1.html

model allowing for the presence of a uniform radon concentration in the atmosphere up to a cutoff altitude (see Eq. 4.8). The best fit parameters obtained in both cases are reported in Table 4.2.

Table 4.2: fit parameters of the model curves defined by Eq. 4.1 and by Eq. 4.6 describing the dependence with the altitude of the count rate in the BEW respectively in the absence or presence of atmospheric radon. The last column reports the value of the reduced χ^2 referred to the entire range of investigated altitudes.

Theoretical model	$A_{BEW} \pm \delta A_{BEW}$ [cps]	$\mu_{BEW} \pm \delta\mu_{BEW}$ [m^{-1}]	$B_{BEW} \pm \delta B_{BEW}$ [cps]	s ± δs [m]	C ± δC [cps]	Reduced χ^2
without Rn (Eq. 4.1)	0.39 ± 0.07	$(1.0 \pm 0.1)\cdot 10^{-3}$	5.5 ± 0.3	/	/	5.0
with Rn (Eq. 4.6)	8.2 ± 0.2	$(2.54 \pm 0.06)\cdot 10^{-4}$	-4.9 ± 0.2	1318 ± 22	0.68 ± 0.05	2.1

From this study it emerges that a theoretical model accounting only for the cosmic and aircraft component is not satisfactory in describing the data distribution, especially at low elevations. Indeed, the model allowing for the presence of radon in the atmosphere provides a better fit to the data, as proved by the reduction of the reduced χ^2 value from 5.0 for the radon free model to 2.1 for the model accounting for radon in the atmosphere.

It is also possible to perform a consistency check of the A_{BEW} and B_{BEW} fit parameters considering that their sum corresponds to the expected count rate at zero altitude in the absence of radon ($n_{BEW}^{aircraft+cosmic}|_{z=0}$). The latter quantity can indeed be obtained also from the parameters of the linear function describing the relation between the count rates in the BEW and the count rates in the CEW, i.e.:

$$\begin{gathered} n_{BEW}^{aircraft+cosmic}|_{z=0} = a_{BEW} + b_{BEW} \cdot n_{CEW}|_{z=0}, \\ \text{with } n_{CEW}(z) = A_{CEW} e^{\mu_{CEW} z} + B_{CEW} \end{gathered} \tag{4.9}$$

where the fit parameters a_{BEW}, b_{BEW}, A_{CEW} and B_{CEW} have been obtained in an independent aircraft plus cosmic background calibration survey 3[2].

Therefore, the following equation between fit parameters should hold:

$$A_{BEW} + B_{BEW} = a_{BEW} + b_{BEW} \left(A_{CEW} + B_{CEW}\right) \tag{4.10}$$

The value obtained for the left hand side of Eq. 4.10 according to the radon free model is (5.9 ± 0.4) cps, while the model accounting for atmospheric radon provides (3.3 ± 0.4) cps, which are respectively incompatible and compatible at 1σ level with the right hand side value of (4.1 ± 0.7) cps. The fit value for the s parameter is equal to (1318 ± 22) m, comparable with atmospheric radon ranges reported in [63].

---

[2] $a_{BEW} = (2.0 \pm 0.4)$ cps, $b_{BEW} = (0.16 \pm 0.01)$ [cps in BEW]/[cps in CEW], $A_{CEW} = (11.4 \pm 0.3)$ cps and $B_{CEW} = (2.0 \pm 0.4)$ cps

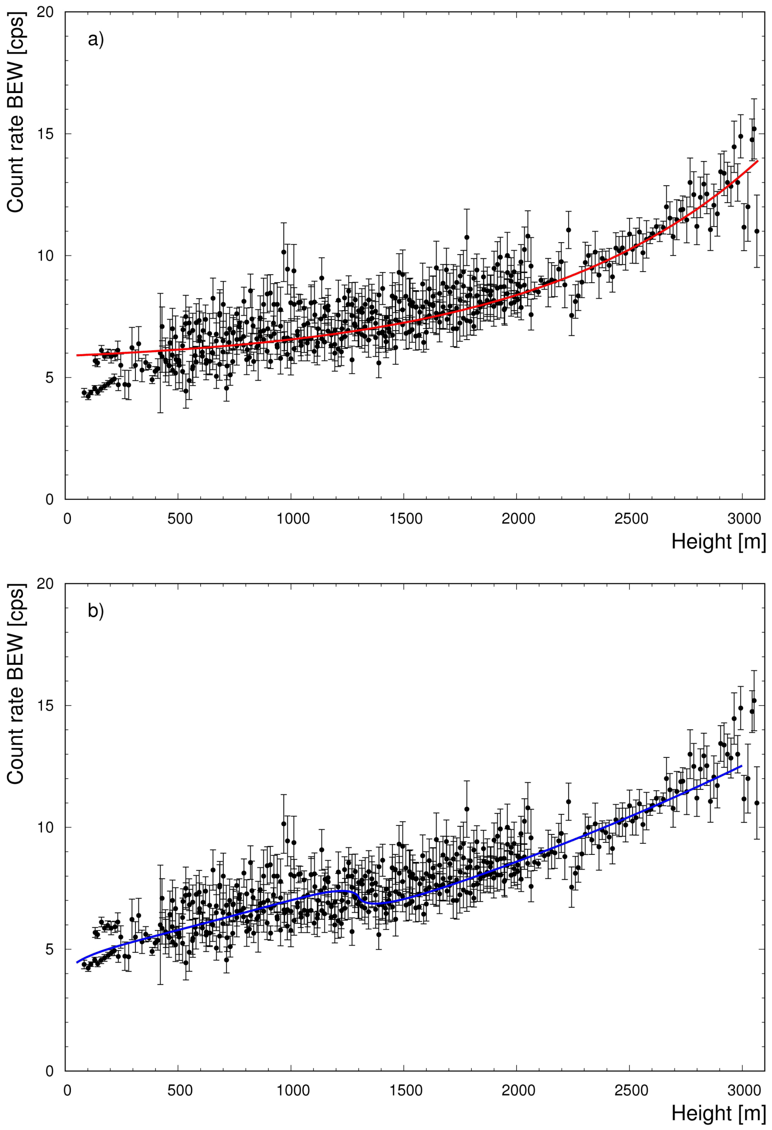

Figure 4.7: panel a) shows the count rate recorded in the BEW during the entire survey (black points) together with the curve (red solid line) obtained by fitting the data acquired at z>2000 m with a theoretical model that includes only the aircraft and cosmic components of the gamma signal (see Eq. 4.1). Panel b) shows the same dataset (black points) with the model curve (blue solid line) obtained by fitting the data acquired in the entire elevation range with the theoretical model that accounts also for the presence of radon in the atmosphere (see Eq. 4.6).

The fit value for the C parameter corresponds to the sea level count rate associated to the presence of radon (and its gamma emitting daughter nuclei) in the atmosphere, which can be converted into radon abundance, provided a sensitivity calibration factor. From an independent ground calibration campaign, the sensitivity matrix necessary for the estimation of the natural radionuclide concentrations via the Window Analysis Method has been determined [56]. On the base of the calibration process a sensitivity coefficient $S_{UU} = 0.71$ cps/(Bq/m^3) is estimated. Since it allows for converting the eU volumetric abundance into count rate in the BEW, is possible to obtain a crude estimate of mean radon concentration in the atmospheric (mixed) layer of $Rn = (0.96 \pm 0.07)$ Bq/m^3. The obtained values for the mean radon abundance and for the mixed layer height are comparable with data published by [63] and [84]. In Figure 6 of [84] it is shown that radon concentration is inversely related to the mixing layer height, corresponding typically to about 1 Bq/m^3 for a mixing layer height of 1500 m. Moreover, the diurnal variations of radon abundance and mixing layer height in different seasons (Figure 5 of [84]) show that typical values of radon abundance in the spring late afternoon are about 1.2 Bq/m^3 for a mixing layer height of $\sim$1000 m.

A further generalization of the 1 layer model having radon contribution described by Eq. 4.5 led to the theoretical description of a 2 layers model built by introducing the s_1, s_2, C_1 and C_2 model parameters in the mathematical description of the count rate. s_1 and s_2 correspond to the separation altitudes of a lower and a higher atmospheric layer characterized respectively by a C_1 and C_2 count rate. The best fit with the 2 layers model provided a $\chi^2 = 2.0$ and $s_1 = (1166 \pm 12)$ m, $Rn_1 = (1.24 \pm 0.09)$ Bq/m^3, $s_2 = (1562 \pm 28)$ m and $Rn_2 = (0.6 \pm 0.1)$ Bq/m^3, where Rn_1 and Rn_2 have been obtained by dividing the C_1 and C_2 cps values by the S_{UU} constant. The 2 layers and 1 layer models fit the experimental data with essentially the same statistical significance, providing similar χ^2 values. According to the quality of the dataset, it is not feasible to have a clear discrimination between a 1 layer model and a 2 layers model: indeed, the 1 layer model having best fit parameters s=(1318 ± 22) m and Rn= (0.96 ± 0.07) Bq/m^3 basically represent the same scenario of a 2 layers model characterized by the above mentioned best fit parameters s_1, s_2, C_1 and C_2, where the average separation altitude and the average radon content essentially reproduce the s and Rn values provided by the 1 layer model.

4.5 Advantages and Perspectives

Radon measurements are typically performed by counting experiments of alpha-particles or beta-particles emitted in the decay of radon progeny, requiring the collection and filtering of air mass samples which is a time consuming and laboratory intense procedure. This study proved the feasibility of performing atmospheric ^{214}Bi AGRS measurements and of assessing its abundance and vertical distribution: in this context, future combined direct radon measurements would provide an important basis for the validation of the model proposed in this study.

The discrimination of ^{214}Bi gamma emissions from other sources of radiation is far from trivial: long acquisitions over a wide range of altitudes are a key ingredient for splitting the different contributions to the measured count rates. Indeed, according to the quality of the experimental dataset it has not been possible to statistically discriminate a simplified one layer radon vertical distribution from a more refined two layers radon vertical profile. In perspective, AGRS measurements carried out with large detectors (e.g. the typical 33 L NaI(Tl) systems) mounted on helicopters, which unlike autogyros are able to hover, could provide high statistics experimental data at well separated altitudes potentially increasing the resolution on different ^{222}Rn vertical strata.

The content of this chapter is based on the following publication:

Baldoncini M., **Alberi M.**, Bottardi C., Mantovani F., Minty B., Raptis K.G.C., Strati V.“*Exploring atmospheric radon with airborne gamma-ray spectroscopy.*” Atmospheric Environment. (2017). DOI: 10.1016/j.atmosenv.2017.09.048 (IF: 3.948)

Part II

Testing gamma ray portable spectrometer for geological and educational experiences

Introduction

The need for quick and accurate gamma spectroscopy measurements in situ has led to the development of the ZaNaI detector. The ZaNaI instrument (Fig. 4.8) is a portable gamma-ray spectrometer designed for natural and artificial radioactivity measurement composed by a sodium iodide (SCIONIX NaI(Tl)) crystal with a cubic shape of a volume of 1 liter (10.16 cm x 10.16 cm x 10.16 cm) and energy resolution of 7.3% at 662 keV (^{137}Cs), 5.2% at 1172 and 1332 keV (^{60}Co). The portable scintillation gamma-ray spectrometer is configured in a backpack inside a thermo-isolator holding house in order to protect the system from temperature changes during the in-situ measurement process. The detector is coupled with a PMT (photo-multiplier tube) base with integrated bias supply, preamplifier and digital multi-channel analyzer (MCA, CAEN GammaStream) with 2048 channels (Fig. 4.8) that is controlled by a tablet or Smartphone (via Bluetooth) with the application GammaTouch. The obtained data log formats are easily imported to GIS systems and Google Earth.

Figure 4.8: the digital multi-channel analyzer GammaStream (left) and The ZaNaI detector (right)

This detector is particularly suitable for in-situ measurements [85] as it can be easily transported, it is able to collect a sufficient statistic in a short time and it can reliably operate in different environmental conditions.

The ZaNaI is able to discriminate the different natural and artificial radioactive isotopes gamma emitters through two different spectral analysis: Windows

Analysis Method (WAM) and Full Spectrum Analysis (FSA). The instrument was calibrated following the method of Full Spectrum Analysis with the Non-Negative Least Squares (FSA-NNLS) constraint, as described in [86].

During my PhD course I studied the application of ZanaI in two different circumstances, focusing on the performances of various analysis methods. In Chapter 5 an extensive radiometric survey performed with ZaNaI in Varsican Basements of Northeastern Sardinia, for geochemical and geological purposes is presented. In this circumstance I participated to the dtata analysis of the 368 in situ measurements acquired with ZaNaI using FSA and WAM method. I have also contributed to the development of a dedicated software able to correct the HPGe aboundances measurements taking into account the fully energy calibration of the detectors performed using certified reference materials presented in the following pubblication: [87].

A further successful application of ZaNaI was done during the Summer Summer School in Nuclear Physics and Technologies in Ferrara with the aim to explain the fondamentals of the enviromental radioactivity in a classroom of undergraduated students. In this educational project I have planned and conducted laboratory activities and adapted the ZaNaI instrument for a better usability of the students. The essential of these experience is reported in Chapter 6.

Chapter 5

Mapping uranium distribution in Northeastern Sardinia with ZaNaI in severe geological context

5.1 Background

One of the strengths of ZaNaI instrument is the immediacy of the result as well as global information mediated on an area that is considered representative of a geological reservoir. Unlike the classic sampling, is it possible to have an immediate and accurate information of the abundances of natural ^{40}K, ^{214}Bi and ^{208}Tl radionuclides presents in the rocks. In light of these strengths, an optimal application of this instrument consists of a geochemical survey in large rock outcrops. The ideal condition has been identified in the north-east region of Sardinia where it is located the state the Variscan Basement of Northeastern Sardinia (VBNS).

VBNS is a benchmark for the study of 'hot' collisional chains characterized by a high temperature-low pressure (HT-LP) gradient. Several processes might have enhanced the Variscan geotherm, such as i) shear heating [88] [89], ii) the advection of hot, mantle-derived melts, iii) the break-off of the mantle lithosphere [90] the selective enrichment of radiogenic heat-producing elements, such as U, Th and K, in the crust [91]. The widespread late-Variscan magmatism in the Corsica-Sardinia Batholith (C-SB) has been occasionally explained in terms of enhanced radiogenic heating. The models that describe the efficiency of the processes depend strongly on the uranium content of the fertile crust [92]. The heterogeneous distribution of uranium throughout the VBNS might be a proxy for investigating the applicability of thermal models based on the selective enrichment of radiogenic elements in the crust [4] [93], [94].

In addition, the outcrops in VBNS are the most accessible intrusive bodies for studying the geoneutrino signal in the Borexino experiment [95], which is particularly sensitive to the U and Th contents and distributions in the Variscan continental crust [96].

Finally, this survey has implications related to the public health, as recent investigations [97] showed that the Sardinia region is characterized by high values of radon gas, monitored in 124 dwellings. Since for good bedrock exposure, as in the case of VBNS, the correlation between indoor radon concentrations and Uranium content of the underlying rocks increases, the results of this study potentially constitute a baseline for future mapping of radon-prone areas.

This chapter presents a map of the eU distribution (this notation indicates equivalent uranium, as the secular equilibrium in the ^{238}U decay chain has been assumed) in the VBNS at a scale of 1:100,000 as support for further studies regarding the main geophysical, geochemical and geodynamic features of the continental crust in this region. This study is included in the framework of a research project which has already led to the realization of the total natural radioactivity map of the Tuscany region [98] and Veneto region [24].

The spatial model, together with its uncertainties, was obtained using the Kriging with Variance of Measurement Error method for 535 gamma-ray spectrometry measurements. The eU distribution is discussed in the geodynamic framework proposed by [88], taking into account the petrological features of the C-SB, the compositional variation and the emplacement timing of Variscan granitoids.

5.2 Geological setting

The Variscan belt of Western Europe resulted from the collision of Northern Gondwana and Laurussia in a time interval spanning from the Late Devonian to the Early Permian (∼380-270 Ma). The European Variscan crust, including the Corsica-Sardinia massif, experienced several episodes of plutonic and volcanic activity with different petrochemical affinities [99] [100].

The C-SB, with its ca. 12,000 km^2 area, constitutes one of the largest batholiths in south-western Europe, emplaced in approximately 40 Ma (Late Mississippian Pennsylvanian-Early Permian). Three main magmatic suites can be recognized: a magnesium-potassium complex exposed only in northern Corsica, a peraluminous calc-alkaline complex [101] [102], and finally, a late to post-orogenic alkaline suite in VBNS [103]. The 2,100 km^2 of the VBNS (Figure 5.1) are characterized by several calc-alkaline plutons and a few minor alkaline complexes emplaced within migmatites and amphibolite-facies of metamorphic rocks [88] . According to [104] the migmatites outcropping in the study area are related to high-pressure metamorphism occurred in the Internal Nappes of the Sardinia Variscides at the age of the initial continent–continent collision.

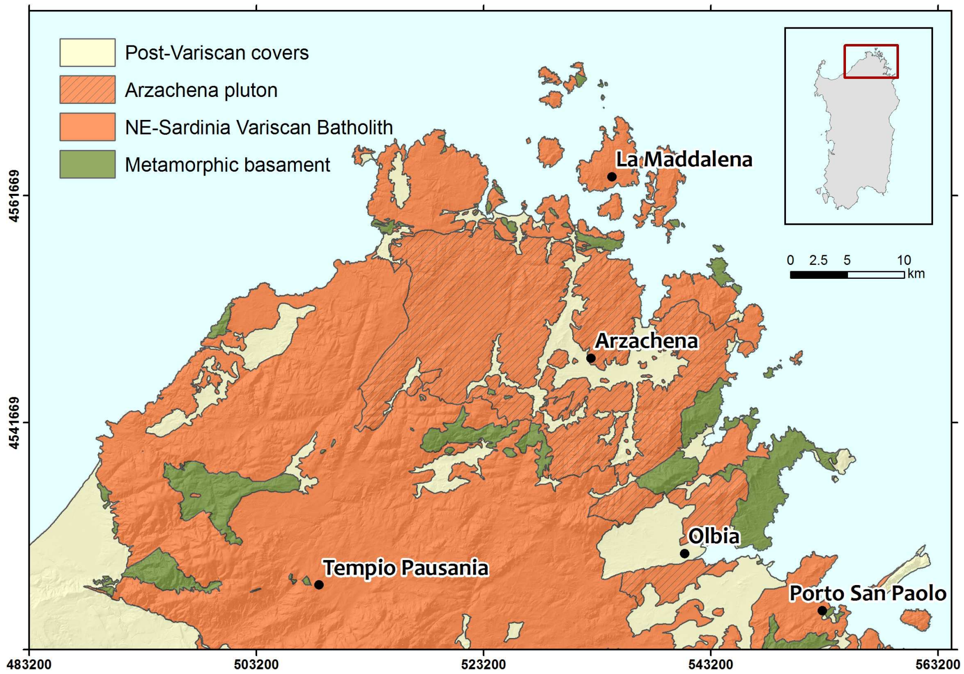

Figure 5.1: geological sketch map of the VBSN (cartographic reference system WGS84 UTM ZONE 32N), modified from [88]

Both migmatites and the calc-alkaline plutons have been interpreted in terms of extensive crustal melting related to the establishment of an anomalous thermal gradient [105]. One of the main contributions to the high geothermal gradient, which is required to induce anatexis processes, originates from the enrichment of radiogenic heat producing elements caused by several genetic processes, such as subduction of continental crust, crust-scale migmatization [90], melt dehydration and segregation [106]. Understanding heat production and transfer mechanisms is relevant for modeling thermal-kinematic and exhumation processes [91].

5.3 Methods

The 535 input data points used for realizing the presented map come from 167 rock sample measurements and 368 in situ measurements. The surveys were planned based on the Geological map of Sardinia at a scale of 1:200,000 [107] and the structural map of Variscan northern Sardinia at a scale of 1:100,000 [88].

The eU abundances in the rock samples collected from fresh outcrops were measured using the MCA-Rad system, a gamma-ray spectrometer equipped with two HPGe p-type detectors having a 60% relative coaxial efficiency and an energy resolution of approximately 1.9 keV at 1332.5 keV (60Co) [108]. The

MCA_Rad system is accurately shielded with 10 cm thickness of copper and 10 cm thickness of lead by reducing the laboratory background of approximately two orders of magnitude. The absolute peak energy efficiency of the MCA_Rad system is calibrated using certified reference materials (RGK_1, RGU_1 and $RGTh_1$) traceable by the International Atomic Energy Agency [109] [87]. The total uncertainty for the absolute peak energy efficiency is estimated to be less than 5%. Prior to measurement, each rock sample was crushed, homogenized and sealed in a cylindrical polycarbonate container of 180 cm^3 volume. Then, the samples were left undisturbed for at least four weeks to establish radioactive equilibrium in the ^{226}Ra decay chain segment. Each sample was measured for 3600 seconds with a statistical uncertainty generally less than 10% for eU. Less than 2% of the measurements are below the minimum detection activity of $\sim$ 2.5 Bq/kg.

With the purpose to test the performances of ZaNaI in a complex geological context, 368 in situ gamma-ray measurements with an acquisition live time of 300 seconds were performed on granitic outcrops (Figure 5.2) comparing the results with the data obtained by MCA rad. According to the FSA-NNLS method, each spectrum was reconstructed from a linear combination of standard spectra for ^{238}U, ^{232}Th, ^{40}K, ^{137}Cs and for the background. The uncertainty of the method is estimated to be 5% for ^{40}K and 7% for ^{232}Th, with relatively higher uncertainty for ^{238}U of approximately 15%. In [86], the coefficient of correlation (0.87 ± 0.12) between the eU values obtained by NaI(Tl) and HPGe is compatible with the unity at the 1 sigma level. Despite this strong agreement between the two acquisition methods, it is well known [109] that in-situ gamma ray measurements are susceptible to many sources of 'noise': the geometry of the investigated area, the presence of atmospheric radon, the soil moisture content, the weathering and the outcrop exposure can affect the gamma signal, decreasing the precision of the survey.

Because the field measurements are included in this study, relevant precautions were taken to ensure the reliability of the data. Indeed, the acquisition of data was avoided immediately after rainfall and preferred flat outcrops far from man-made constructions (Figure 5.2). In the U decay chain, disequilibrium occurs when one or more isotopes are completely or partially removed or added to the system. Because gamma ray spectroscopy is a method that detects the gamma emitter daughters of uranium, secular equilibrium of the decay chains is commonly assumed and is reported as the equivalent uranium (eU).

Figure 5.2: the ZaNaI detector during a geological survey in a remote area in Sardinia.

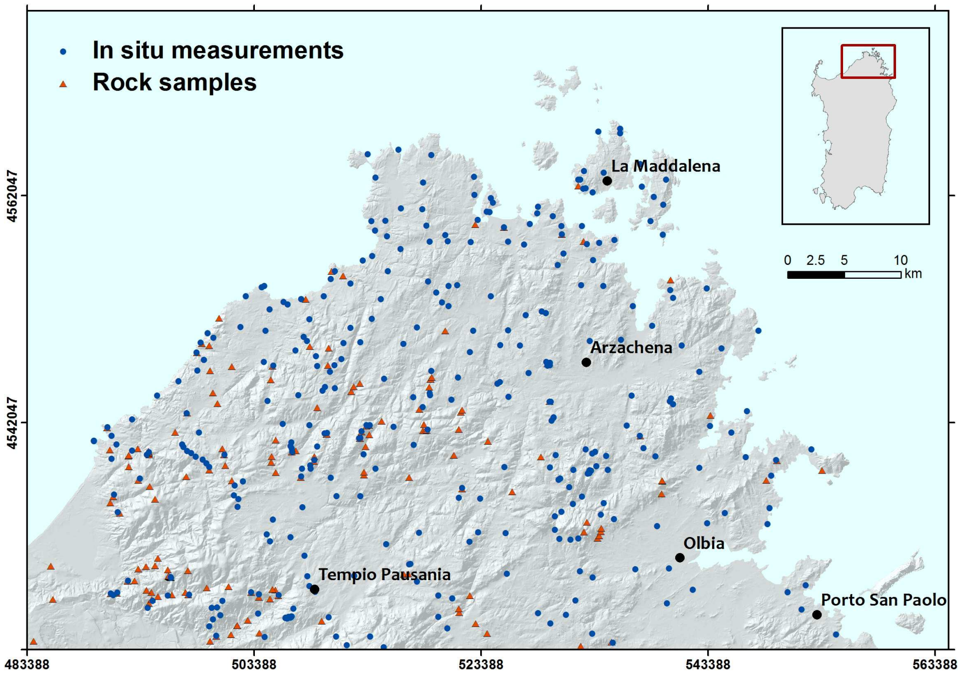

Figure 5.3: the locations of the 167 collected rock samples and the 368 in situ measurements (cartographic reference system WGS84 UTM ZONE 32N).

5.4 Mapping radiometric data

The map of the eU distribution in VBNS, a raster with a 100 m × 100 m spatial resolution, was obtained considering all 535 measurements acquired by HPGe and NaI(Tl) using the Kriging method. The frequency distribution and the principal statistical parameters of the input data and the output model are reported in the Main Map.

The exploratory statistics analysis highlights that the HPGe and NaI(Tl) data are characterized by frequency distributions (Figure 5.2) described by the statistical parameters reported in 5.1. The distributions are affected by a sampling bias because each lithology was not investigated by the same amount of records in the two datasets: this is particularly clear in observing the tails of the distributions. In fact, the quartzites and amphibolites of the metamorphic basement are characterized by the lowest uranium concentrations ($< 2\ \mu g/g$) and were mainly investigated with HPGe measurements because they are badly exposed and poorly suitable for in situ measurements. In contrast, the highest values in Figure 5.4 are found in the U-rich monzogranites ($\sim 9\ \mu g/g$) of the La Maddalena pluton [88], investigated mostly with in situ surveys.

Since the distribution of the input data shows a skewness value close to unity, the study of the spatial variability was performed without any normal transfor-

Table 5.1: uranium average abundance U ($\mu g/g$), standard deviation σ ($\mu g/g$) and goodness of fit (normalized χ^2) obtained with normal and lognormal probability density functions applied to all data and both datasets (i.e., HPGe and NaI(Tl)).

		Normal distribution		Lognormal distribution	
Dataset	Number of records	U ± σ ($\mu g/g$)	χ^2	U ± σ ($\mu g/g$)	χ^2
HpGe	167	3.5 ± 1.9	1.7	$2.9^{+3.3}_{-1.5}$	4.3
NaI(Tl)	368	5.2 ± 2.2	6.0	$4.8^{+2.4}_{-1.6}$	0.5
All data	535	4.7 ± 2.3	4.5	$4.1^{+3.3}_{-1.8}$	6.1

mation of the uranium abundances. A detailed analysis of the directional Experimental Semi-Variograms (ESV) highlighted an isotropic experimental variability without any preferred directions. Therefore, an omnidirectional ESV made up of 9 lags of 2.2 km was computed and modeled using a trial-and-error procedure (Figure 5.5). To study the small scale variability of U abundances, the parameters used for the ESV modeling were tuned for optimizing the fit in the first lags of the EVS. The nugget effect (1.7 $\mu g^2/g^2$), contributing approximately to 30% of the total amount of spatial variability, and the maximum distance of spatial variability equal to 4.8 km are in excellent agreement with the observed tendency of the experimental data. The goodness of fit of the ESV model was checked via the cross validation procedure. The results are reported in Table 5.1, together with the parameters of the structures of variability used for the ESV modeling.

The estimation process, performed with Geovariances ISATIS ® software, takes into account the overall uncertainties of the two methods of γ-ray measurements as the known Variance of Measurements Error of the input data. In particular, is considered an overall uncertainty of 5% for each HPGe measurement and a conservative uncertainty of 20% in the case of the NaI(Tl) measurements. This methodology, known as Kriging with Variance of Measurement Error, allows for assigning different weights to the input considering the degree of confidence of the measurements, thus improving the quality of the estimations [110].

The accuracy of the spatial model in terms of the variance normalized with respect to the estimated values is reported in the Main Map with the contour lines.

The chromatic variations in the color ramp of the legend were assigned to specific values of eU concentration. In particular, they correspond to the 20th, 35th, 45th, 55th, 65th, 75th, and 80th percentiles calculated on the entire dataset of 535 measurements.

Table 5.2: parameters of the structures of variability used for the model fitted on the ESV; results of the cross-validation procedure in terms of the Mean of Standardized Errors (MSE) and the Variance of Standardized Errors (VSE).

	ESV model parameters		Cross-validation results	
Structures of variability	Range (km)	Sill $\mu g/g^2$	MSE	VSE
Nugget effect model	-	1.7		
First Spherical model	3.4	2.4	-0.04	0.74
Second spherical model	13.8	0.8		

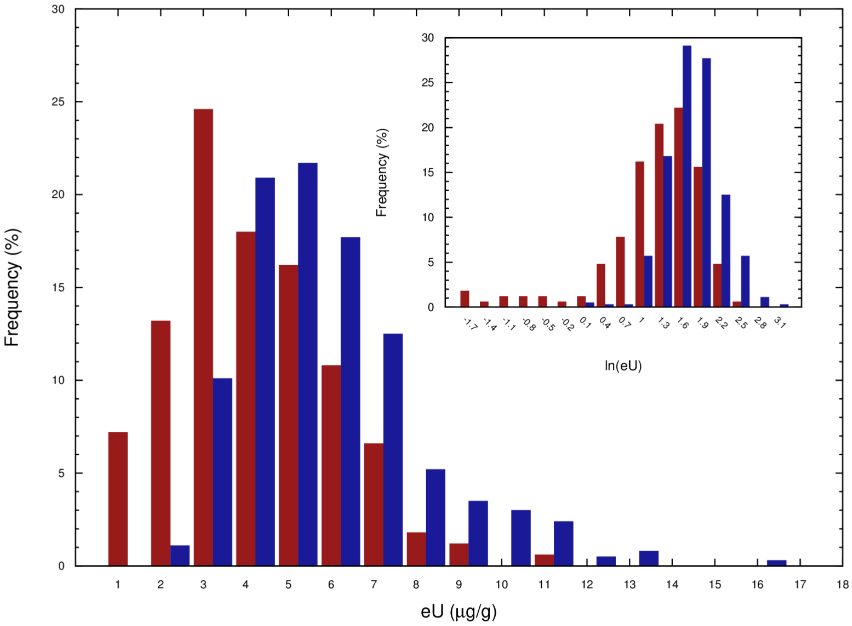

Figure 5.4: the frequency distributions of the eU abundances ($\mu g/g$) in rock samples (red) and in situ measurements (blue).

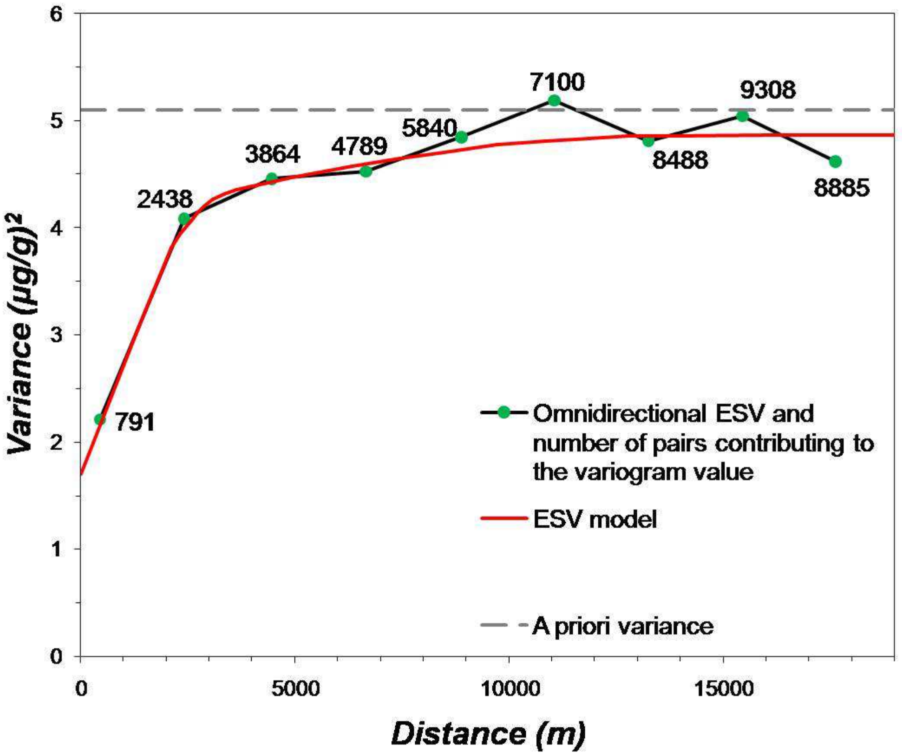

Figure 5.5: model fitted for the ESV calculated with 9 lags of 2.2 km.

5.5 Final remarks

This study present a 1:100,000 scale map of the eU abundance distribution in the Variscan Basement, which occupies a total area of 2100 km^2 in Northeastern Sardinia. The spatial model obtained performing Kriging on the 535 gamma-ray measurements is reported together with the uncertainties of the estimations.

Following a detailed statistical analysis performed on the input dataset consisting of 167 laboratory measurements (HPGe) and 368 in situ measurements (NaI(Tl)), the spatial variability of the eU abundance was studied with the computation and modeling of an omnidirectional Experimental Semi-Variogram (9 lags of 2.2 km). The map was obtained using the Kriging with a Variance of Measurement Error method, a geostatistical tool that allows for combining eU abundances with different levels of confidence associated with the two different gamma-ray spectroscopy methods.

The map shows the highest values in the granitoids of the La Maddalena pluton, where the eU content ranges between 6.2 and 9.3 $\mu g/g$. However, in the metamorphic basement, outcropping in the southwest of the study area (Figure 5.1), the presence of eclogites intruded in the migmatitic orthogneisses contributes to the lowest uranium abundances ($< 2\mu g/g$).

The results suggest that the distribution of the eU content is related to the Post-Variscan brittle structure, reported in [88], that affects the metamorphic units and the plutons of the VBNS. In particular, in the Tempio Pausania pluton (southwest of the study area), the major NE-SW faults correspond to anomalies in the eU distribution and mark an area with higher eU content (5 - 7 $\mu g/g$) compared to the adjacent sectors of the pluton with lower eU content (~ 3.5 $\mu g/g$).

In the AZN, the eU content increases in the more differentiated rocks. This behavior can be verified in the spatial model, even if the ranges of the estimated values for granodiorites, monzogranites and leuco-monzogranites are affected by the 'smoothing effect' typically associated with the Kriging method.

The presented map, integrated with available and more detailed geological maps, is a useful tool for studying the assembly of the intruded plutons and the relationships between the different petrological associations, based on the eU behavior during crustal magmatic processes. Indeed, the study of the eU distribution in the VBNS, particularly in the AZN, could help to refine existing models explaining the post-collisional magmatic processes of the southern European Variscides.

From this study it emerges that about 90% of the territory of the VBNS is characterized by eU concentrations higher than the average upper continental crust abundance (2.7 $\mu g/g$) [111]. Since Uranium rich rocks are generally the main source of radon, the presented distribution is a primary criterion for identifying radon-prone areas. Although radon migration depends on many geophysical parameters (e.g. porosity, fractures and permeability of rocks), the assessment of radon gas emission from the underlying bedrock is strongly recommended for mapping the Radon risk, which could be relevant in the coastal areas where the tourism enhances the population density especially in the summer.

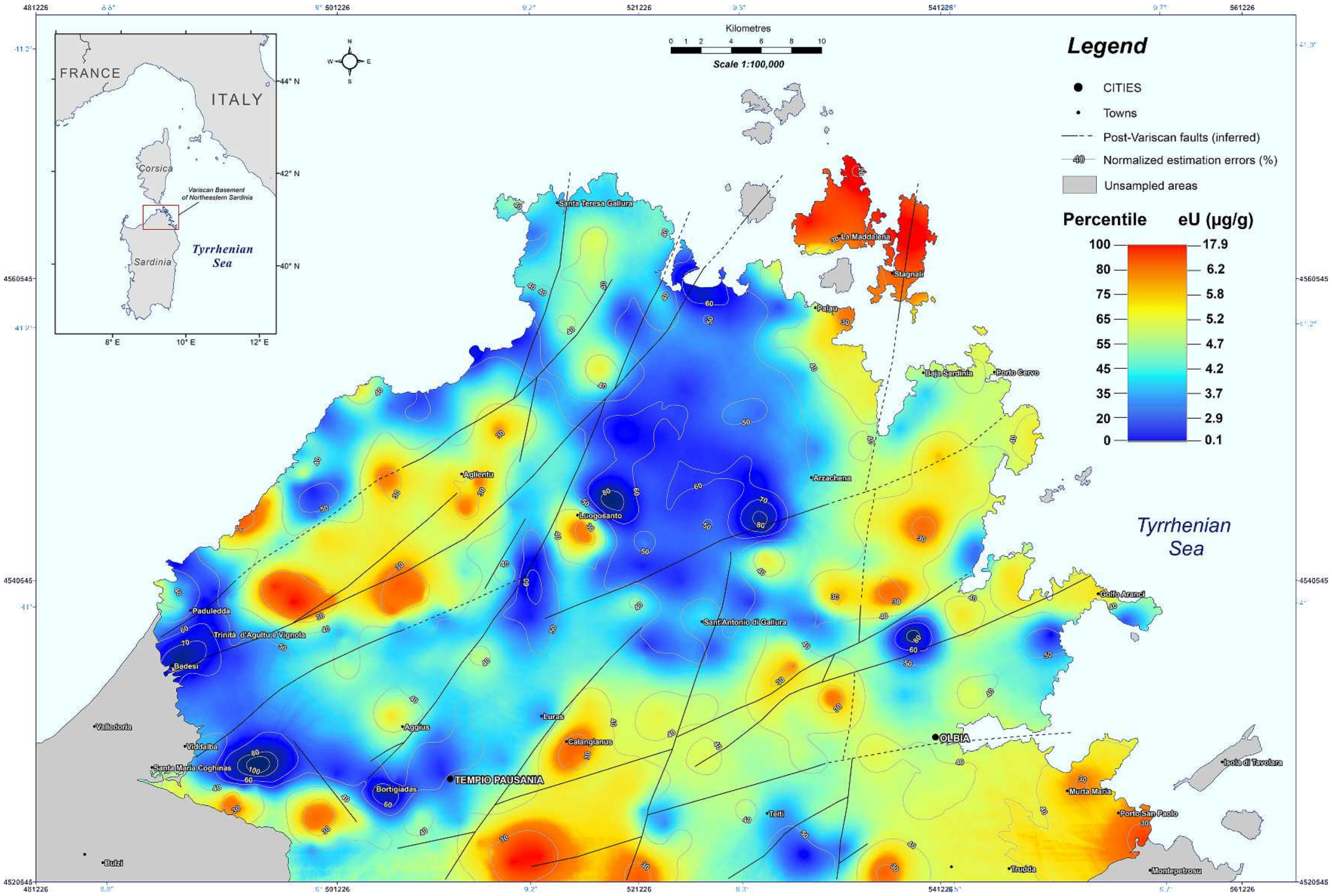

Figure 5.6: eU distribution map of the Varsican Basement of Northern Sardinia. The cromatic variations in the colo ramp of the legend correspond to 20th 35th 45th 65th 55th 75th and 80th percentiles calculated from the entire dataset of 535 measurement.

The content of this chapter is based on the following publication:

Kaçeli Xhixha M., **Alberi M.**, Baldoncini M., Bezzon G.P., Buso G.P., Callegari I., Casini L., Cuccuru S., Fiorentini G., Guastaldi E., Mantovani F., Mou L., Oggiano G., Puccini A., Rossi Alvarez C., Strati V., Xhixha G., Zanon A. V.“ *Uranium distribution in the Variscan Basement of Northeastern Sardinia*” Journal of Maps (2015). DOI:10.1080/17445647.2015.1115784 (IF: 1.435)

Chapter 6

Undergraduate student educational laboratories with γ-ray spectrometer

6.1 Introduction

The Summer School in Nuclear Physics and Technologies was born and developed from an international cooperation between the University of Ferrara (Italy) and the Cockrell School of Engineering at the University of Texas at Austin (USA). Addressed to almost all undergraduate students from the University of Texas, it is an educational training lasting a month and dedicated to the comprehension of the physics phenomenon of radioactivity and to the applications of nuclear and radiation physics.

The educational activities include lectures and laboratory group experiences aimed at providing the basic concepts of nuclear physics and at the same time at introducing frontier technologies and topics.

In this educational experience, it was possible to test the usability of the ZaNaI and to have student feedback on its ease of use. This experience was important to develop and update the graphical interfaces and the features of the smart-phone application that manage the multichannel analyzer Gamma stream.

In this chapter are presented two group activities focused on $\gamma - ray$ spectroscopy, carried on during the Summer School and detailed in table 6.1. The activities are conceived as hands-on experiments with a duration of 4 hours and are addressed to a group of 5/8 students.

Table 6.1: the supplies (equipment and software) necessary for the two experiments carried on during the Summer School together with the educational aims.

Experiment	**Equipment and software**	**educational aims**
Laboratory I: introduction to the gamma ray interaction with matter	• 1L NaI(Tl) detector with Multi Channel Analyzer (MCA) gstream by CAEN • Tablet and smartphone • 5 cm thick lead slabs • Radioactive source (^{137}Cs) • Aluminium layers	• Learning how to manipulate a $\gamma - ray$ spectrum acquired with a scintillation detector • Comprehension of the high penetration capacity of gamma photons, calculating attenuation coefficients
Laboratory II: investigate the outdoor natural radioactivity using a portable γ-ray spectrometer	• 1L NaI(Tl) detector with Multi Channel Analyzer (MCA) gstream by CAEN • Tablet and smartphone • GammaTouch application • Google Maps • Google Earth	• Learning how to design and perform in-situ $\gamma - ray$ spectrometry measurements • Critical comprehension of all accidental factors which make an in-situ g-ray survey a complex issue

6.2 Theoretical outline

Radioactivity is a physical phenomenon occurring when the unstable nucleus of an atom reaches a new condition of stability. Radiation can be found everywhere, starting from the first moments of life of our universe. In particular, terrestrial radiation is mostly due to three isotopes of uranium, thorium and potassium: ^{238}U, ^{232}Th, ^{40}K (and all their daughter products), which are relatively common in the Earth's crust. The activity of a radioactive material is measured in Bq/kg, defined as one decay per second per unit mass. ^{238}U and ^{232}Th produce decay chains that comprise isotopes decaying α, β or γ radiation. The γ decay occurs when a nucleus in an excited state, often produced by a previous decay, emits a low (tens of keV) or high energy (1-3 MeV) photon, called gamma, in order to reach a more stable configuration. These photons belong to a region of the electromagnetic spectrum characterized by energies higher than that of the visible light: as a consequence they are invisible to our eyes and a detector is needed in order to reveal them. In these experiments we use a sodium iodide (NaI) scintillator based detector, which is able to discriminate photons energies and therefore to measure a $\gamma - ray$ spectrum. The typical unit of measurement of energy used in gamma spectroscopy is the keV (kiloelectronvolt), corresponding to $1.602 \cdot 10^{-16}$ Joules, or the MeV (10^3 keV). In a gamma spectrum it is possible to identify two energy regions: above 3 MeV there are only gammas of cosmic origin, while below there are also terrestrial gammas.

^{238}U has a half-life of $4.47 \cdot 10^9$ years and its decay chain involves 18 unstable isotopes among which the main gamma emitters are: ^{234m}Pa, ^{214}Pb and ^{214}Bi. ^{232}Th has a half-life of $1.41 \cdot 10^{10}$ years, its decay chain includes 12 unstable isotopes among which the main gamma emitters are: ^{228}Ac, ^{212}Pb, ^{212}Bi and ^{208}Tl. Here we measure ^{214}Bi and ^{208}Tl by monitoring gamma lines having an energy of 1764 keV and 2614 keV, respectively. The gamma signal at 1460 keV produced by photons from the ^{40}K decay is a typical feature of the environmental gamma spectrum.

A photon can interact with matter mainly via three phenomena: the photoelectric effect, the Compton scattering and the pair production-annihilation [112]. Through these phenomena the energy of the gammas is deposited in the NaI detector. Successively, the signal is amplified and analysed by the electronics which assigns the recorded events to histogram channels of increasing energy, giving rise to a gamma spectrum (Figure 6.1(b)).

Figure 6.1(a) shows how the relative contributions of the three interaction mechanisms change with the gamma energy. The photoelectric effect is predominant for low energies and arises from the absorption of a photon by an atom and the ejection of an electron from one of the atomic bound shells. The Compton scattering is the main interaction mechanism of terrestrial gamma photons as it dominates at intermediate energies ($\sim$ 1 MeV).

This occurs when an incident photon collides with an atomic electron deflecting from its initial direction and losing part of its energy that is transferred to the electron itself as kinetic energy. Since the energy loss varies with the photon incident angle, gamma photons can emerge after a single collision with a wide range of energies, producing a continuum in the gamma spectrum, called Compton continuum. The pair production process corresponds to the conversion of a gamma photon into an electron-positron pair and occurs only if the gamma has a minimum energy equal to the mass of the particle pair (2me = 1022 keV). A typical shape that can be observed in a $\gamma - ray$-ray spectrum is the so-called photopeak, which is populated by those events in which a gamma photon having energy equal to the one of the decay impinges on the scintillator releasing inside the detector all of its energy.

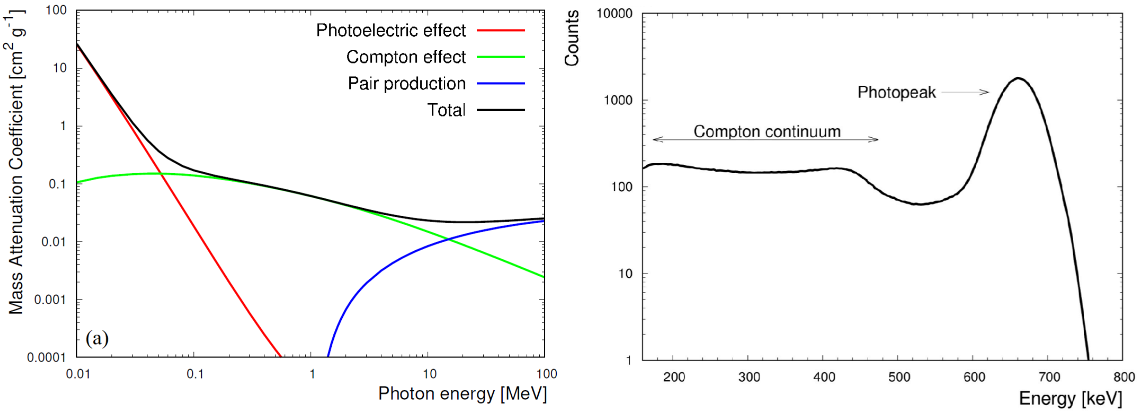

Figure 6.1: (a) mass attenuation coefficient $\mu_{m}ass$ for aluminium as function of the photon energy (source: https://physics.nist.gov) where the three contributions due to the photoelectric, Compton and pair production interactions are separately displayed. (b) Example of a ^{137}Cs gamma spectrum, the photopeak and the Compton continuum are visible.)

If one considers a gamma beam propagating in matter in the x direction and if N_0 corresponds to the initial number of radiated gammas, due to the interplay of the attenuating processes described before, a photon loss ΔN occurs, which is proportional to the covered distance Δx:

$$\Delta N = -\mu_m ass N_0 \rho \Delta x = -\mu N_0 \Delta x \tag{6.1}$$

with μ being the linear attenuation coefficient of the traversed material in cm-1, corresponding to the mass attenuation coefficient $\mu_m ass$ in cm^2/g (see Figure 6.1) multiplied by the material density ρ in g/cm^3. The linear attenuation coefficient represents the inverse of the distance at which the number of photons is reduced by a factor 1/e, as can be inferred by the following equation [113]:

$$\Delta N = N_0 e^{-\mu x} \tag{6.2}$$

This theory can be experimentally tested by surrounding a point-like radioactive source with a lead box having a small hole on one side, which is meant to produce a collimating effect on the radiated photons. This project has the aim of making the students think about the concept of detector field of view (Figure 6.2), which is essentially ruled by Eq. 6.2. In particular, a point-like source of $137Cs$, shallow layers of natural soils and environmental background can be seen respectively as a 1D, 2D and 3D source of radioactivity that can be detected by the equipment.

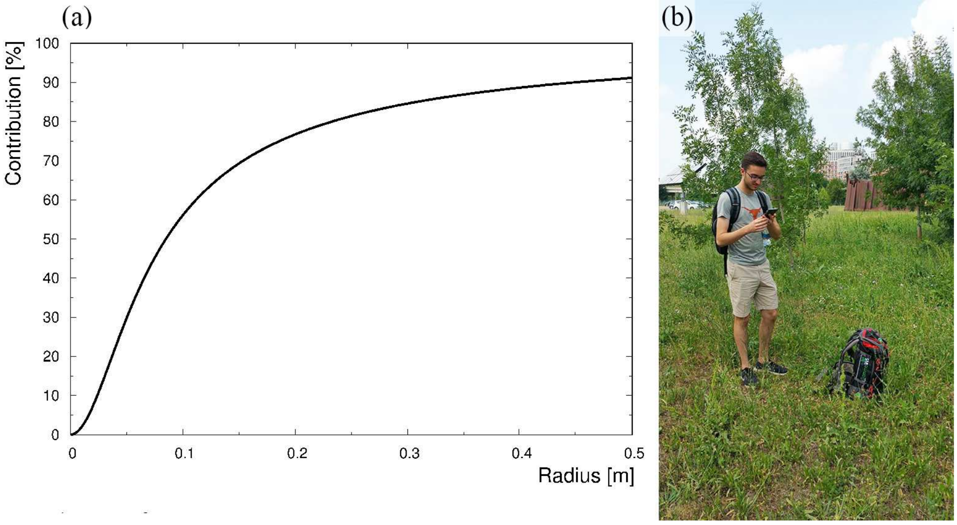

Figure 6.2: field of view: (a) percentage cumulative contribution of soil radioactivity as function of the radial distance from the detector position, assuming a homogeneous soil radioactive content and that the detector is placed at ground level; (b) a student during the acquisition of a spectrum.

6.3 Laboratory I: introduction to the gamma ray interaction with matter

In this experiment the students learn to perform an environmental γ-ray spectroscopy measurement, handle the acquired spectrum by retrieving counting statistics information and, finally, determine the linear attenuation coefficient of a given material by modelling the absorption of gamma photons emitted by a collimated point-like ^{137}Cs source [114]. This educational experience has the aim of enhancing the knowledge about radioactivity in terms of both natural and artificial sources as well as making the students directly experience the high penetration of γ-rays in matter, which makes this radiation ideal for proximal and remote environmental monitoring.

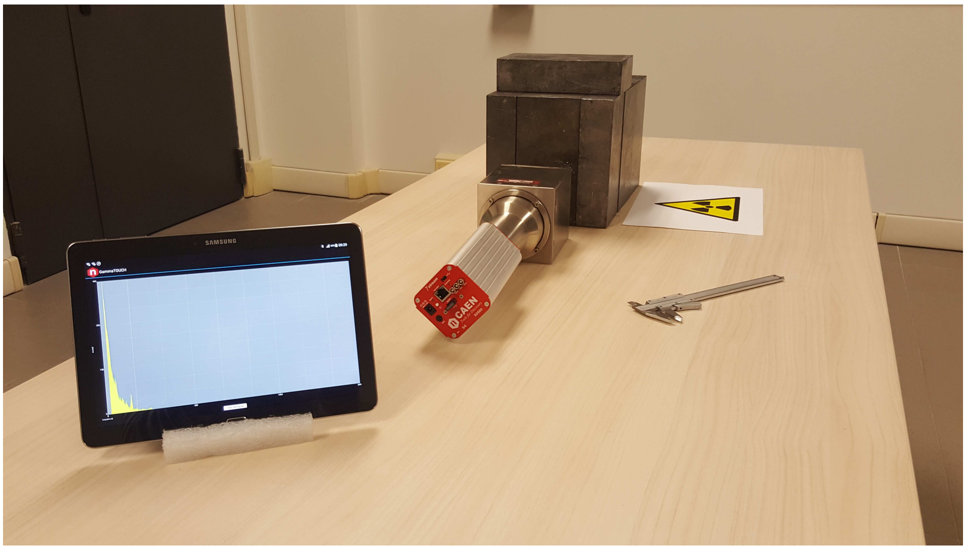

Figure 6.3: the experimental setup: on the left the tablet showing the graphical interface of the GammaTOUCH app during the acquisition, on the right the 1L NaI(Tl) scintillator based detector and the lead box.

The experimental setup consists in a 1L NaI(Tl) scintillator, a photomultiplier tube (PMT) and a digital multichannel analyzer (MCA, γstream by CAEN), as shown in Figure 6.3. This detector is particularly versatile as it reliably complies with a variety of experimental and environmental conditions. Indeed, as NaI(Tl) crystals are characterized by a relatively high scintillation efficiency, the detector is able to collect sufficient statistics in a short time, also providing a good enough energy resolution for the radionuclide identification. The PMT, coupled to the NaI(Tl) crystal, converts each photon into a small current which is subsequently amplified and transformed into a voltage pulse proportional to the energy deposited by the gamma photon inside the crystal itself. The MCA in turn converts the pulse into a channel whose number is proportional to the magnitude of the voltage pulse. Each channel is consequently populated with the corresponding number of recorded events, giving rise to a γ-ray spectrum (i.e. a frequency histogram of the events classified according to their energies) in which 1024 different energies can be distinguished. The γstream can be operated via the Android app GammaTOUCH, which uses a Bluetooth communication protocol: this application allows the user to set the operating voltage, specify the acquisition time and start the measurement.

The environmental measurement is launched by setting the γstream operating voltage to 850 V and the acquisition time to 800 seconds. The graphic interface of the GammaTOUCH app continuously updates the histogram shape by showing the cumulative number of events over time. This preliminary step helps the students identify the main photopeaks and distinguish them from local fluctuations, as well as to start decrypting the information encoded in the different energy ranges. When the acquisition ends, the spectrum is saved in an ASCII file which lists in a single column the number of events for each channel and which can be opened and manipulated in an Excel spreadsheet.

A dedicated Android app performs the energy calibration of the spectrum (see Figure 6.4), which allows to convert the acquisition channels into energy deposited inside the detector according to the following equation:

$$E = m \cdot ch + q \tag{6.3}$$

where E is the energy in keV corresponding to the channel ch, m is the gain in keV/ch, i.e. the width in keV of a single acquisition channel, and q is the intercept in keV, corresponding to the energy of the first channel.

The energy calibration procedure is based on the reconstruction of the Gaussian shapes of the ^{40}K and ^{208}Tl photopeaks corresponding respectively to the 1460 keV and 2614 keV gamma emissions. Knowing the energies of the gamma emission and the channels corresponding to the Gaussian means, the slope and intercept of the linear relation given by Eq. 6.3 are calculated, shown in the app graphic interface (see Figure 6.4) and subsequently used by the students to integrate the counts of measured spectra in the energy windows of interest (see Figure 6.5).

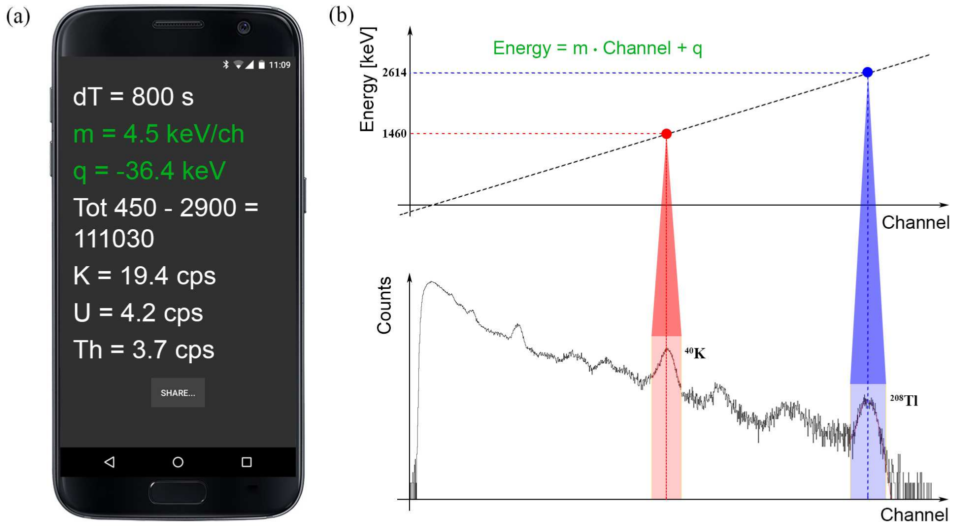

dT = 800 s
m = 4.5 keV/ch
q = -36.4 keV
Tot 450 - 2900 = 111030
K = 19.4 cps
U = 4.2 cps
Th = 3.7 cps

Figure 6.4: (a) screenshot of the output of the Android app performing the energy calibration of the gamma spectrum: m and q represent respectively the slope and the intercept of the linear function (b) determined on the base of the Gaussian reconstruction of the ^{40}K and ^{208}Tl photopeaks at 1460 keV and 2614 keV.

The integrated number of occurrences N for each of the four energy windows of interest [115] (Figure 6.5) is obtained by summing in Excel the number of counts N_i recorded in all the energy channels i of the specific window. The count rate n is then directly calculated by normalizing for the acquisition time T as n=N/T. In particular, at the end of this procedure, the students measured the count rate in the ^{137}Cs photopeak energy window in the absence of any ^{137}Cs source, which corresponds to what is later called background count rate n_{Cs-bkg}.

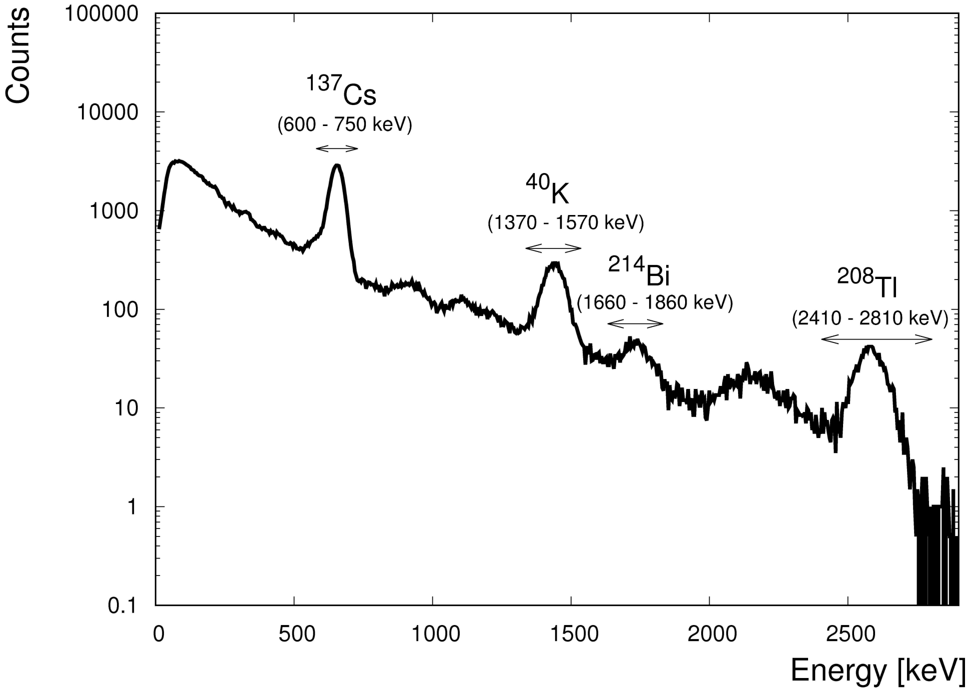

Figure 6.5: a 360 s γ-ray spectrum acquired in laboratory with a 1L NaI(Tl) detector in presence of a 137Cs point-like source: the most prominent photopeaks of ^{137}Cs point-like source: the most prominent photopeaks of ^{137}Cs, ^{40}K, ^{214}Bi (daughter of the ^{238}U decay series) and ^{208}Tl (daughter of the ^{232}Th decay series) are in evidence.

The goal of the second part of this laboratory is to derive the linear attenuation coefficient of aluminium by using a ^{137}Cs point-like source, which emits monochromatic gamma photons at 662 keV, and 16 aluminium layers, each one having a thickness of 2.9 mm. The source is located inside a lead shielding box at a distance of 46.4 mm from the crystal bottom, which corresponds to the full thickness of all the aluminium attenuating layers (figure 6(a)). The lead box has a 0.5 cm diameter hole which allows to collimate the gamma radiation in order to reproduce the mono-directional boundary condition described in section 6.3 (see Eq. 6.1 and 6.2).

Once the experimental setup is ready, the first 360 s acquisition is started in absence of any attenuating layer. Then, the 8 successive 360 s acquisitions are performed by adding each time two aluminium layers until, in the last measurement, the space between the detector and the source is completely filled (see figure 6(a)).

The net count rate in the ^{137}Cs photopeak n is obtained by subtracting to the total count rate ntotal, measured in presence of a given aluminium thickness, the background count rate n_{Cs-bkg}, measured during the environmental background acquisition. The net count rate measured in absence of any attenuating material n_0 is used as normalization factor for each measurement performed in the presence of aluminium layers, in order to calculate for each configuration the ratio n/n_0 , which is plotted versus the layer thickness (Figure 6.6).

The Excel fitting tool is employed in order to reconstruct the exponential trend of the ratio n/n_0 as function of the total thickness of aluminium layers from which the students retrieve the value of the aluminium linear attenuation coefficient μ as in 6.2.

The obtained result ($0.184\ \mathrm{cm}^{-1}$) is compared with the literature value of $0.207\ \mathrm{cm}^{-1}$ and with the $9.52 \cdot 10^{-5}\ \mathrm{cm}^{-1}$ value referred to air (National Institute of Standards and Technology's database website https://physics.nist.gov). The students discuss critically the results, trying to justify potential differences between experimental and reference value (due for instance to the presence of the stainless steel crystal housing or to the imperfect collimating effect of the hole in the lead shielding box) and understanding the potential of gamma ray spectroscopy in remote sensing. The discussion is also instrumental in making the students master the concepts of highly penetrating nature of the gamma radiation and of the dependence of the linear attenuation coefficient on the type of the attenuating material as well as on the energy of the photons.

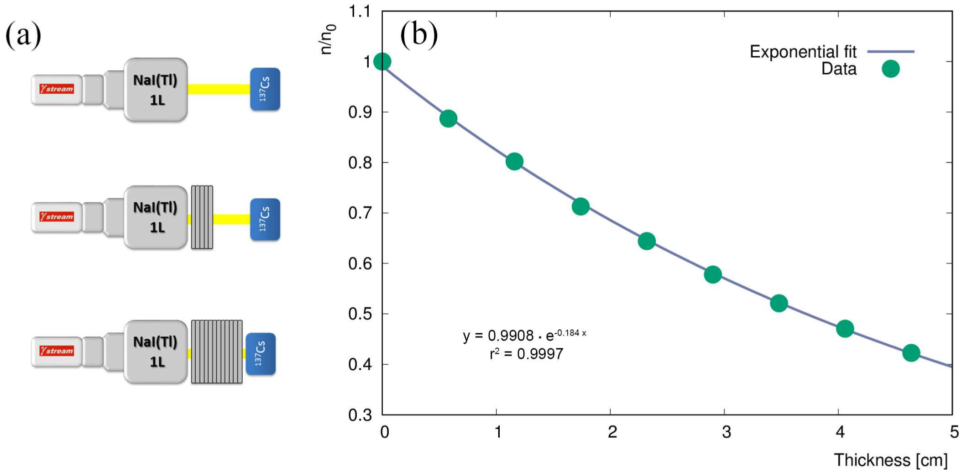

Figure 6.6: a scheme of the different experimental steps carried out for the determination of the aluminium linear attenuation coefficient. The students perform successive acquisitions by adding each time aluminium layers till the space between the detector and the ^{137}Cs pointlike source is completely filled; (b) plot of the exponential attenuation with increasing aluminium thickness of the net count rate in the ^{137}Cs energy window normalized to the count rate in absence of any aluminium layer. The students experimentally measured the data used to determine the green points and reconstructed the exponential trend reported with the blue curve representing the fit function from which the experimental aluminium attenuation coefficient ($0.184\ \mathrm{cm}^{-1}$) was retrieved.

6.4 Laboratory II: investigate the outdoor natural radioactivity with the ZaNaI

The second laboratory is dedicated to the measurement of outdoor natural radioactivity and has the aim of making the students familiar with different levels of terrestrial gamma radiation in the environment. Unlike a laboratory experience, in the outside environment it is impossible to manage all the parameters characterizing the experimental conditions. In the specific case of in-situ γ-ray spectroscopy, there are many variables that could interfere with the measurement: the presence of vegetation or of buildings and the morphology of the area affect the field of view of the spectrometer (Figure 6.2(a)) [85], [28], soil humidity has a damping effect on gamma radiation and sources having weak intensities need longer acquisition times. In order to compensate for these potential nuisances, having a well established measurement procedure could help in minimizing the effects of outdoor factors. In this sense, students are stimulated to carefully adhere to the acquisition procedure, which comprises taking notes of all the relevant experimental conditions, especially in terms of their potential impact on the experimental outcomes.

The ZaNaI detector has been employed for the outdoor survey. In outdoor campaigns the potential of the instrument is fully exploited, as performing the measurement with just the use of a tablet simplifies and quickens the data taking operations.

The in-situ survey is planned while keeping in mind the spatial resolution of the desired information. When possible, the best strategy is to choose sampling points on a regular grid, covering homogeneously the surveyed area for the different types of ground coverage like asphalt, grass or brick. A map of the measurement points located in and around the campus (Figure 6.7 (a)) has been previously loaded in the Google Maps app of a smartphone. For each measurement point, a 180 s acquisition is performed, a picture of the area surrounding the detector is shoot and the measurement sheet is compiled with GPS coordinates, type of ground coverage and the measurement ID provided by the GammaTOUCH app. Knowing the detector field of view (Figure 6.2(a)), the students place the backpack at sufficient distance from vertical structures (walls, trees) and avoid standing close to the instrument during the acquisition, in order to minimize both the attenuation and the radiation emission effects of their bodies. During the data acquisition, the students are encouraged to ask questions, make suppositions about the effects that a change in atmospheric conditions or soil humidity may cause in the measurement or about the type of ground coverage that would be the most or least abundant in natural radioactivity and why.

Once all the measurements are performed, the experimental results, together with the information related to the data taking conditions, are organized in an

Excel file. The analysis is performed with a dedicated Android app which reads and processes the spectra stored in the γstream internal memory. In particular, the software performs the energy calibration of the spectra, retrieves the total counts in the ^{40}K, ^{214}Bi and ^{208}Tlenergy windows of interest (see Figure 6.5) and applies the so called Window Analysis Method [116] based on a stripping technique in order to convert count rates to K, U and Th concentrations. The total specific activity A in Bq/kg due to the terrestrial radionuclides radiation is then determined as [116].

$$A = 313 \cdot K + 12.35 \cdot U + 4.06 \cdot Th \tag{6.4}$$

where K is the potassium concentration in 10^{-2} g/g and U and Th are the uranium and thorium concentrations in μg/g. The relevant information are transferred to a WebGIS platform and used to create a kml file (see supplementary material), a Google Earth supported format suitable for open access on-line publication. The kml file reports the measurement points, each one assigned with the corresponding natural radioactivity content and with a picture of the area (Figure 6.8). By inspecting the data reported in the kml file the students are able to discuss the results, understand how radioactivity is spatially distributed and how it relates to the ground coverage type. The transfer of the data in a WebGIS platform allows not only to have a spatial visualisation, but also the spread of the results to a wider audience.

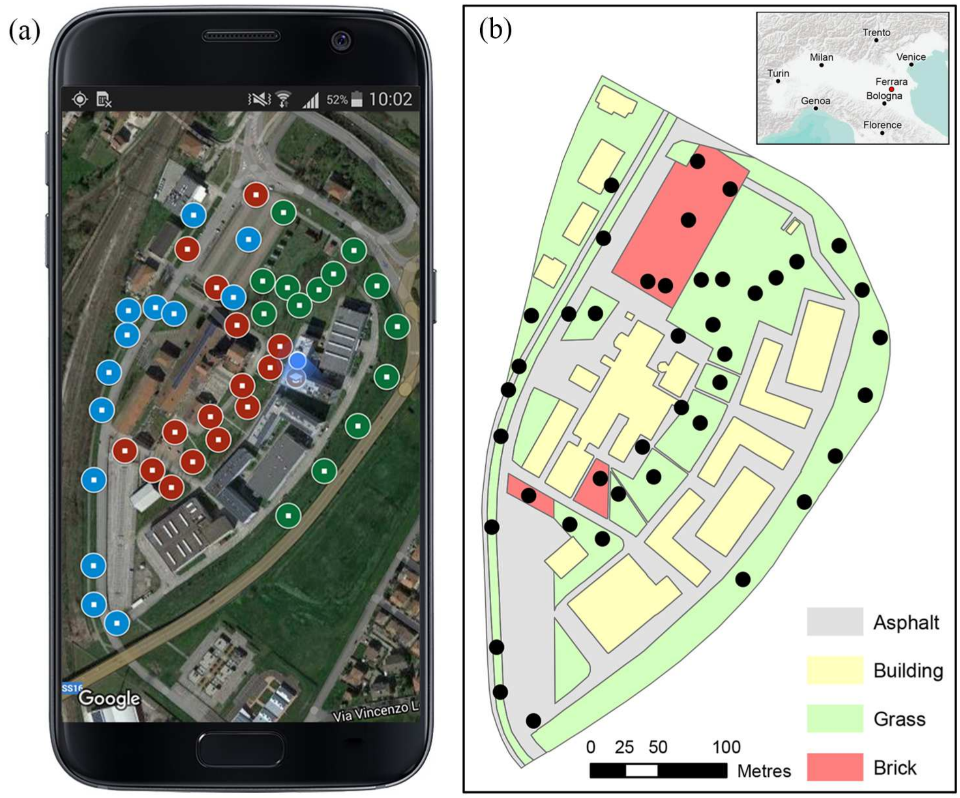

Figure 6.7: (a) planned measurement points reported in the Google Maps app: the different colours represent the three teams in which the students have been grouped. (b) Map of the campus structure with the measurement points (in black): the different colours indicate different types of ground coverage.

6.5 Final remarks

The educational experiences presented in this paper provide a successful example of the effectiveness of performing γ-ray spectroscopy measurements for conveying basic concepts related to the phenomenon of radioactivity. During the experimental activities the students had the opportunity of getting familiar with the physics of gamma radiation while becoming aware of being surrounded by radioactivity and being themselves natural sources of it. In performing the indoor and the outdoor measurements the students learnt how to use advanced tools for the environmental radioactivity monitoring, both at the hardware and at the software level.

The gamma radiometric acquisition was discussed in all the relevant aspects, from the interpretation of the distinct features of the spectrum to the critical inspection of the experimental conditions that can potentially affect the outcomes of the measurement. In the elaboration of the experimental data the students are called to collaboratively work in teams in order to extract from the acquired spectra quantitative information on the attenuating properties or on the radioactive content characterizing a given material or different types of ground coverage.

During the indoor experience the students learnt to interpret a γ-ray spectrum by identifying the distinct spectral features of the Compton continuum and of the photopeak, the latter being a clear footprint for distinguishing natural and artificial sources of radiation. Furthermore, the students quantitatively assessed the high penetration nature of gamma radiation by estimating the linear attenuation coefficient of aluminium and by comparing it with the reference value and with that of air.

The measurements performed during the outdoor survey are used to create a map (Figure 6.8) of the natural radioactivity of the campus and a Google Earth kml file for open access on-line publication. The data spatialization is performed by adopting a multivariate geostatistical interpolator, the Collocated CoKriging [28], which estimates the radioactivity in the areas among measurement points by taking into account not only the distance but also the different types of ground coverage.

Higher values of specific activity are found for grass covered areas (708 ± 108 Bq/kg), while pavement materials are characterized by activity values lower than 444 Bq/kg. These results did not match the students' expectations, reflecting their preconception about the exclusively artificial nature of radioactivity. This hands-on experience indeed was particularly effective in making the students perceive the omnipresence of radioactivity in the natural environment.

Finally, the course assessment questionnaires proved a positive feedback from the students regarding the educational content of the activities as well as the teaching methodologies and the advice arising from the students have been helpful to improve the ZaNaI system.

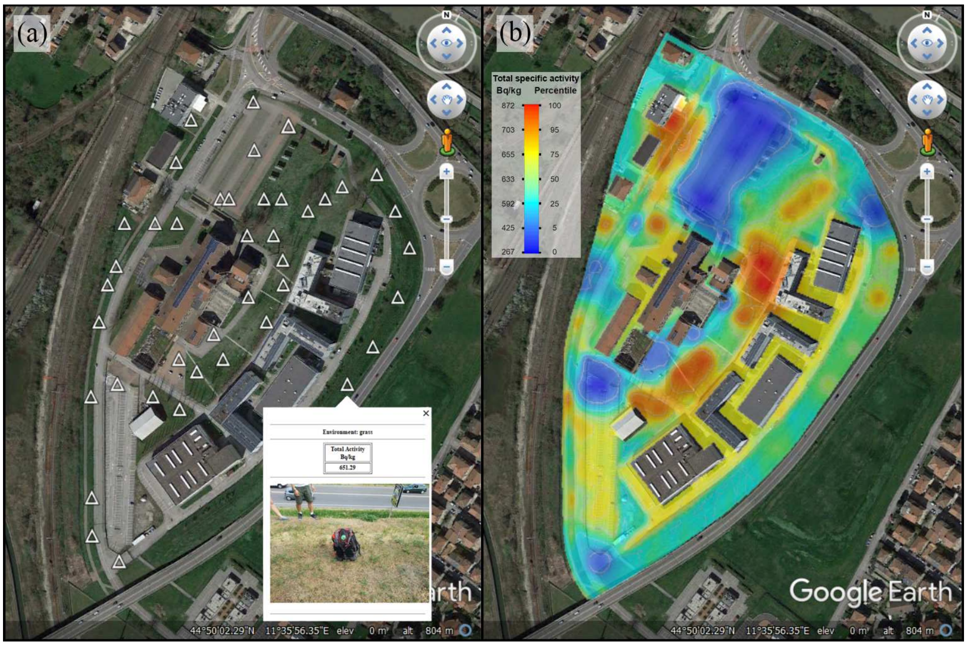

Figure 6.8: WebGIS of the natural radioactivity of the campus: (a) the triangles reports the measurement points: by clicking on them a box containing the information gathered by the students shows up; (b) map of the natural radioactivity of the campus obtained interpolating the total specific activity measured in the points reported in panel (a).

The content of this chapter is based on the following publication:

Alberi M., Baldoncini M.,Bottardi C., Chiarelli E., S. Landsberger, Raptis K.G.C., Strati V., Mantovani F.“*A Ghostbusters training: hunting for the spectral radioactivity*” submitted to European Journal of Physics (IF: 0.614).

Part III

Water content in agricultural soil investigated with gamma ray spectroscopy

Introduction

Agriculture accounts for as much as 70% of total freshwater consumption and climate change is having a considerable impact on the availability of water resources for agricultural production [117]. The future water management represent a challenge and is also expected to play an increasingly central role for the next generations. In this scenario new technologies and technique must be develop to optimize agricultural water management practices that support the intensification of crop production and the preservation of natural resources.

Determining and monitoring the quantity of water held by a soil destined to agriculture purposes is a key point to figure out plant available moisture. In the evolution of irrigation techniques, water management became important and requires continuous monitoring of water content in the soil. Measuring and monitoring soil water status methods are divided into two main categories: direct methods and field methods.

Direct methods consists of removing a sample by augering into the soil and then determining its moist and dry weights placing the sample in an oven at 105^o C.

Field methods estimate soil moisture by a calibrated relationship with some other measured variable. Among the volumetric field methods, i.e. those that estimate the volume of water in a sample volume of undisturbed soil (θ), are the neutron moderation methods. Its working principle consists in fast neutrons which are emitted from a decaying radioactive source. When they collide with particles with the same mass as a neutron (protons, H^+), they slow down dramatically, building a "cloud" of "thermalized" (slowed) neutrons. Since water is the main source of hydrogen in most soils, the density of slowed neutrons formed around the probe is proportional to the volume fraction of water present in the soil.

The dielectric techniques estimate soil water content by measuring the dielectric constant (K) which determines the velocity of an electromagnetic wave or pulse through the soil. The principal dielectric methods are time domain reflectometry (TDR), capacitance and frequency domain reflectometry (FDR), amplitude domain reflectometry (ADR), phase transmission and time domain transmission (TDM) [118].

This work is focused on the gamma spectroscopy indirect techniques. This method estimates water content by measuring the gamma photons in the 0.3-3 MeV energy range emitted from the radionuclide in the soil. The water content in the soil is inversely proportional to the gamma ray emission measured by the gamma spectrometer: photon survival probability depends on their energy, the chemical composition and the density of the crossed medium, the presence of moisture in the soil causes an effective increase in density, resulting in an increased attenuation of the gamma flux.

With the aim of measuring the water content in the first 20 cm of soil of an area of 0.2 ha during my PhD I contributed to the development and placement of a permanent gamma station equipped with a NaI(Tl) gamma spectrometer (see Figure 6.9). The gamma station is flanked by a weather station equipped with thermo-hygrometer, solar pyranometer, ultraviolet radiation sensor, anemometer, rain collector and barometer. Both stations are located in a field of tomatoes.

During the acquisitions I collected samples to calibrate the spectrometer and characterize the soil. With the help of analytical methods and Montecarlo simulations, taking into account the variation of environmental parameters and the attenuation effect produced by plant growth, the field water content was estimated. The measure highlighting a strong sensitivity to the precipitation phenomenon and the wet and dry soil curves are clear visible. The results obtained were compared with two suites of soil water balance and crop modelling systems: CRITERIA and Aquacrop demonstrating a good agreement between the measurements and the models. A theoretical outline is presented in Chapter 7, the equipment and the results are presented in Chapter 8 and 9.1.

Figure 6.9: installation of NaI(Tl) spectrometer inside the gamma station

Chapter 7

Physical characteristics of soils

7.1 Soil: a three phase system

Soil is made up of a heterogeneous mixture of inorganic and organic particles, composed of three phases: liquid, solid and gaseous. The solid phase of soil, mainly made up of inorganic matter, contains particles of widely varying sizes, shapes and chemical composition. The inorganic matter comprises two types of soil particles: primary and secondary. Primary particles cannot be subdivided and they form secondary particles

The spaces between solid particles, called pores, are filled with liquids and gases. The liquids (also called soil solution) will be principally water which contains many chemicals coming from the solution of soil minerals or from surface, ions commonly found in solution include Na^+ K^+ Ca^{2+} Mg^{2+} Cl^- $NO^-{}_3$ and SO^+. Most of them are plant macro and micro nutrients. Local conditions and soil properties will determine the mobility and the specific kind of bound of the water within the soil. The soil solution may fill the soil pores either completely or partly. In the former case, the soil is said to be “saturated”. In the latter “unsaturated” case, the soil solution occurs as thin films along particle surfaces, as annular wedges around contact points of particles and as isolated bodies in narrow pore passages.

The gaseous phase, also known as soil air or soil atmosphere, is composed mainly of N_2, O_2, water vapour and CO_2, with traces of other gases.

Grain size is a quantitative aspect of the inorganic primary particles (or soil separates) that constitute the solid fraction. So, depending on the size distribution, soil separates are usually divided into four categories: gravel, sand, silt, and clay.

In pedology, soil texture refers to the proportions of sand, silt, and clay in the fine earth of a soil sample, which give a distinctive feel to the soil when handled, and which are defined by different classes of soil texture.

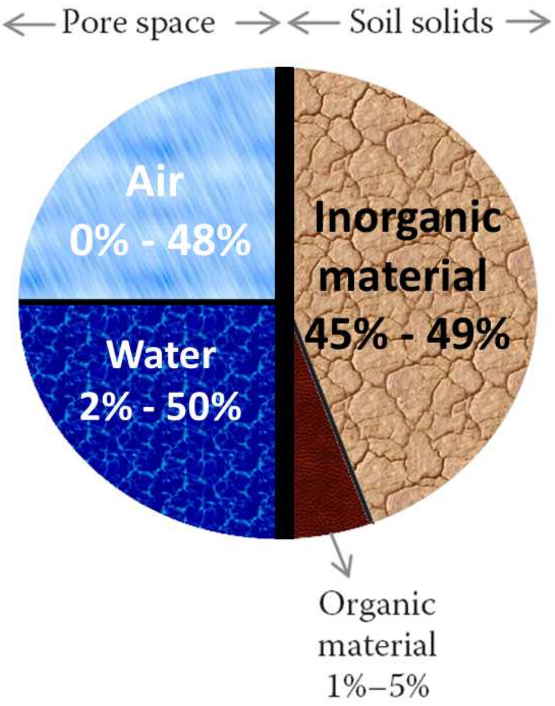

Figure 7.1: usual volume composition of soil (from [119])

Soil organic matter is any living or dead animal and plant material. It includes living plant roots and animals, plant and animal remains at various stages of decomposition, and microorganisms and their excretions. Organic solids form only a small fraction of the total solids, meanly lower than 5% of total soil by weight, but it plays an important role in numerous important soil processes that determine soil quality, its productivity, and environment moderation capacity. Soil organic matter has a high "plaint available" water retention capacity it can hold twenty times its weight in water [120].

Soil organic matter consists of a variety of components. Three categories of soil organic matter are recognized on the basis of the stages of decomposition: fresh or undecomposed, partially decomposed, and fully decomposed organic matter, together constitute the "active soil organic matter" (Table 7.1).

Table 7.1: different pools of soil organic matter depending upon the composition. From [120].

Pool		**Constituents**	**Mean residence time (years)**
Labile pool	Metabolic litter	plant and animal residues, cellulose	<0.5
	Structural litter	plants residues, lignin,polyphenol	0.5-2
Active pool		microbial biomass,simple carbonydrates enzymes	0.2-1.5
Intermediate pool		articulate organic matter	2-50
Recalcitrant pool		humic and fulvic acids,organo-mineral complexes	500-2000

7.2 Volume and mass relationships

The particle density is generally denoted by the symbol ρ_s and is also known as density of soil solids or true density. The definition of particle density states that it is the ratio of the mass of the soil solids to its volume (Figure 7.1):

$$\rho_s = \frac{mass\ of\ soil\ solids}{volume\ of\ soil\ solids} = \frac{M_s}{V_s} \tag{7.1}$$

In most mineral soils, the mean density of the particles varies between 2600 and 2700 kgm^{-3}, and is thus close to the density of quartz, which is often prevalent in sandy soils. The presence of iron oxides and heavy metals or solid organic materials can increase or decrease the value of particle density respectively.

On the other hand, bulk density (or dry bulk density) expresses the ratio between the mass of dried soil and its total volume (solids and pores together). It used to be symbolised by ρ_b and its mathematical expression is:

$$\rho_b = \frac{mass\ of\ soil\ solids}{total\ volume\ of\ soil} = \frac{M_s}{V_t} = \frac{M_s}{V_s + V_a + V_w} \tag{7.2}$$

Where V_a is the volume of soil gaseous phase (or air content) and V_w is the volume of liquids (Figure 7.1). In general, the mass of soil for bulk density determination is the mass after oven-drying the soil at 105° C for 24 hours. Obviously, ρ_b is always smaller than ρ_s, and if the pores constitute half the volume, ρ_b is half of ρ_s, namely 1300-1350 kg/m^{-3}. In sandy soils, ρ_b can be as high as 1600 kg/m^3, whereas in aggregated loams and in clay soils, it can be as low as 1100 kg/m^3.

The voids between the solid elements are called pores and liquid and gaseous components will fill them. The porosity is an index used to estimate the relative pore volume in the soil and is therefore expressed as a fraction or percent. Nevertheless, there are numerous ways to express it, the most interesting are the following:

- Total porosity (p_t): is the ratio of the volume of the pores (V_p or V_f in Figure 7.2), both connected (V_{cp}) and unconnected (V_{up}), to the total volume of soil.

$$p_t = \frac{total\ volume\ of\ pores}{total\ volume\ of\ soil} = \frac{V_a + V_w}{V_t} = \frac{V_{cp} + V_{up}}{V_t} \tag{7.3}$$

- Effective porosity (p_e): it is defined as the proportion of the rock which consists of interconnected pores.

$$p_e = \frac{total\ volume\ of\ pores}{total\ volume\ of\ soil} = \frac{V_{cp}}{V_t} \tag{7.4}$$

Depending on the kind of soil, the values of total and effective porosity can differ highly, effective porosity can be over one order of magnitude smaller than total porosity. Assuming that $V_u p \approx V_{clay}$ (volume of clay), in first approximation we can write:

$$p_t \approx p_e + \frac{V_{clay}}{V_t} \tag{7.5}$$

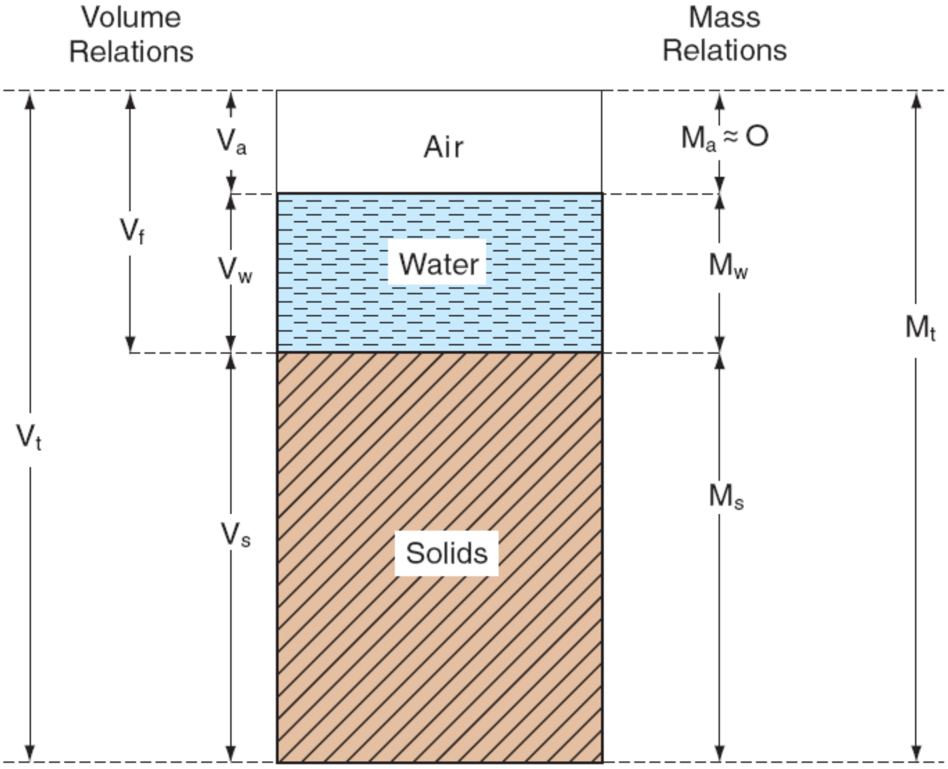

Figure 7.2: typical volume and mass notation of different parts of soil (from [121])

So in very clean sands, total porosity is equal to effective porosity. Hence, effective porosity is that portion of the total porosity available for fluid flow [122]. In Table 7.2 some range of values are shown, we can see that porosity can vary from zero or near zero to more than 65%. In general, for sedimentary materials, the higher the smaller the particle size, the higher the porosity 7.2.

There is a further relationship among particle density (Equation7.1), bulk density (Equation 7.2) and soil's total porosity (Equation 7.3):

$$p_t = 1 - \frac{\rho_s}{\rho_b} \tag{7.6}$$

Table 7.2: ranges of total porosity (p_t), effective porosity (p_e) of principal soil texture classes and some rocks [123].

	p_t [%]	p_e [%]
Gravel	24-40	13-40
Coarse sand	31-46	18-43
Fine sand	31-46	1-46
Silt	34-61	1-39
Clay	34-65	1-18
Sandstone	5-30	10-30
Siltstone	21-41	1-33
Crystalline rocks	0-10	–
Basalt	3-35	–
Weathered gabbro	42-45	0.8-1.7

Water may be present in soils with chemical compounds, on particle surfaces, in micro and macropores. There are three main general forms of water in soil: hygroscopic water, gravitational water and capillary water (Figure 7.3).

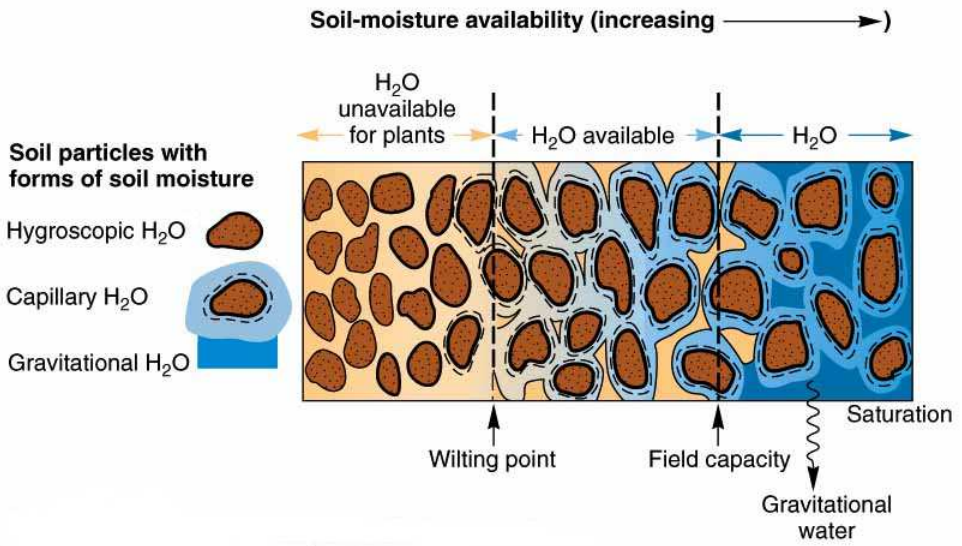

Figure 7.3: types of water present in soils in relation to soil moisture content.

Hygroscopic water is water absorbed from the atmosphere and held very tightly by the soil particles, so that it is unavailable to plants in amounts sufficient for them to survive Water occupies all pore spaces in the soil immediately following rainfall or irrigation. When rain or irrigation stops, water retained temporarily in the macropores is drained away by the pull of gravity. This excess water is called gravitational water. It moves through soil under the influence of gravity and that must be removed before the soil can attain field capacity. Moisture that is left in the soil is called capillary water. It is water that is left in the soil, along with hygroscopic moisture and water vapour, after the gravitational water has drained off. Capillary water is held by matric potential as a film of moisture on the surface of soil particles and peds, and as minute bodies of water filling part of the pore space between particles. Curved water surfaces or menisci form bridges across the pores at the boundaries between their water-filled and air-filled parts. Capillary water may move through the soil under the influence of surface tension forces.

Soil moisture content is defined, by convention, as the amount of water removed by drying at 105^oC. It is also called soil water content or soil wetness and it can be expressed in different ways, the most usual is to express it as a ratio in mass (w) or volume (θ).

The volume wetness or volumetric water content is generally computed as a percentage of the total soil volume or in units of volume of water per unit bulk volume of soil (m^3m^{-3}):

$$\theta = \frac{V_w}{V_t} \tag{7.7}$$

Thus, at saturation it is equal to the porosity. This way to express soil wetness is the most used in engineering and agricultural contexts.

The gravimetric soil moisture content is the ratio of mass of water (M_w) to that of solids (M_s):

$$w = \frac{M_w}{M_s} \tag{7.8}$$

Therefore, using Equations 7.2, 7.7 and 7.8, and density of water (ρ_w), we obtain an useful relationship between volumetric and gravimetric soil moisture content:

$$\theta = w \cdot \frac{\rho_b}{\rho_w} \tag{7.9}$$

For our purposes, soil water content will be expressed almost exclusively as volumetric ratio. It is often more convenient because it is more directly applicable to the computation of fluxes and water volumes added to soil by rain or irrigation and to quantities extracted from the soil by evaporation and transpiration.

It can range from extremely dry (or around 0 m^3m^{-3}) to the value of the porosity at full saturation. In sandy soils, θ at saturation is on the order of 40%; in medium-textured soils it is approximately 50%; and in clayey soils it can approach 60%. In the last, in fact, the volume of water at saturation can exceed the porosity of the dry soil, since clayey soils swell upon wetting.

Conveniently the quantity of soil water in a specific soil depth increment may be expressed in terms of soil water storage or equivalent depth of soil water (units of length). Equivalent depth of soil water, $D\theta$ (m), is calculated as:

$$D_\theta = \theta \cdot D \tag{7.10}$$

where D is the soil depth increment (m) having volumetric water content θ.

During a rain shower or irrigation application, the soil pores will fill with water. If all soil pores are filled with water the soil is said to be saturated. There is no air left in the soil. Thus, the degree of saturation (s) refers to a relative volume of pore space containing water in relation to the total porosity (Equation 7.3) and is also expressed as a ratio or percentage:

$$s = \frac{V_w}{V_p} = \frac{V_w}{V_w + V_a} = \frac{\theta}{p_t} \tag{7.11}$$

Plants need air and water in the soil. At saturation, no air is present and the plant will suffer. Many crops cannot withstand saturated soil conditions for a period of more than 2-5 days. The period of saturation of the topsoil usually does not last long. After the rain or the irrigation has stopped, part of the water present in the larger pores will move downward. This process is called drainage or percolation. The water drained from the pores is replaced by air. In coarse textured soils, drainage is completed within a period of a few hours, while in fine textured soils, drainage may take some days.

7.3 Water balance and evapotranspiration

The water balance is based on the law of conservation of mass, which states that matter can be neither created nor destroyed but can only change from one state or location to another. The flow processes in the soil are interdependent, the water balance is an account of quantities of water added, subtracted and stored within a given volume of soil during a specified period of time. The water balance is associated to the energy balance, an expression of the law of conservation of energy, both are involved in the same process: the content of water in the soil affects the way the flux of energy streaming into the soil-plant and the energy flux affects the state and movement of water. A description of the soil-plant interaction is based on an understanding of the evapotranspiration process that depends, in a combined way, on the simultaneous cycling of water and energy.

Using the law of conservation of mass, the total water in a system can be accounted for by taking into account various components of the hydrologic cycle involved.

In its simplest form, the water balance merely states that any change that occurs in the water content of a given body of soil during a specified period must equal the difference between the amount of water added to that body and the amount of water withdrawn from it during the same period.

The pertinent volume or depth of soil for which the water balance is computed is determined arbitrarily. Thus, in principle, a water balance can be computed for a small sample of soil or for an entire watershed. From an agricultural or plant ecological point of view, it is generally most appropriate to consider the water balance of the root zone (maximum depth at which the roots of a plant of interest can be found) per unit area of field. The root-zone water balance is usually expressed in integral form:

$$\Delta S + \Delta V = (P + I + U) - (R + D + E + T) \tag{7.12}$$

where ΔS is the change in root-zone soil-moisture storage, ΔV is the vegetational storage increment, P is precipitation, I is irrigation, U is upward capillary flow into the root zone, R is runoff and D is deep drainage leading to groundwater recharge. Note that the terms in these equation can be expressed as volumes or volumes per unit area during a specific time period, or as average rates.

In Equation 7.12 (water balance equation) the change in storage term can be either positive or negative, as water can be released from storage (negative) or absorbed into storage (positive). The other terms in the water balance equation can be recognized as a series of fluxes and stores. A flux is a rate of flow of some quantity: in the case of hydrology the quantity is water. The water balance equation assesses the relative flux of water to and from the surface with a storage term also incorporated. A large part of hydrology is involved in measuring or estimating the amount of water involved in this flux transfer and storage of water. The largest composite term in the “losses” part of Equation 7.12 is generally the evapotranspiration (E + T), as a flux includes that from open water bodies (lakes, ponds, rivers), the soil surface and vegetation (including both interception and transpiration from plants).

Precipitation (P) in the water balance equation represents the main input of water to a surface. It is a flux of both rainfall and snowfall. It is relatively easy to measure the amount of water added to the field by rain and irrigation (P + I), though areal nonuniformities must be taken into account.

The runoff (R) is in essence the movement of liquid water above and below the surface of the earth and it is (or at least should be) small in agricultural fields, particularly in irrigated fields, so it is often considered negligible in comparison with the major components of the water balance.

Capillary rise (U) is induced by extraction of water from the unsaturated zone and capillary fringe by evapotranspiration, and by migration of water to a freezing front. Capillary rise is usually considered to be a minor to negligible component of the water budget.

Another important, indeed essential, item of the field water balance is the internal drainage (D) out the bottom of the root zone. The function of drainage, in principle, is to release excess water that might otherwise restrict aeration and to leach excess salts. In the absence of adequate drainage (natural or artificial), waterlogging as well as salt accumulation in the root zone are particular hazards of arid-zone farming. Different components listed in Equation 7.12 are determined by lysimetric evaluation. A lysimeter is a confined volume of soil, in which input, output and change in water storage can be quantified. In a larger scale, water balance can be considered through a simpler equation as a continental water balance, only in terms of precipitation, runoff, change in storage and evapotranspiration:

$$P = \Delta S + R + ET \tag{7.13}$$

Evapotranspiration is the combination of two separate processes whereby water is lost on the one hand from the soil surface by evaporation and on the other hand from the crop by transpiration. Evaporation is the process whereby liquid water is converted to water vapour (vaporization) and removed from the evaporating surface (vapour removal). On the other hand, transpiration consists of the vaporization of liquid water contained in plant tissues and the vapour removal to the atmosphere.

Both of processes depend on the energy supply, vapour pressure gradient and wind; hence, radiation, air temperature, air humidity and wind terms should be considered when assessing ET. The most used units to express evaporation rate are millimetres per unit time, normally mm/day. That is the amount of water lost from a cropped surface in units of water depth. It can be expressed as a volume per unit area or energy per unit area as well. In Table 7.3 a units conversion guide is summed up.

Evaporation and transpiration occur simultaneously and there is no easy way of distinguishing between the two processes. Evaporation from a cropped soil is mainly determined by the fraction of the solar radiation reaching the soil surface and when the crop is small, water is predominately lost by soil evaporation. Once the crop is well developed and completely covers the soil, transpiration becomes the main process.

Table 7.3: conversion factors for different ET units. From [124]. (For water with density of 1000 kg/m^3 and temperature of 20^{o}C)

	Depth	**Volume per unit area**		**Energy per unit area**
	$mm\ day^{-1}$	$m^3\ ha^{-1} day^{-1}$	$l\ s^{-1} ha^{-1}$	$MJ\ m^{-2} day^{-1}$
1 $mm\ day^{-1}$	1	10	0.116	2.45
1 $m^3\ ha^{-1} day^{-1}$	0.1	1	0.012	0.0245
1 $ls^{-1}\ ha^{-1}$	8.640	86.40	1	21.17
1 $MJm^{-2}\ day^{-1}$	0.408	4.082	0.047	1

The amount of water required to compensate the ET loss from the cropped field is defined as crop water requirement. Weather parameters (such as radiation, air temperature, wind speed and humidity), crop characteristics, management and environmental aspects are factors affecting evaporation and transpiration.

Direct measurement of evapotranspiration is much more difficult and expensive than of precipitation and streamflow, and is usually impractical. Thus hydrologists have developed an array of methods that provide estimates of evapotranspiration based on measurements of more readily measured quantities. Owing to the difficulty of obtaining accurate field measurements, ET is commonly computed from weather data. A large number of empirical or semi-empirical equations have been developed for assessing crop or reference crop evapotranspiration from meteorological data. Some of the methods are only valid under specific climatic and agronomic conditions and cannot be applied under conditions different from those under which they were originally developed.

The evapotranspiration rate from a reference surface, not short of water, is called the reference crop evapotranspiration or reference evapotranspiration and is denoted as ET_0. The reference surface is a hypothetical grass reference crop with specific characteristics. These characteristics are: crop height of 0.12 m, fixed surface resistance of 70 s m^{-1} and albedo of 0.23. The reference surface closely resembles an extensive surface of green, well-watered grass of uniform height, actively growing and completely shading the ground. The most used method in ET_0 calculations is the FAO Penman-Monteith equation ([124], Equation 7.14).

The FAO Penman-Monteith method is selected as the method by which the evapotranspiration of this reference surface (ET_0) can be unambiguously determined, and as the method which provides consistent ET_0 values in all regions and climates. The FAO Penman-Monteith equation is derived from original Penman-Monteith equation and estimation of other parameters (aerodynamic and surface resistance):

$$ET_0 = \frac{0.408\Delta(R_n - G) + \gamma\frac{37}{T_{hr}+273}u_2(e^o(T_{hr}) - e_a)}{\Delta + \gamma(1 + 0.34u_2)} \tag{7.14}$$

Where ET_0, expressed in in mm $hour^{-1}$, is the reference evapotranspiration and the remaining parameters are explained in Table 7.4. Therefore, in order to calculate the hourly reference evapotranspiration rate some direct measurements are required, whereas other parameters must be worked out by means of empirical data and calculations.

- Wind speed

Table 7.4: parameters on FAO Penman-Monteith equation (Equation 7.14 7.14)

Symbol	**Definition**	**Units**	**Determination**
u_2	Average hourly wind speed at 2 m height	m s^{-1}	Direct measurement
T_{hr}	Mean hourly air temperature at 2 m height	$°C$	Direct measurement
e_s	Saturation vapour pressure	kPa	Equation 7.18
e_a	Average hourly actual vapour pressure	kPa	Equation 7.19
Δ	Slope vapour pressure curve	kPa $°C^{-1}$	Equation 7.26
γ	Psychrometric constant	kPa $°C^{-1}$	Equation 7.21
R_n	Radiation at the crop surface	MJ m^{-2} $hour^{-1}$	Equation 7.22
G	Soil heat flux density	MJ m^{-2} $hour^{-1}$	Equation 7.30

As wind speed at a given location varies with time, it is necessary to express it as an average over a given time interval. In case wind speed measurements are not able to be done at 2 m above ground surface, the following expression can be used:

$$u_2 = u_z \frac{4.87}{ln(67.8z - 5.42)} \tag{7.15}$$

Where u_z is the measured wind speed at z m above ground surface.

- Temperature

  Firstly, the air temperature (T_{hr}) corresponds to the average between the maximum (T_{max}) and minimum (T_{min}) hourly temperatures:

$$T_{hr} = \frac{T_{max} - T_{min}}{2} \tag{7.16}$$

  Due to the non-linear relationship between air temperature and air humidity, T will be calculate according to Equation 7.16 rather than through other methods as the average of hourly temperature measurements. In fact, T data are employed to compute parameters related to vapour pressure.

- Vapour pressure

  Saturation vapour pressure is the pressure at which water vapour is in thermodynamic equilibrium with its condensed state. The temperature dependence of saturation vapour pressure can be calculated through the relationship:

$$e^o(T) = 0.6108 \cdot exp\left[\frac{17.27 \cdot T}{T + 237.3}\right] \tag{7.17}$$

  In turn, dewpoint temperature (T_d), or simply dewpoint, is the temperature to which the air needs to be cooled to make the air saturated. The actual vapour pressure (e_a) of the air is the saturation vapour pressure at the dewpoint temperature. The drier the air, the larger the difference between the air temperature and dewpoint temperature. The corresponding daily values used in Equation 7.14 are computed trough the following relationships. Saturation vapour pressure (e_s):

$$e_s = \frac{e^o(T_{max}) - e^o(T_{min})}{2} \tag{7.18}$$

Actual vapour pressure:

$$e_a = e^o(T_d) = 0.6108 \cdot exp\left[\frac{17.27 \cdot T_d}{T_d + 237.3}\right] \tag{7.19}$$

Where T_d is the average dewpoint and it should be calculated like T in Equation 7.16. There are other ways to estimate ea in case T_d is unknown. And the slope of the relationship between saturation vapour pressure and T, denoted by Δ:

$$\Delta = \frac{4098 \cdot \left[0.6108 \cdot exp\left(\frac{17.27 \cdot T}{T+237.3}\right)\right]}{(T + 237.3)^2} \tag{7.20}$$

- Psychrometric constant

  The psychrometric constant (γ) is given by:

  $$\gamma = \frac{c_p p}{\varepsilon\lambda} = 0.665 \cdot 10^{-3} \tag{7.21}$$

  where c_p is the specific heat at constant pressure (for average atmospheric conditions is usually assumed $c_p = 1.013 \cdot 10^{-3} MJ\ kg^{-1}\ °C^{-1}$), ε is the ratio between molecular weight of water vapour and dry air ($\varepsilon = 0.622$), λ is the latent heat of vaporization of water at 20 $°C$ ($\lambda = 2.45$ MJ kg^{-1}) and p is the atmospheric pressure in kPa (taken by direct measurement).

- Net radiation

  The net radiation (R_n) is the difference between the incoming net shortwave (R_{ns}, Equation 7.23) and the net outgoing longwave (R_{nl}, Equation 7.29) radiation:

  $$R_n = R_{ns} - R_{nl} \tag{7.22}$$

  R_n is normally positive during the daytime and negative during the nightime. The total daily value for R_n is almost always positive over a period of 24 hours, except in extreme conditions at high latitudes. R_{ns} is the resulting from the balance between incoming and reflected solar radiation is given by:

$$R_{ns} = (1 - \alpha)R_s \tag{7.23}$$

where α is the albedo (which is 0.23 for the hypothetical grass reference crop) and R_s is the incoming daily solar radiation which is usually measured by a pyranometer. The first step to obtain R_{nl} is to estimate the extraterrestrial radiation R_a for hourly periods (as usual expressed in $MJm^{-2}hour^{-1}$).

It can be done with the following expression:

$$R_{ns} = \left(\frac{60}{\pi}\right)G_{sc}d_r\left[\omega_s sin(\varphi)sin(\delta) + cos(\varphi)cos(\delta)sin(\omega_s)\right] \tag{7.24}$$

where G_{sc} is the solar constant ($G_{sc} = 0.0820\ MJ\ m^{-2}min^{-1}$, d_r is the inverse relative distance Earth-Sun (Equation 7.25),ω_s is the sunset hour angle (in rad, Equation 7.26), φ is the latitude (in rad) and δ is the solar declination (in rad, Equation 7.27). The needed factors in Equation 7.24 are given by:

$$d_r = 1 + 0.033cos\left(\frac{2\pi}{365}DOY\right) \tag{7.25}$$

$$\delta = 0.409sen\left(\frac{2\pi}{365}DOY - 1.39\right) \tag{7.26}$$

$$\delta = arccos\left[-tan(\varphi)tan(\delta)\right] \tag{7.27}$$

DOY (day of year) is the the number of the day in the year between 1 (1 January) and 365 or 366 (31 December).

Once R_a is known, the last factor that is required to calculate R_{nl} is the clear-sky solar radiation (R_{so}), which as a function of station elevation above the sea level (z, in meters) is given by:

$$R_{so} = (0.75 + 2 \cdot 10^{-5}z)R_a \tag{7.28}$$

So, finally, R_{nl}:

$$R_{nl} = \sigma \underbrace{\left(\frac{T^4_{max,K} + T^4_{min,K}}{2}\right)}_{\text{Stefan-Boltzman Law}} \underbrace{\left(0.34 - 0.14\sqrt{e_a}\right)}_{\text{effects of air humidity}} \underbrace{\left(1.35\frac{R_s}{R_{so}} - 0.35\right)}_{\text{effects of cloudiness}} \quad (7.29)$$

- Soil heat flux

  There are several models that try to describe soil heat flux (G), for a calculation time compressed between time i–1 and time i, the following expression can be used:

  $$G = C_s \frac{T_i + T_{i-1}}{\Delta t} \Delta z \quad (7.30)$$

  Where T_i and T_{i-1} are the temperatures ($°C$) at times i and i–1, c_s is the soil heat capacity (assumed $c_s = 2.1 MJm^{-3}\ °C^{-1}$), Δt is the length of time interval (hour) and Δz is the effective soil depth. The depth of penetration of the temperature wave is determined by the length of the time interval, i.e., Δz is only a few centimetres for a time interval of one or a few days (and so $G_{day} \approx 0$) but might more than 2 m for monthly periods. Where the soil is warming, the soil heat flux G is positive. The amount of energy required for this process is subtracted from R_n when estimating evapotranspiration.

In this study the evapotranspiration is estimated with hourly FAO Penman-Monteith equation using input data of MeteoSense® station 8.1, a typical daily trend is shown in Figure 7.4. As an exercise the results were compared with those obtained from the following software: REF-ET (Reference evapotranspiration calculation) and Hourly Reference Evapotranspiration (ET_0) (HRPM) Calculator, both software use hourly weather data and the FAO Penman-Monteith equation. Linear regressions show a excellent correlation between the estimation of ET_0 with hourly FAO Penman-Monteith and that obtained with REF-ET and HRPM (Figure 7.5).

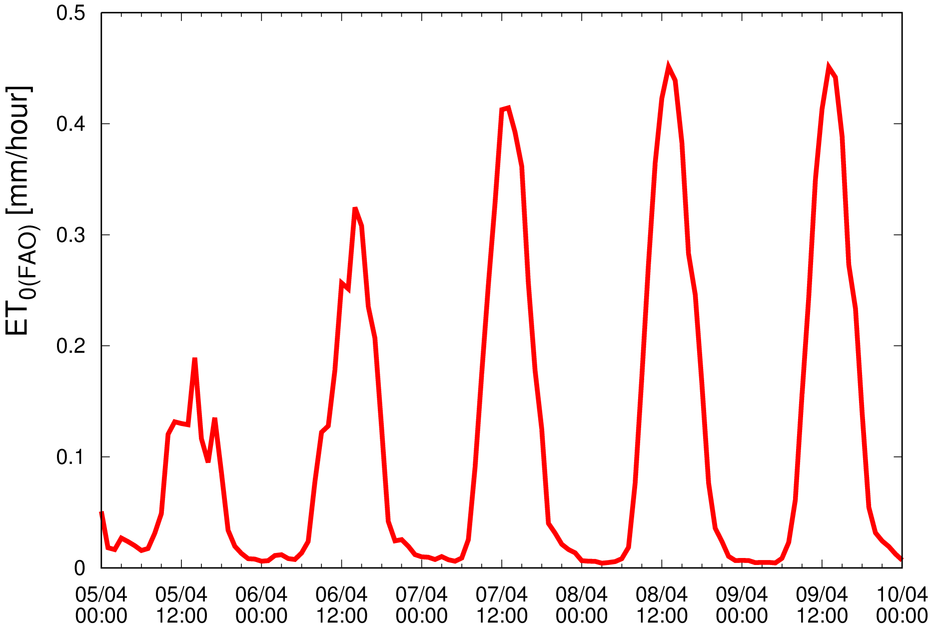

Figure 7.4: graphic representation of evapotraspiration estimate using input data of MeteoSense® station (see Section 8.1) from 05/04/2017 to 10/04/2017.

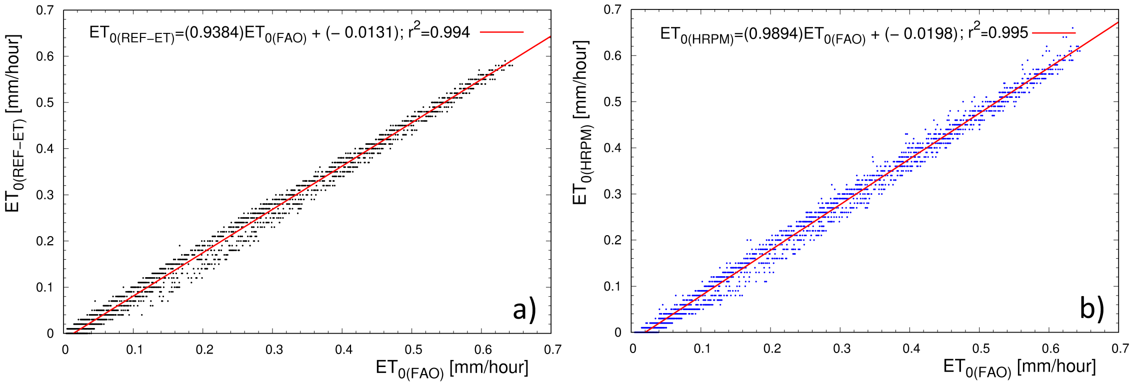

Figure 7.5: a) linear regression between ET_0 estimate with FAO Penman-Monteith equation ($ET_{0(FAO)}$) and REF-ET software $ET_{0(REF-ET)}$ b) linear regression between ET_0 estimate with FAO Penman-Monteith equation ($ET_{0(FAO)}$) and HRPM software ($ET_{0(HRPM)}$).

Chapter 8

Equipment and field test

Overview

Soil water content is an important property in plants biophysical processes, the quantification of soil moisture is necessary in agriculture for the optimization of irrigation.

Terrestrial gamma radiation attenuation can be used to measure the change in soil moisture near the surface with a greater sensitivity for the upper 20 cm [125].

Water is an effective absorber of gamma radiation emitted from the radionuclide in the soil (^{40}K, ^{214}Bi and ^{208}Tl), the incremented moisture has the adverse effect of decreasing the signal intensity because there are more water molecules to attenuate the gamma-ray flux [126].

Soil water content measurement with gamma spectroscopy techniques can be made by in situ [127] and airborne survey [128], this method can be used to scan a large field rapidly after an opportune calibration with gravimetric measurements [125]. Recently this type of proximal remote sensing technique has been combined with microwave, infrared and thermal spectroscopy for studing the vertical distribution of the soil water content in the root zone for agricultural purposes [129].

With the aim of measuring the water content in the first 20 cm of soil of an area of 0.2 ha a gamma station equipped with a sodium iodide gamma-ray detector were placed in a tomatoes crop field located in Budrio (BO).

The volume of water-filled pore space changes as a function of precipitation or irrigation events and subsequent soil drying via deep percolation and evapotranspiration (See Section 7.12), for this reason solar radiation, temperature, rain and other environmental factors were studied with the aid of a professional agrometerorological station installed near the gamma station.

8.1 Agrometeorological station

The MeteoSense® professional agrometeorological station (Figure 8.1) (Meteosense 2.0; Netsens s.r.l., Florence, Italy;), includes different instruments to carry out estimations of the various meteorological magnitudes (see Table 8.1)

Table 8.1: main sensors and technical specifications of agrometeorological station Meteosense 2.0 [130]

Meteosense 2.0 agrometeorological station				
Weather sensors	**Measured quantity**	**Operative range**	**Resolution**	**Accuracy**
Anemometer	m/s	Speed: 0 - 75 m/s Direction: 0° - 360°	Speed: 0.1 m/s Direction: 0.5°	Speed: ± 0.12 % Direction: ± 4 %
Rain gauge	mm/h	/	0.2 mm/h	/
Air temperature	°C	-40 °C - +80°C	0.1°C	± 0.4 °C.
Air Humidity	RH	0 - 100 % RH	0.1 % RH	± 3 %
Dew point/frost	°C	-40°C +25°C	0.1°C,	± 0.5°C.
Barometer	hPa	750 - 1050 hPa	0.1 hPa	0.2 hPa
Solar Pyranometer	W/m^2	0 - 1800 W/m^2	1 W/m^2	± 5 %
UV Radiation	MED = 0.06 Wh/m^2	0 - 199 MEDs	/	± 5%
Battery and photovoltaic (solar) panel				
Battery type: Pb, rechargeable Nominal voltage: 12 Vdc Minimum battery capacity: 12 Ah Maximum battery capacity: 100 Ah Maximum current: 3A Max recharge current from solar panel: 2A				

Meteosense main unit implements a large memory area used to save data if communication with Central Server is temporary unavailable. All data are internally stored (associated to sampling time/date), and then automatically retransmitted to Central Server once communication is again available. Optionally, data can be stored on SD-Card memory card; in this case SD-Card can be removed and read using external devices.

Figure 8.1: Meteosense station performing measurements in the testing ground.

8.2 Gamma Station

The gamma spectroscopy station is equipped with a 1L sodium iodide scintillator NaI (Tl) connected to the CAEN Gamma Stream multichannel analyzer (see Chapter II) which acquires the signals in list mode (event by event) and in histogram format *.spe on an SD card. The system is powered by a photovoltaic kit (100 W panel connected to a battery from 100 Ah). The instrument is placed inside a steel box (Figure 8.2), held by a 2.3 m high pole, at this height the horizontal field of view of the detector is $\sim$ 25 m radius (see Figure 8.3).

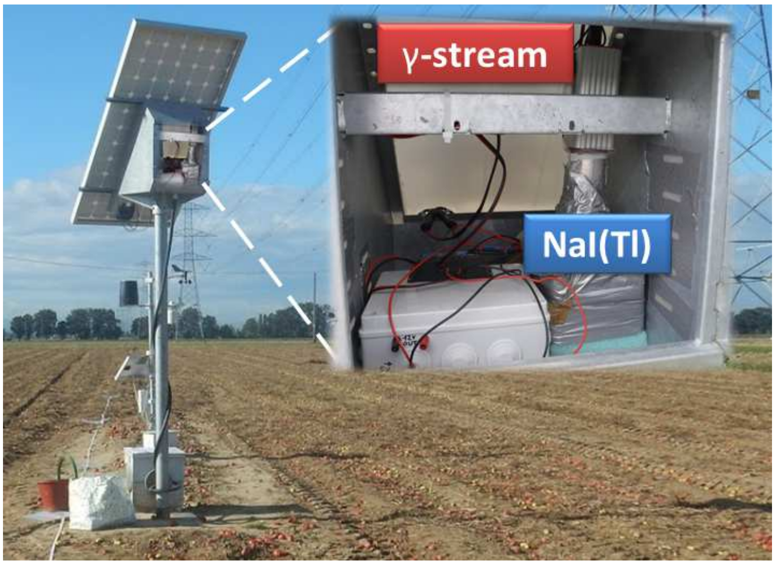

Figure 8.2: the gamma spectroscopy station (left) and the inside of the steel box containing instruments for gamma spectroscopy: NaI(Tl) and CAEN Gamma Stream (right)

Figure 8.3: representation of the field of vision of NaI(Tl) installed in the Gammma Station at 2.3 m height. In yellow is highlighted the region that produces the greatest contribution in the gamma signal. The percentage of source radiation detected reaches 95% at $\sim$ 25 m (see Section 9.1)

.

8.3 Testing field

The testing ground consists in a nearly rectangular crop filed whose dimensions are 108 x 40 m and it is NE - SW oriented. Agrometeorological station and the gamma spectroscopy station are placed in tomatoes crop field at Acquacampus irrigated research area of CER (Canale Emiliano Romagnolo) located in Budrio in the province of Bologna.

Instruments within the testing ground are arranged in the following way: the gamma station placed at around 34 m from NE side and 14 m from ES side, the agrometeorological station is placed at around 4 m from the gamma station (Figure 8.1).

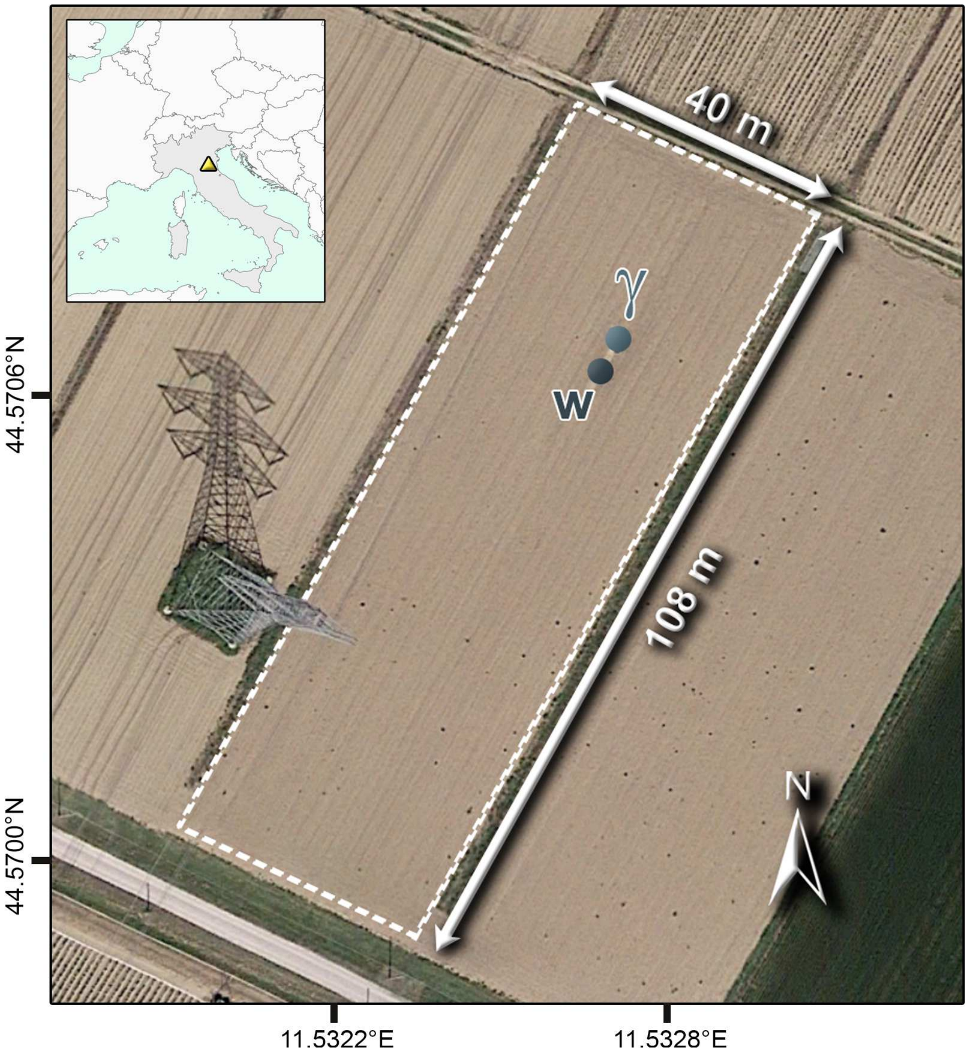

Figure 8.4: geographical location of testing field and relative position of meteo station and gamma station. Screenshot from Google Earth.

The crop is watered with sprinklers, a method of providing rainfall-like irrigation to the crops (see Figure 8.5 and Table 8.3). A field Diary allowed the to keep records of a complete history of the field, the main activities are presented in Table 8.2.

Table 8.2: the main field activities.

Data	**Activity**
18/05/2017	Field fertilization
23/05/2017	Tomates implantation
14/09/2017	Harvesting tomatoes

Figure 8.5: particular of an impact irrigation sprinkler and a tomato fruits in the crop field.

Table 8.3: table of irrigation.

Date	Time	Total time [hh:mm]	Irrigation [mm]
24/05/2017	08:42:00 09:42:00	1:00	7.5
26/05/2017	15:15:00 17:15:00	2:00	15
30/05/2017	13:15:00 15:15:00	2:00	30
01/06/2017	11:15:00 13:15:00	2:00	15
06/06/2017	13:45:00 15:45:00	2:00	15
13/06/2017	08:22:00 10:30:00	2:08	15
19/06/2017	14:40:00 17:00:00	2:20	15
22/06/2017	14:08:00 15:28:00	1:20	20
26/06/2017	08:20:00 11:40:00	3:20	25
05/07/2017	08:37:00 10:37:00	2:00	30
11/07/2017	07:48:00 11:48:00	4:00	30
18/07/2017	08:15:00 10:41:00	2:26	30
25/07/2017	09:12:00 13:12:00	4:00	30
01/08/2017	08:33:00 13:33:00	4:40	35
07/08/2017	08:40:00 11:00:00	2:20	17.5
18/08/2017	13:20:00 16:00:00	2:40	15

The tomatoes plant row density (RD) is 5.2 plants/m and the row spacing (RS) 1.5 m, the areal standard density (ASD) is given by: ASD = RD/RS $\simeq$ 3.5 plants/m^2.

Destructive above-ground biomass samples were collected in 4 different evolution step of tomatoes plant to estimate the amount of water in the plant defined Plant Water Mass expressed in kg/m^2 (numerically equal to the water height in mm) (see Figure 8.6). The plant were separated into stem, leaf and fruits components, the last measure was made at the maximum fruit development (full harvest).

Table 8.4: water content of tomato plants biomass samples.

Sampling day	$\theta_{leaf,stem}$ $[mm]$	θ_{fruits} $[mm]$	$PWM = \theta_{leaf,stem} + \theta_{fruits}$ $[mm]$
23/05/2017	0.05	0.00	0.05
23/06/2017	0.70±0.11	0.04±0.02	0.74±0.14
24/07/2017	1.57±0.11	4.16±0.12	5.73±0.23
28/08/2017	1.42±0.04	7.06±1.06	8.47±1.10

Figure 8.6: tomatoes plants harvested for destructive biomass analysis.

8.3.1 Physical properties of soil

The in situ surveys curried out on the testing ground reveals some important information regarding soil texture, soil bulk density and other physical properties for the aims of this study. These results are listed in Table 8.5. The survey has been made by Agri-Bio-Eco Laboratori Riuniti s.r.l. within two depth ranges: 0-30 cm and 30-60 cm. In both of depths the same soil texture with quite similar clay, silt and sand contents are found. The experimental layout was set up on 13 March 2017, and at the same time some soil samples were collected in order to characterize the soil bulk density (ρ_b). According to the percentage of sand silt and clay (see Table 8.5) using the three-phase system [121] is classifiable as sandy loam (see Figure 8.7).

Table 8.5: soil survey made up by Agri-Bio-Eco Laboratori Riuniti s.r.l

Depth (cm)		0-30	30-60
Soil class content (%)	**Sand**	65	66
	Silt	19	18
	Clay	16	16
Soil texture		**Sandy loam**	**Sandy loam**
Organic matter content (%)		1.26	1.13
Electrical conductance (dS)		0.185	0.23
pH		7.9	7.8

Table 8.6: results of measurements carried out on samples collected on 13/03/2017.

Depth [cm]	0-30
Volume $[m^3]$	$0.708 \cdot 10^{-3}$
$M_{sample} = M_s + M_w [kg]$	0.45914
Ms [kg]	0.39021
ρ_b [kg m^{-3}]	1345

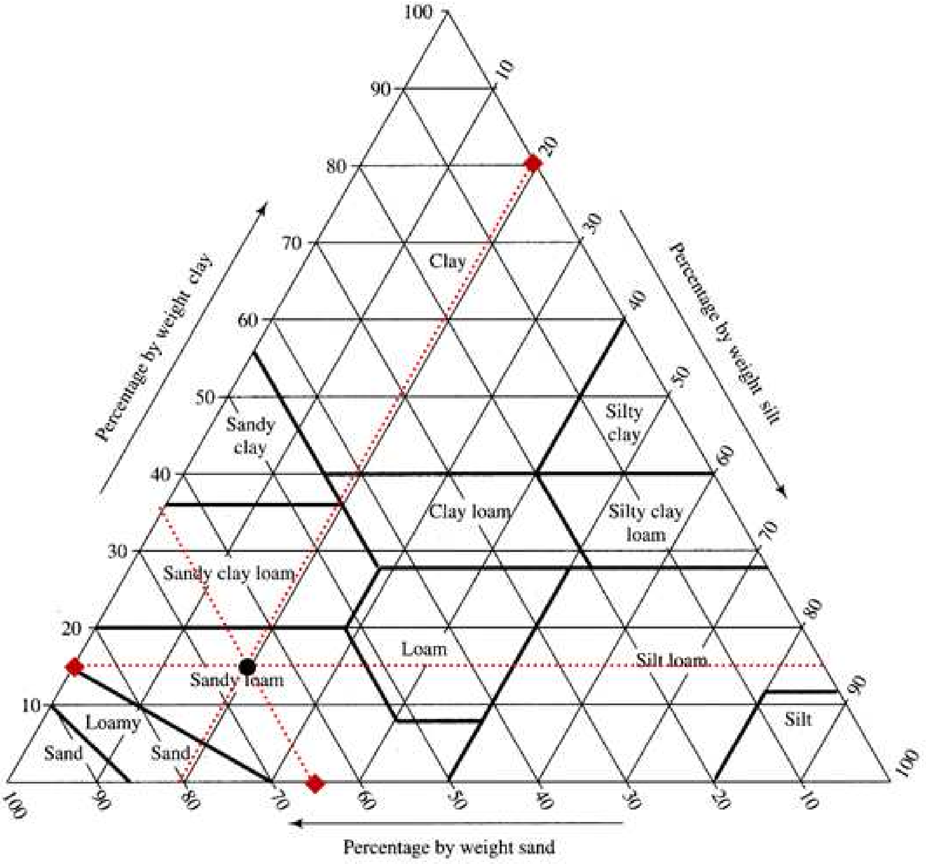

Figure 8.7: schematic view of soil as three-phase system devised by USDA (from [121]). According to the Table 8.5 the soil is a mixture of about 16% of clay, 65% of sand and 19% of silt (percentages indicated by red squares) and is classifiable as sandy loam.

To calibrate and compare the water content measurements estimated with the gamma spectroscopy method, a large number of soil samples were collected following the sampling scheme show in Figure 8.8 in different soil moisture conditions at different depths (0-10 cm, 10-20 cm, 20-30 cm) (see Table 8.7) and their water content was calculated through the gravimetric method. This traditional method of measuring w consists of removing a sample by augering into the soil and then determining its moist and dry weights (M_s^{wet} and M_s^{dry} respectively). The moist weight is determined by weighing the sample as it is at the time of sampling; the dry weight is obtained after drying the sample to a constant weight in an oven. Indeed:

$$M_w = M_s^{wet} - M^{dry} \tag{8.1}$$

And using Equation 7.7, volumetric water content (θ) can be obtained.

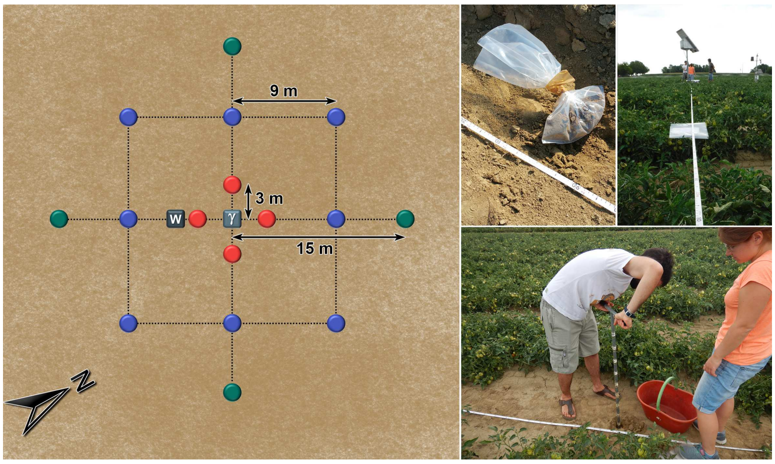

Figure 8.8: sampling scheme of the 16 samples collected for gravimetric and gamma measurements.

Table 8.7: mean and standard deviation of volumetric water content obtained from gravimetric measurements performed in Budrio (see Appendix 9.3).

Date	θ_G $[m^3/m^3]$ [%]			
	0-10 cm	**10-20 cm**	**20-30 cm**	**Number of samples**
24/07/2017	16 ± 3	18 ± 2	22 ± 3	48
26/07/2017	27 ± 3	24 ± 3	24 ± 3	48
28/07/2017	18 ± 3	21 ± 2	23 ± 3	48
18/09/2017	22 ± 1		/	16
21/09/2017	24 ± 2		/	16

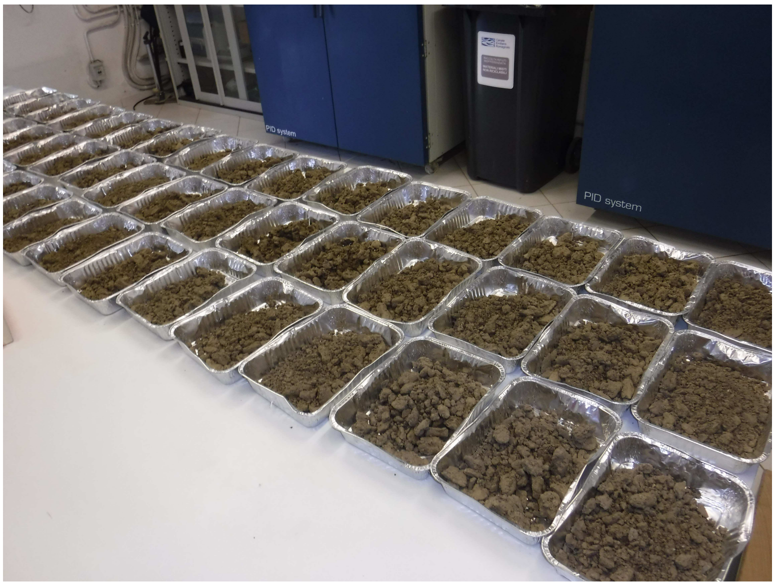

Figure 8.9: soil samples before oven drying.

8.3.2 Chemical properties of soil

On 18 September 2017, 5 samples were collected in positions with ID 36 37 38 39 40 (see Figure 8.8). X-ray fluorescence was used to identify the the major elements of oxides in the soil (see Table 8.8).

Table 8.8: mean and standard deviation of the percentage in mass of major elements and LOI (Loss On Ignition: H_20, CO_2, organic, etc.) in soil resulting from 5 measurements carried out on samples collected on 18/09/2017 (see Table 13), measurements made by ANALITICA S.a.s.

Major Elements of oxides	**Mass fraction [%]**
Na_2O	0.958 ± 0.031
MgO	2.844 ± 0.038
Al_2O_3	11.734 ± 0.050
SiO_2	55.720 ± 0.552
P_2O_5	0.272 ± 0.033
K_2O	2.080 ± 0.039
CaO	9.618 ± 0.081
TiO_2	0.510 ± 0.014
MnO	0.118 ± 0.004
Fe_2O_3	4.348 ± 0.116
LOI	11.804 ± 0.542

To estimate the abundance of radionuclides present in the soil and their spatial homogeneity, 16 samples were collected at a growing distance from the gamma station (3, 9, 15 m) see Figure 8.8 and 3 additional samples were collected at a distance of $\sim$ 20 m. The samples were measured using the high purity germanium detector HPGe called MCA Rad (see Section 5.3 [87]). The low values of the standard deviation show that the radionuclide distribution is homogeneous (see Table 8.9).

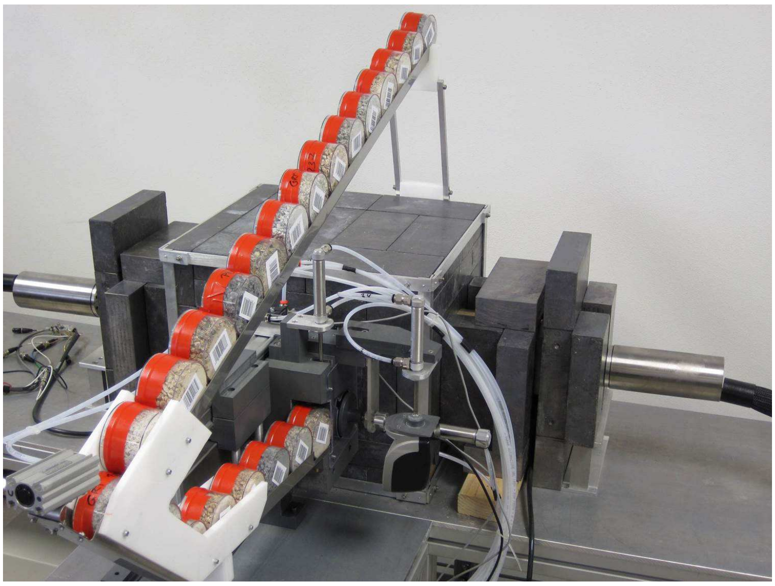

Figure 8.10: the High Pure Germanium detector (HPGe) called MCA Rad composed by two coaxial p-type HPGe detectors used for the analysis

Table 8.9: mean and standard deviation of natural radionuclide abundances and activity for the 19 samples taken 30/03/2017 (see Table 7 analysed with HPGe).

Mass[g]	204.47 ± 13.56
Activity ^{40}K [Bq/kg]	504.21 ± 50.22
Abundance ^{40}K [%]	1.61 ± 0.16
Activity ^{214}Bi [Bq/kg]	30.96 ± 3.07
Abundance eU [ppm]	2.51 ± 0.25
Activity ^{208}Tl [Bq/kg]	38.45 ± 4.40
Abundance eTh[ppm]	9.47 ± 1.08

Chapter 9

Preliminary results and discussions

9.1 Fundamentals

The correct interpretation of the data acquired with the gamma and agrometeorological station requires an understanding of the physical principle, the system calibration, the analysis method and data reduction processing procedure. The gamma radiation flux near the ground originates primarily from the natural radioisotopes in the soil in the typically range of 0.3-3 Mev. The energies of these photons are reduced by the interaction with matter, the attenuation depends on the source-detector geometry and on the crossed medium between the source and the detector. The Subsections 9.1.1 and 9.1.2 quantifies the influence of this phenomenon on the detector's field of view and in the presence of soil moisture. The Subsection 9.1.3 explain how the Monte Carlo simulation strategy has been investigated in physical conditions for which an exact analytical solution wasn't known. The Subsection 9.1.4 presented two main software for hydrological simulation used to estimate the water content in the soil: Aquacrop and Criteria. These software need as a input meteorological data provided by the agrometeorological station, the soil characteristics and crop field specification.

9.1.1 Horizontal and vertical field of view

The flux of unscattered photons emitted by the naural radionuclides that are present in dry soil is given by the following Eq. [131]:

$$\Phi = \frac{A_t}{2\mu_s} \int_0^1 dcos\theta \left[1 - e^{\frac{-\mu_s z}{cos\theta}} \right] \tag{9.1}$$

where A_t is the volumetric gamma activity [γ/cm^3] of the uniformly distributed U, Th and K radionuclide, μ_s [cm^2g^{-1}] is the soil linear attenuation coefficient referred to the energy photons, z [cm] is the thickness of the soil layer in which gamma photons are homogeneously and isotropically emitted.

According to Eq. 9.1 the percentage of the infinite source radiation detected from thick circular source of varying radius for ^{40}K, ^{214}Bi and ^{208}Tl gamma rays (see Table 2.6 and 2.5) and detector height of 2.3 m reaches 95% at $\sim$ 25 m of radius (Figure 8.3). Using Eq. 9.1 it is also possible to estimate that the first 20 cm, 30 cm, 40 cm of the dry soil (with a density and chemical composition of Budrio testing field exposed in Section 8.3.1) contributes respectively to ~92%, ~97%, ~99% of the radiation (at the emission energies of ^{40}K) at the surface of the soil (see Figure 9.2).

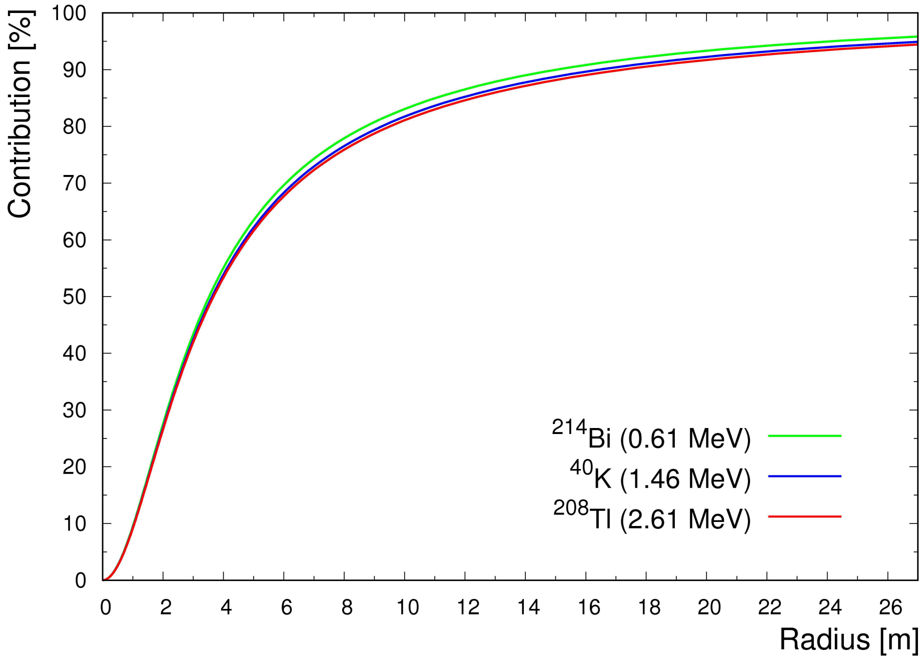

Figure 9.1: variation in response of a spherical detector 2.3 m height to circular source of different diameter for ^{40}K, ^{214}Bi and ^{208}Tl gamma rays.

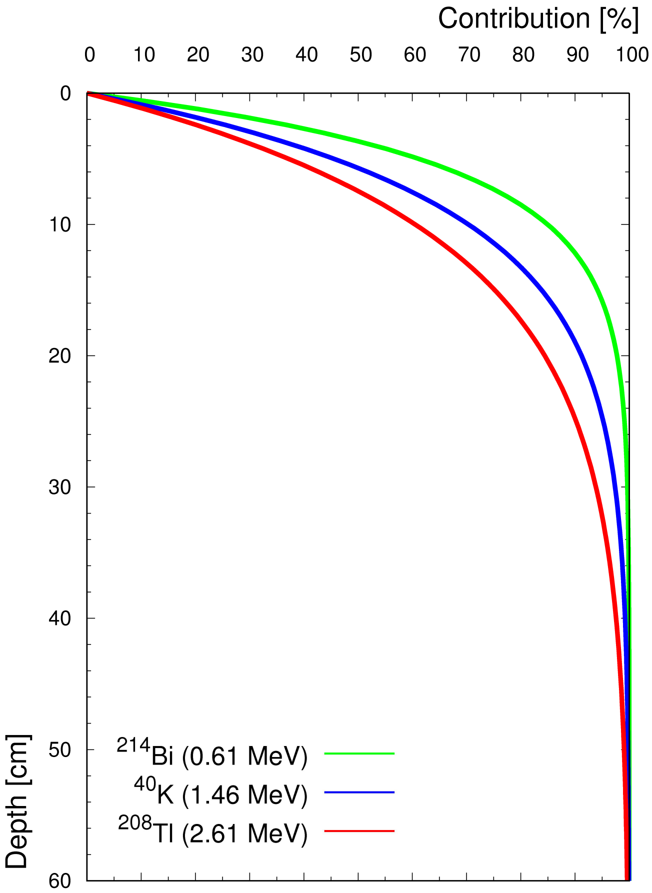

Figure 9.2: percentage of the infinite source radiation detected from broad source of varying thickness for ^{40}K, ^{214}Bi and ^{208}Tl gamma rays and a dry soil source density of $1.345 g/cm^3$

9.1.2 Soil moisture attenuation

The water in the soil pores produces an effective change in soil density, causing a variation of the gamma flux. Water is 1.11 times more effective in attenuating gamma radiation than a typical dry material [126]. The relationship between the linear attenuation coefficient of a wet soil (μ_w) and a dry soil (μ_s) is given by $\mu_w = \mu_s(1 + 1.11w)$. The Eq. 9.1 for a wet soil becomes:

$$\Phi = \frac{A_t}{2\mu_s(1+1.11w)} \int_0^1 dcos\theta \left[1 - e^{\displaystyle\frac{-\mu_s(1+1.11w)z}{cos\theta}} \right] \tag{9.2}$$

where w is the gravimetric water content in the soil [kg kg^{-1}] (see Eq. 7.8).

The ratio between the flux measured produced from the soil with gravimetric water content equal to w and the gravimetric water content equal to w_0 is given by:

$$\frac{\Phi(w)}{\Phi(w_0)} = \frac{(1+1.11w_0)}{(1+1.11w)} \tag{9.3}$$

from this equation it is possible to obtain w:

$$w = \frac{\frac{\Phi(w)}{\Phi(w_0)}(1+1.11w_0) - 1}{1.11} \tag{9.4}$$

Given a gravimetric calibration measurement of water content w_0, according to [125] three independent soil moisture values can be calculated using the counts rate from the ^{40}K and ^{208}Tl window (see Table 2.6) and gross count window (GC) (0.3-3 MeV) by the following equations:

$$w(^{40}K)[\%] = \frac{\frac{K_{\theta_0}}{K_\theta}(100+1.11w_0) - 100)}{1.11} \tag{9.5}$$

$$w(^{208}Tl)[\%] = \frac{\frac{T_{\theta_0}}{T_\theta}(100+1.11w_0) - 100)}{1.11} \tag{9.6}$$

$$w(GC)[\%] = \frac{\frac{GC_{\theta_0}}{GC_\theta}(100+1.11w_0) - 100)}{1.11} \tag{9.7}$$

where:

- K_θ, T_θ, and GC_θ current soil gamma count rates in windows ^{40}K, ^{208}Tl, and GC
- K_{θ_0}, T_{θ_0} and GC_{θ_0} calibration soil gamma count rates in windows ^{40}K, ^{208}Tl, and GC
- $w[\%]$ and $w_0[\%]$ current and calibration soil moisture for the upper 20 cm.

In this study the ^{40}K window was chosen, the reason is related to the fact that the photopeak has a high number of events ($\sim 3.6 \cdot 10^4$ counts per hour) with a mean associated statistical noise of $\sim 0.5\%$ (see Section 9.2.2). To get the contents of volumetric water is necessary multiply the gravimetric water content $w(^{40}K)[\%]$ to the soil bulk density ρ_b using Eq. 7.9:

$$\theta_K = \theta(t)[\%][m^3m^{-3}] = \rho_b \left[\frac{\frac{K_{\theta_0}}{K_\theta}(100 + 1.11w_0) - 100)}{1.11} \right] \tag{9.8}$$

the equation can be written replacing the following term:

$$\xi = \rho_b \frac{100}{1.11} \tag{9.9}$$

$$\theta_0 = \rho_b w_0 \tag{9.10}$$

the vegetative cover generates a shielding effect producing an overestimation of water content. The count rate attenuation produced by the plants water mass (PMW) is given from the following fraction:

$$\Lambda(PWM) = \frac{K_\theta(PWM)}{K_\theta} \tag{9.11}$$

where K_θ is the measured counts rate in windows ${}^{40}K$ in bare soil conditions, and $K_\theta(PWM)$ is the count rate in the presence of the vegetative cover: $PWM[mm] = \theta_{steam,leaf} + \theta_{fruits}$. $\theta_{leaf,stem}$ is a time-dependent factor related to Leaf Area Index (LAI) [132] that characterizes plant canopies defined as the one-sided green leaf area per unit ground surface area (m^2m^{-2}) and θ_{fruits} depends to fruits growth rate after anthesis [133].

After the appropriate substitutions the Eq. 9.8 becomes:

$$\theta_K = \Lambda(PWM)\frac{K_{\theta_0}}{K_\theta(PWM)}(\xi + \theta_0) - \xi \tag{9.12}$$

9.1.3 Monte Carlo simulation

Monte Carlo simulations is a powerful tool in modelling the performances of systems too complex for analytical solutions. A simulation attempts to generate a sample of representative scenarios for a model in which a complete enumeration of all possible states would be prohibitive or impossible.

In this context, Monte Carlo methods relies in the possibility of simulating the behaviour of each single photon, by simulating both the emission and propagation of photons one-by-one. Monte Carlo simulations generate the random distances each photon travels before undergoing interactions in a specific medium, testing the interaction most likely to occur and determining full or partial energy deposition.

In order to simulate gamma-ray spectra measured by the gamma station a Monte Carlo code based on GEANT4 has been developed. The structure of the experimental system has been modelled in the following constituents: a 2.3 m height steel prism without top cover containing 1L NaI(Tl) coupled to a photomultiplier tube, MCA, solar panel and the pole have not been simulated because their contribution were considered negligible in the attenuation balance (see Figure 9.3.

Each components interact with radiation depending on its chemical and density propriety. The physical and chemical characteristics of each constituent element are presented in Table 9.1 and 9.2. The dimensions of the simulated environment where the detector is located are shown in the Table 9.3 and Figure 9.4.

The reconstruction of input radionuclides concentrations in soil derived from HPGe measurements on collected samples (see Table 8.9), and the the chemical composition of soil derived from the X-ray fluorescence measurements (see Table 8.8), the characteristics of the source emission is described in the Table 9.4.

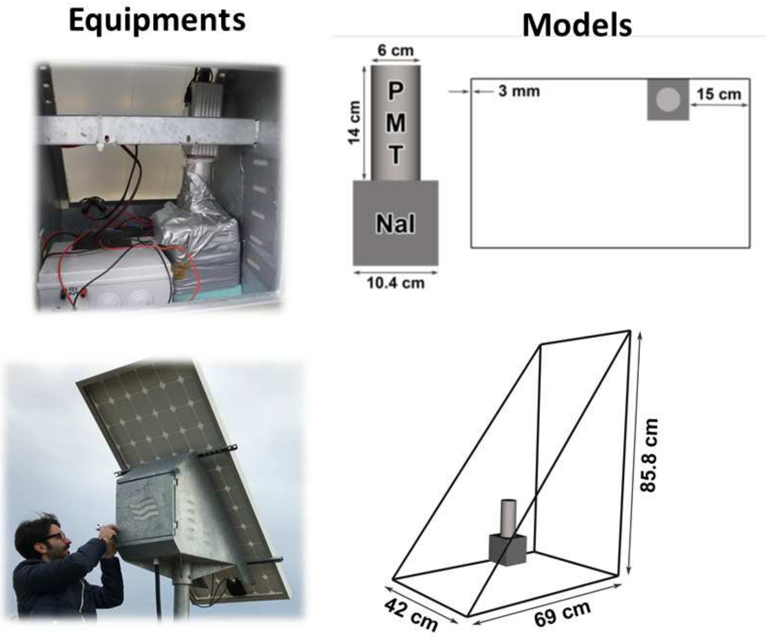

Figure 9.3: a scheme of the geometrical model of gamma station adopted for the Monte Carlo simulation.

Table 9.1: geometrical dimensions, physical and chemical features of the the steel box model.

Steel Box			
Component	**Density [g/cm^3]**	**Dimensions [cm]**	**% by weight**
Prism	7.93	Width = 42.0	Fe = 69.17
		Height = 85.8	Mn = 2.00
		Length = 69.0	Cr = 19.00
			Ni = 9.00
		Thickness = 0.3	C = 0.08
			S = 0.75

Table 9.2: geometrical dimensions, physical and chemical features of the detector model.

Detector			
Component	**Density [g/cm^3]**	**Dimensions [cm]**	**% by weight**
Photomultipier casing	7.93	Diameter = 6	Fe = 69.17
		Height = 14	Mn = 2.00
			Cr = 19.00
			Ni = 9.00
		Thickness = 0.3	C = 0.08
			S = 0.75
1 L NaI	3.67	Width = 10.3	NaI = 100
		Height = 10.3	
		Length = 10.3	
NaI casing	2.34	Width = 10.4	Fe = 69.17
		Height = 10.4	Mn = 2.00
		Length = 10.4	Cr = 19.00
			Ni = 9.00
		Thickness = 0.1	C = 0.08
			S = 0.75

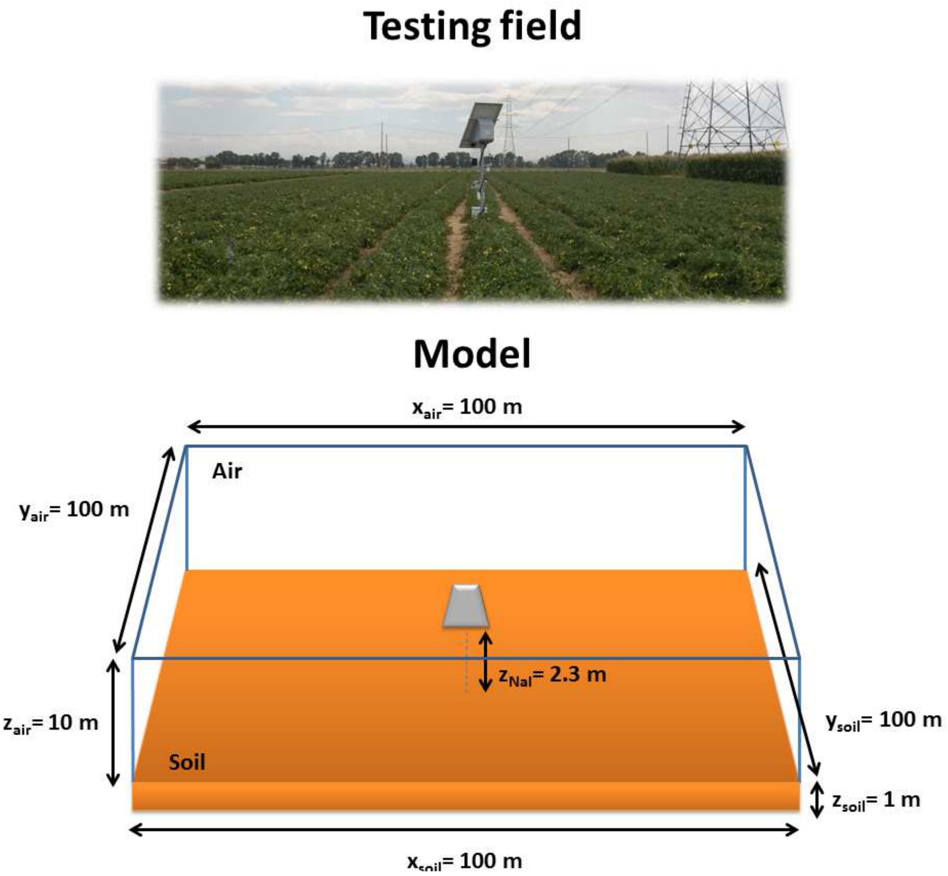

Figure 9.4: a scheme of the geometrical model of environment

.

Table 9.3: geometrical parameters adopted of the environmental model.

Enviroment dimensions [m]	
z_{air}	10
x_{air}	100
y_{air}	100
z_{soil}	1
x_{soil}	100
y_{soil}	100

Table 9.4: source parameters adopted in the simulation.

Simulated source	
Total number of photon simulated	$2.23 \cdot 10^8$
Photon live energy threshold [keV]	200
Irradiation angle	4π

9.1.4 Hydrological simulation software

Physically-based hydrological models develop a description of the water balance phenomena through classical physics equations (e.g. the equation of mass conservation and quantity of motion). The model allows you to specify boundary conditions that vary over time and space, the numerical formulation of the model produces a non-linear system that is solved by successive approximations.

To investigate the evolution of soil water movements after a precipitation event at different depths two different software were used: CRITERIA and Aquacrop.

CRITERIA is a suite of soil water balance and crop modelling systems developed by the Regional Environmental Protection Agency (ARPA) of the Emilia-Romagna region, Italy Criteria [134]. AquaCrop is the crop growth model developed by FAO simulates daily biomass production and final crop yield in relation to water supply and consumption and agronomic management, based on plant and soil water [135]. Both software simulate the balance and movement of water in the soil profile and required input data of weather, crop, soil, and management practices. The main inputs needed for the Aquacrop and CRITERIA software are listed in the Table 9.5.

Table 9.5: main input needed for hydrological models.

Input	Description	Criteria	Aquacrop
Tmax [°C]	Maximum air temperature	X	X
Tmin [°C]	Minimum air temperature	X	X
ET0 [mm/day]	Reference evapotranspiration	X	X
Soil Texture [%]	Proportions of sand, silt, and clay in the fine earth of a soil.	X	X
Wilting Point (WP) [%][m^3/m^3]	Soil water content when plants cannot obtain water from the soil	-	X
Field capacity (FC) [%][m^3/m^3]	Water content which can be retained by a soil after excess moisture has drained by gravity.	-	X
Saturation [%][m^3/m^3]	Soil water content when all pores are filled with water	-	X
Water retention curve models	Relationship between the water content, θ, and the soil water potential, Ψ characterized by several models (e.g. Van Genuchten, Campbell).	X	-
Saturated hydraulic conductivity (Ks) [cm/hr]	Coefficient that expresses the rate of water flow through saturated porous media.	X	X
Soil horizon [cm]	Soil horizontal layers range.	X	X
Bulk density [g/cm^3]	Apparent density of soil.	X	-
Cultivation	Type of crop.	X	X
Planting	Planting time.	X	X
Harvesting	Harvesting time.	X	X
Irrigation [mm]	Quality of irrigation water	X	X
Rain [mm]	Quality of rainwater	X	X
Methods of irrigation	(ie. surface irrigation, sprinkler irrigation)	-	X

9.2 Results

The data taking started on the 03/04/2017 and ended the 02/11/2017 the data were acquired for the entire growing season of tomatoes and even in the periods before planting and after harvesting (Table 8.2). During this period all the instruments were contemporaneity operational for 97.5 % of the time, with a single interruption from 09/06/2017 to 16/06/2017, the row data produced are $\sim$ 350 GB. The following subsections disclose the organization of the data and the results obtained from the analysis.

9.2.1 Data organization

The agrometeorological station measurements (see Table 8.1) are taken with a relatively high acquisition rate (meanly every 5-10 minutes) and, through a GPRS connection, data is sent to LiveData User Interface. This software consents to have real-time access to measurements from any Internet connected device and to download the output file with all meteorological data in a CSV. The precipitation and air temperature data of a second agrometeorological station in a nearby field have been added as support in case of malfunction (in the Table 9.6 is referred to as "support station").

The spectral analysis on a gamma station acquisition has been performed using a software developed in ROOT dedicated to the management of the radiometric data recorded. The list mode file are offline processed to generate the gamma spectra corresponding to 15 minutes acquisitions after the application of the energy calibration procedure. Abundances of U, K, Th were estimated with three different spectral analysis: Windows Analysis Method, Full Spectrum Analysis Non Negative Least Square and Monte Carlo (see Chapter II).

Thanks to a specially developed management software the gamma data were temporally aligned with the meteorological data and organized in a single database with a temporal resolution of 15 minutes. The output field number is 42 (see Table 9.6) and the total entry are 20448.

Table 9.6: for each entry of dataset every 15 minutes the following data are compiled.

ID	Descriptions	Units
1	Date	gg/mm/aa
2	Time	hh:mm:ss
3	Acquisition time	[s]
4	Gross counts rate in the ^{214}Pb [320 - 380 keV] window	[cps]
5	Net counts rate in the ^{214}Pb [320 - 380 keV] window	[cps]
6	Gross counts rate in the ^{214}Bi [550 - 670 keV] window	[cps]
7	Net counts rate in the ^{214}Bi [550 - 670 keV]window	[cps]
8	Gross counts rate in the ^{40}K [1370 - 1570 keV] window	[cps]
9	Net counts rate in the ^{40}K [1370 - 1570 keV] window	[cps]
10	Gross counts rate in the ^{214}Bi [1660 - 1860 keV] window	[cps]
11	Net counts rate in the ^{214}Bi [1660 - 1860 keV] window	[cps]
12	Gross counts rate in the ^{214}Bi [2000 - 2400 keV] window	[cps]
13	Net counts rate in the ^{214}Bi [2000 - 2400 keV] window	[cps]
14	Gross counts rate in the ^{208}Tl [2410 - 2810 keV] window	[cps]
15	Net counts rate in the ^{208}Tl [2410 - 2810 KeV] window	[cps]
16	Total terrestrial counts [0.3-3MeV]	[cps]
17	Total terrestrial net counts [0.3-3MeV]	[cps]
18	Total counts [3-5MeV]	[cps]
19	Total net counts [3-5MeV]	[cps]
20	Equivalent uranium (eU) abundance calculated with Windows Analysis Method	[ppm]
21	Potassium abundance calculated with Windows Analysis Method	[%]
22	Equivalent Thorium (eTh) abundance calculated with Windows Analysis Method	[ppm]
23	Equivalent uranium (eU) abundance calculated with Full Spectrum Analysis Method	[ppm]
24	Potassium abundance calculated with Full Spectrum Analysis Method	[%]
25	Equivalent Thorium (eTh) abundance calculated with Full Spectrum Analysis Method	[ppm]
26	Equivalent uranium (eU) abundance calculated with Monte Carlo Method	[ppm]
27	Potassium abundance calculated with Monte Carlo Method	[%]
28	Equivalent Thorium (eTh) abundance calculated with Monte Carlo Method	[ppm]
29	Atmosferic Pressure	[hPa]
30	Internal Temperature	[C°]
31	Wind Direction	[°]
32	Wind Speed	[m/s]
33	Wind Gust	[m/s]
34	Air Temperature	[C°]
35	Air Humidity	[%]
36	Dewpoint	[C°]
37	Visibile Radiation	[W/m^2]
38	UV Radiation	[Wh/m^2]
39	External Temperature	[C°]
40	Rain	[mm]
41	Rain measured with support station	[mm]
42	Air Temperature measured with support station	[C°]

9.2.2 Calibrations

The calibration of the gamma station was carried out on September 18 when the field was without a vegetative cover (see Table 9.8). The ^{40}K spectral window has a significant number of events $\sim 3.6 \cdot 10^4$ counts per hour with a mean associated statistical noise of $\sim 0.5\%$. The K_{0s} values were averaged over the entire sampling time (Table 9.7), and w_0 was obtained averaging the gravimetric water content measurements of the first 20 cm of soil (see Table 8.7). A subsequent sampling was done on September 21 (Table 9.7), in order to estimate uncertainty on gamma water contents measurements θ_K (using eq. 9.8) the uncertainty on the counts rate and on water content gravimetric measurements was propagate through Gaussian random number generator with a sigma value equal to the standard deviation of measurements. The result is a Gaussian distribution with mean value of $\theta_K = 24.5 \pm 3.8$ $[m^3 m^{-3}]$ (see Figure 9.5).

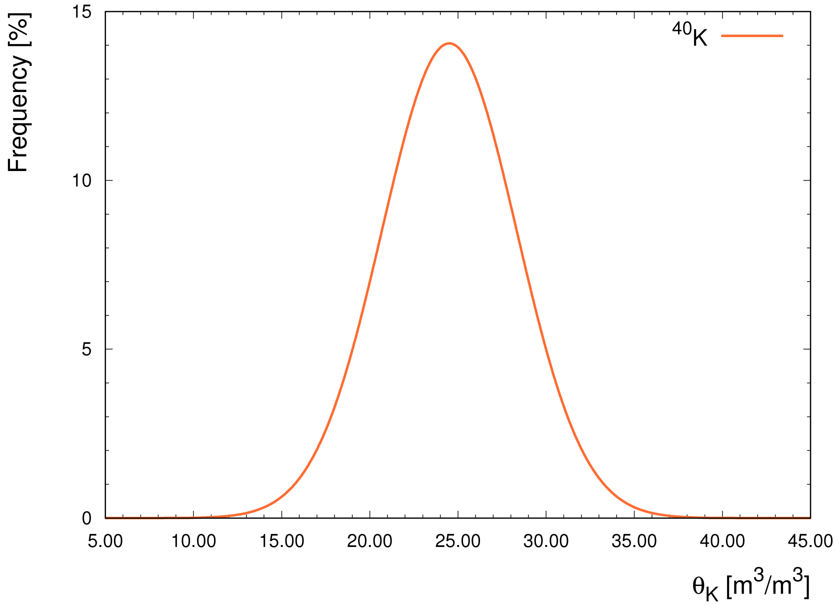

Figure 9.5: distribution of θ_K calculated using Eq. 9.8 with Gaussian random number generator.

Table 9.7: calibration data of September 18 and comparison with the values of θ_K (using Eq. 9.12) and θ_G in the subsequent sampling of September 21.

Day	Time	K_s [cps]	θ_G [%]	θ_K [%]	$\Delta\theta$[%]
Calibration 18/09/2017	10:00 - 11:00	11.70 ± 0.23	21.9 ± 1.1	21.9 ± 2.8	0.0
21/09/2017	11:00-12:00	11.49 ± 0.20	23.7 ± 1.5	24.5 ± 2.0	3.3

9.2.3 Water content calculated with gamma ray measurements

The volumetric water content was estimated using the Eq. 9.8. As can be seen in Figure 9.6 the estimated water content θ_K is particularly sensitive to rainfall events: the soil wetting and drying is clearly visible. The value of θ_K are compared with the value of the gravimetric samples θ_G collected in July when tomato plants with ripe fruits covered the field. Since the contribution of radiation detected depends by the soil thickness (see Section 9.1.1) θ_G is calculated by weighting averaging, assigning weight factors depending on the soil depth (0.79 for 0-10 cm , 0.16 for 10-20 cm samples and 0.05 for 20-30 cm). From table 9.8 is visible a systematic overestimation of the water content θ_K respect to θ_G of maximum $\sim$ 57 %.

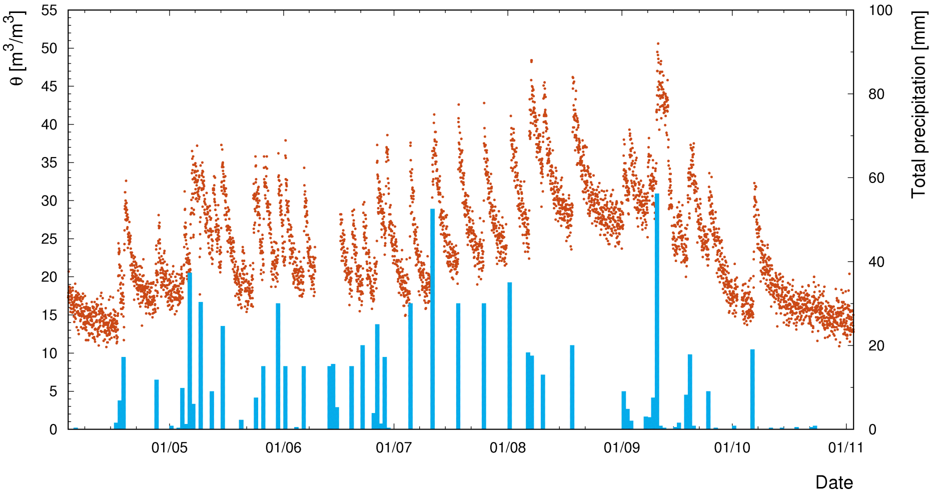

Figure 9.6: volumetric water content θ_K calculated using the Eq. 9.8. The rains and irrigations are in blue (data taken from Table 8.3 and 6)

.

Table 9.8: comparison with the values of θ_K (using Eq. 9.8) and θ_G taken in July.

Day	**Time**	θ_G [%]	θ_K [%]	$\Delta\theta$ [%]
24/07/2017	10:00-11:00	16.7 ± 2.8	26.3 ± 2.0	57.4
26/07/2017	10:00-12:00	26.5 ± 2.8	34.4 ± 1.4	29.8
28/07/2017	10:00-11:00	18.9 ± 2.9	27.2 ± 0.4	43.8

In our measures we need to take into account the vegetative coverage of tomato plants for this reason is necessary to use the Eq. 9.12. Monte Carlo simulation were performed with an increasing number of water layer to determine the attenuation of the signal in the ^{40}K window as a function of tomato plants water equivalent PWM. The presence of 5 mm of water layer produces an overestimation of ~50% of the water content in the soil (Figure 9.7).

A straight line function was fitted for determined Λ in function of plant water mass (Figure 9.7). A linear regression model was fitted using the plant water mass values (see Table 8.4) to obtain PWM as a function of plants age 9.8. The slope value is 0.00351 h and the origin start when the tomatoes were planted. The application of signal correction due to the prevalence of vegetative coverage is effective, the gravimetric measurement θ_G and θ_K are compatible at 1σ level with a maximum difference between the central values of $\sim$8%(see Table 9.9).

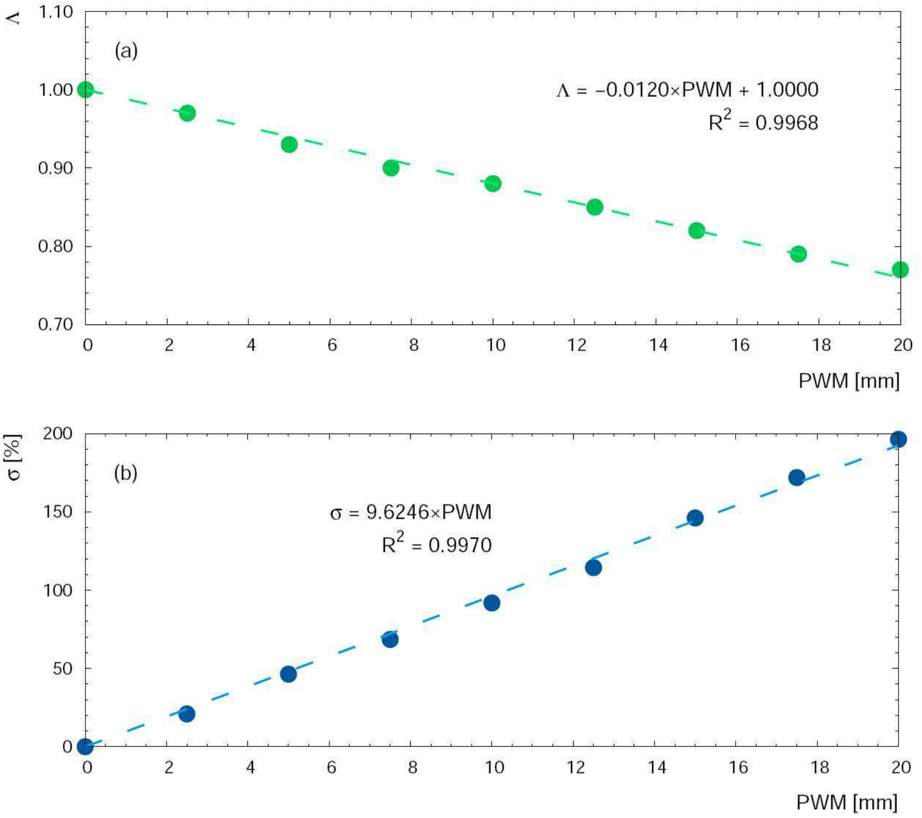

Figure 9.7: attenuation Λ for the characteristic emission energies of ${}^{40}K$ in function of plant water mass (PWM [mm]) (panel a) and effect of overestimation of water content using Eq. 9.8 (panel b).

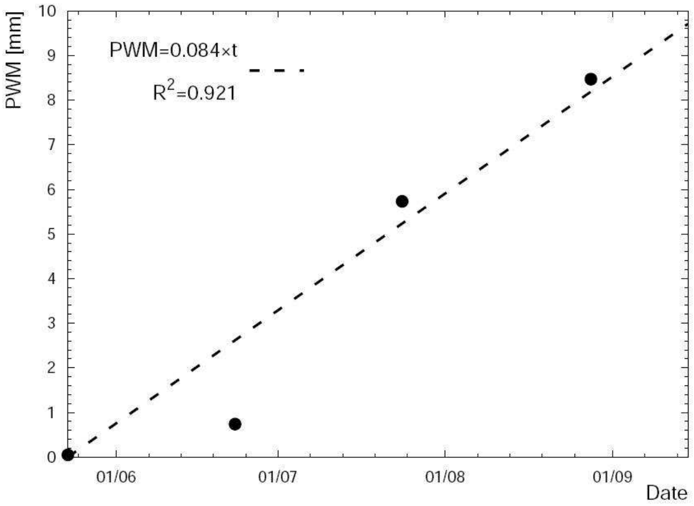

Figure 9.8: plant water mass (PWM) function, the black points represents PWM estimated from destructive above-ground biomass samples.

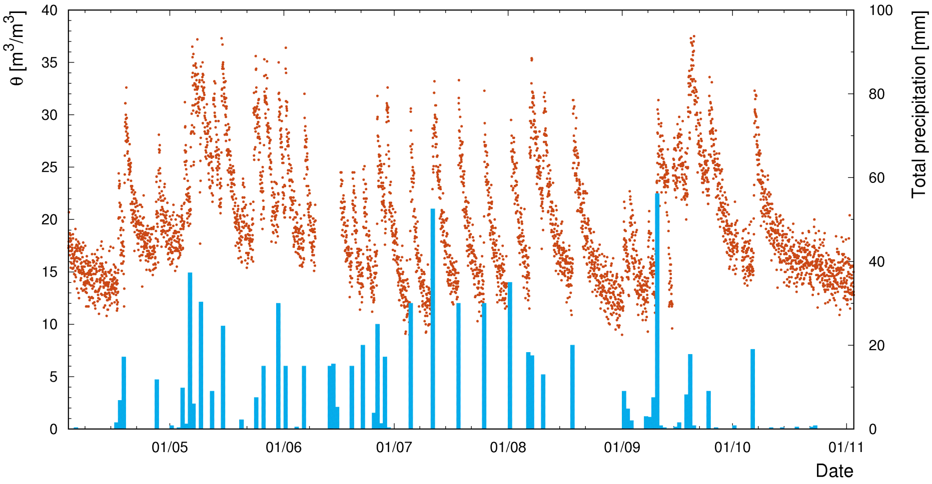

Figure 9.9: volumetric water content θ_K calculated using the Eq. 9.12 taking to account the $\Lambda(PWM)$ correction in the presence of tomatoes plants. The rains and irrigations are in blue (data taken from Table 8.3 and 6 of Appendix D).

Table 9.9: comparison with the measurements of θ_K (using Eq. 9.12 taking to account the $\Lambda(PWM)$ correction) and θ_G taken in July.

Day	**Time**	θ_G [%]	θ_K [%]	$\Delta\theta$ [%]
24/07/2017	10:00-11:00	16.7 ± 2.8	17.0 ± 1.9	1.9
26/07/2017	10:00-12:00	26.5 ± 2.8	24.3 ± 1.3	-8.3
28/07/2017	10:00-11:00	18.9 ± 2.9	17.9 ± 1.5	-5.6

9.2.4 Hydrological simulation software and gamma ray measurements

To compare qualitatively the result of the water content obtained with gamma spectroscopy measurements with hydrological models two simulation software were used: CRITERIA and Aquacrop described in Section 9.1.4. Inserting the characteristics of the soil (summarized in Table 9.10), meteorological data and the characteristics of cultivation (see Table 9.5) was simulated the water content of the top 40 cm of soil and compared with the results of gamma spectroscopy measurements averaged on 24 h, the time resolution of the simulations is 1 day, an output example of CRITERIA is show in Figure 9.10.

The Aquacrop input soil-water characteristic have been estimated from the percentage of sand (%s) and clay (%c) [136]. The porosity was derived from following equation:

$$\theta_s = 0.332 - 7.251 \cdot 10^{-4}(\%s) + 0.1276 \cdot 1og_{10}(\%c) \tag{9.13}$$

The wilting point (WP) and field capacity (FC) were derived from the water retention function:

$$\Psi = A\theta^B \tag{9.14}$$

for Ψ=33 Kpa and Ψ=1500 Kpa respectively, where:

$$A = exp[-4.396 - 0.0715(\%c) - 4.880 \cdot 10^{-4}(\%s)^2 - 4.285 \cdot 10^{-5}(\%s)^2(\%c)] \cdot 100 \tag{9.15}$$

$$B = -3.140 - 3.484 \cdot 10^{-5}(\%s)^2(\%c) \tag{9.16}$$

Table 9.10: main parameters used in the hydrological simulation software.

Parameter	**Criteria**	**Aquacop**
Soil Texture	Sandy Loam	Sandy Loam
Wilting Point (WP) [%]	-	11.3
Field capacity (FC) [%]	-	21.6
Saturation [%]	-	43.9
Water retention curve models	Modified Van Genuchten	-
Saturated hydraulic Conductivity (K_s) [cm/day]	240	240
Soil horizon [cm]	0-30 and 30-200	0-30 and 30-200
Bulk density [g/cm3]	1.345	-
Cultivation	Tomatoes	Tomatoes
Methods of irrigation	-	Sprinkler irrigation

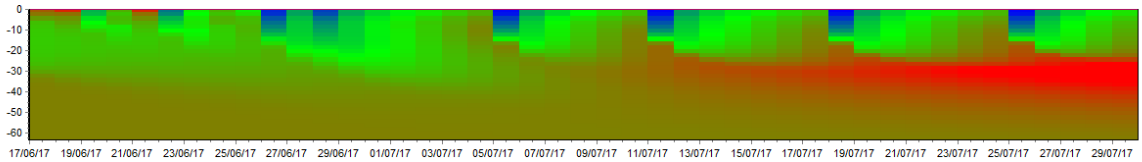

Figure 9.10: a typical output of CRITERIA: the water content in soil expressed in $mm\ cm^{-1}$ in function of depth and time, the blue represents the values close to the saturation, the red represent the values close to the wilting point.

Both models are in agreement with the gamma spectroscopy measurements trend but they seem to overestimate the water content respect to the gamma measurements in some cases after the irrigation events in July. After the harvesting tomatoes, at the end of September, the models curves seem to underestimate the water content after the precipitation while reach higher water content values in the drying phases (see Figure 9.11). A future improvement would be investigating the origin of these differences through a more in-depth analysis.

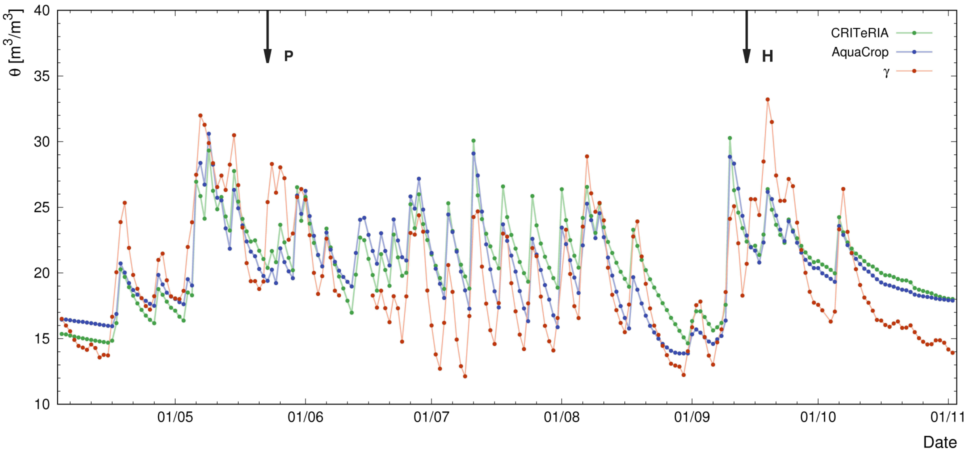

Figure 9.11: volumetric water content θ_K (red) and volumetric water content in first 40 cm of soil simulated with CRITERIA (green) and Aquacrop (blue). The upper arrows indicate the tomatoes planting day (P) and the harvesting tomatoes day (see Table 8.2) (H)

9.3 Final remarks

Variations in soil moisture can be detected by terrestrial gamma-ray spectrometry: with an opportune calibration is possible to estimate the water content in the soil with a greater sensitivity for the first 20 cm of depth. This study has set the goal to develop a gamma station equipped with a sodium iodide gamma-ray detector flanked to an agrometeorological station with the aim of measuring the water content in a tomatoes testing field. A large number of samples was collected to characterize the soil chemically and physically for calibration purpose. The gamma station is equipped with a sodium iodide gamma-ray detector able to measure the gamma radiation coming from 0.2 ha. The instruments were contemporaneity operational for 97.5 % for a duration of $\sim$ 7 months. The acquisition data were post-processed, temporally aligned and organized in a single database with a temporal resolution of 15 minutes. The gamma measurements have shown a great sensitivity to irrigation and rainfall events highlighting the wetting and drying processes in the soil. The values showed that vegetative cover produces an attenuation effect that causes an overestimation of the water content in the soil.

The water content in tomato plants in as a function of time was estimated from destructive above-ground biomass samples. Monte Carlo simulation were performed in order to estimate the attenuation of the signal produced by tomato plants during their development. The correction was effective because the water content estimated with gamma method are compatible at 1σ level with gravimetric measurements of the soil with a maximum difference between the central values of ∼8%.

The hydrological simulation softwares CRITERIA and Aquacrop were used to compare qualitatively the water content of the first ∼40 cm of soil: both are in good agreement with the gamma spectroscopy measurements trend. A future improvement would be defining a metric in order to quantitatively assess the degree of agreement between the hydrological models and gamma spectroscopy measurements.

Conclusions

After the master degree in astrophysics I had the opportunity to start my PhD in physics at the University of Ferrara. In these three years I came in contact with the fascinating field of gamma spectroscopy applied to the environmental monitoring. This topic is strongly connected to other disciplines such as engineering, computer science and the Earth sciences. It stimulated me to grow up both professionally and humanly, in particular improving my communication and technical skills. My research activities allowed me to build a network of experts with who I had the pleasure to public many papers.

The main gamma terrestrial emitters are ^{40}K, ^{214}Bi (belonging to U decay chain) and ^{208}Tl (belonging to Th decay chain), which can be effectively investigated by Airborne Gamma-Ray Spectroscopy survey (AGRS). Since these measurements are acquired dynamically with low cont rates, the study of statistical and systematic uncertainties is the mandatory task which I took care. In particular the severe backgrounds, variable in time and space, constituted by aircraft materials, cosmic rays and atmospheric radon is a challenge for the entire research branch. For this purpose $\sim$5 hours of AGRS surveys over the sea have been performed in a range of heights (35 - 3066) m with 4L of NaI(Tl) crystals mounted on a ultralight prototype aircraft. On the base of new theoretical model for atmospheric radon profile, the fit of data permits to estimate a radon concentration of (0.96 ± 0.07) Bq/m^3 ^{222}Rn distributed up to (1318 ± 22) m, in agreement with the values reported in scientific literature. From this research a minimum detectable abundances of 0.05 $\cdot 10^{-2}$ g/g for K, 0.4 μg/g for U and 0.8 μg/g for Th has been successfully evaluated and published.

Since a precise evaluation of flight altitude is fundamental for avoiding systematic effects in gamma spectrum reconstruction, the aircraft was equipped with four low-cost GNSS receivers, one Inertial Measurement Unit, one radar altimeter and two barometric sensors. My GNSS double-difference post-processing analysis enhanced significantly the data quality, reaching an accuracy better than 2% at flight altitude higher than $\sim$80 m. This uncertainty of the vertical position affects with an error of 2% the estimation of ground total activity measured at 100 m height. This issue is not commonly considered in the budget of the uncertainties and this work makes a significant contribution to this theme.

My experience in data analysis with AGRS surveys has been useful for enhance the performance of ZaNaI, a portable gamma-ray spectrometer designed for accurate and quick in situ measurements. In particular I analyzed the data collected during an extensive radiometric survey in Northeastern Sardinia. On the base of 167 HPGe measurements and 368 NaI measurements the spatial variability of eU abundance has being modeled using the Kriging with Variance of Measurement Error method, a geostatistical tool that assigns different levels of confidence to the data acquired with the two gamma-ray detectors. It is one of the most successful result of this survey and it allowed to realize the map of the eU abundance distribution of Northeastern Sardinia, together with together with the uncertainties of the estimations.

With this portable gamma-ray spectrometer I had the opportunity to design a laboratory experience with the aim to explain the fundamentals of the in-situ radioactivity measurement during the Summer School in Nuclear Physics and Technologies in Ferrara. The simplicity of use through Android applications, make ZaNaI an excellent instrument for educational purposes. The acquisitions performed by the students during the outdoor survey are used to create a map of the radioactivity of the Scientific and Technology Campus of University of Ferrara.

An amazing application of in-situ gamma ray detection has being done in the field of precision agriculture. Since the water mass attenuation coefficient is $\sim$11% higher than those of the typical minerals commonly present in the soil, a gamma spectroscopy measurement is extremely sensitive to the variation of moisture in the pores. With the aim of measuring the water content in the first $\sim$20 centimeters of an area of 0.2 ha, a permanent gamma station equipped 1L NaI(Tl) detector were placed in a tomato crop field. The challenges of these measures is estimate the shielding effect induced by the vegetation growing. Monte Carlo calibration allowed me to tackle this problem successfully: the water content estimated with gamma method are compatible at 1σ level with gravimetric field measurements of the soil with a maximum difference between the central values of $\sim$8%.

The successful results in AGRS measurements and in-situ gamma-ray surveys have confirmed that gamma spectroscopy is a spectacular technique for exploring environment. The applications of refined methods of analysis and new equipments in precision agriculture, in homeland security, in applied geophysics and in environmental monitoring need to be enhanced, since the great potentiality of this researches are not yet completely exploited.

Bibliography

[1] V. Strati, M. Baldoncini, G. P. Bezzon, C. Broggini, G. P. Buso, A. Caciolli, I. Callegari, L. Carmignani, T. Colonna, G. Fiorentini, E. Guastaldi, M. Kaçeli Xhixha, F. Mantovani, R. Menegazzo, L. Mou, C. Rossi Alvarez, G. Xhixha, and A. Zanon. Total natural radioactivity, veneto (italy). *Journal of Maps*, 11(4):545–551, 2015.

[2] M. Kaçeli Xhixha, M. Albèri, M. Baldoncini, G. P. Bezzon, G. P. Buso, I. Callegari, L. Casini, S. Cuccuru, G. Fiorentini, E. Guastaldi, F. Mantovani, L. Mou, G. Oggiano, A. Puccini, C. Rossi Alvarez, V. Strati, G. Xhixha, and A. Zanon. Uranium distribution in the variscan basement of northeastern sardinia. *Journal of Maps*, pages 1–8, 2015.

[3] J. Wilford and B. Minty. Chapter 16 the use of airborne gamma-ray imagery for mapping soils and understanding landscape processes. 31:207–610, 2006.

[4] Abdullahi Hassan Mohamud, Juan Sebastián Cózar, Julio Rodrigo-Naharro, and Luís Pérez del Villar. Distribution of u and th in an iberian u-fertile granitic complex (nw, spain): airborne-radiometry, chemical and statistical approaches. *Journal of Geochemical Exploration*, 148(0):40–55, 2015.

[5] P. Kock, C. Raaf, and C. Samuelsson. On background radiation gradients–the use of airborne surveys when searching for orphan sources using mobile gamma-ray spectrometry. *J Environ Radioact*, 128:84–90, 2014. Kock, Peder Raaf, Christopher Samuelsson, Christer eng Evaluation Studies Research Support, Non-U.S. Gov't England 2013/12/11 06:00 J Environ Radioact. 2014 Feb;128:84-90. doi: 10.1016/j.jenvrad.2013.10.022. Epub 2013 Dec 8.

[6] T. Saito, Y. Kurihara, Y. Koike, I. Tanihata, M. Fujiwara, H. Sakaguchi, A. Shinohara, and H. Yamamoto. Altitude distribution of radioactive cesium at fuji volcano caused by fukushima daiichi nuclear power station accident. *Journal of Radioanalytical and Nuclear Chemistry*, 303(2):1613–1615, 2015.

[7] David Beamish. Enhancing the resolution of airborne gamma-ray data using horizontal gradients. 132:75–86, 2016.

[8] Enrico Guastaldi, Marica Baldoncini, Giampietro Bezzon, Carlo Broggini, Giampaolo Buso, Antonio Caciolli, Luigi Carmignani, Ivan Callegari, Tommaso Colonna, Kujtim Dule, Giovanni Fiorentini, Merita Kaçeli Xhixha, Fabio Mantovani, Giovanni Massa, Roberto Menegazzo, Liliana Mou, Carlos Rossi Alvarez, Virginia Strati, Gerti Xhixha, and Alessandro Zanon. A multivariate spatial interpolation of airborne gamma-ray data using the geological constraints. 137:1–11, 2013.

[9] Edgar Romeo Herrera de Figueiredo Iza, Adriana Maria Coimbra Horbe, and Adalene Moreira Silva. Boolean and fuzzy methods for identifying lateritic regoliths in the brazilian amazon using gamma-ray spectrometric and topographic data. 269:27–38, 2016.

[10] Brian Minty and Ross Brodie. The 3d inversion of airborne gamma-ray spectrometric data. 47(2):150–157, 2016.

[11] I. Baroň, R. Supper, E. Winkler, K. Motschka, A. Ahl, M. Čarman, and š. Kumelj. Airborne geophysical survey of the catastrophic landslide at stože, log pod mangrtom, as a test of an innovative approach for landslide mapping in steep alpine terrains. 13(10):2543–2550, 2013.

[12] A. Keaney, J. McKinley, C. Graham, M. Robinson, and A. Ruffell. Spatial statistics to estimate peat thickness using airborne radiometric data. 5:3–24, 2013.

[13] Cheikh Mohamedou, Timo Tokola, and Kalle Eerikäinen. Applying airborne γ-ray and DEM-derived attributes to the local improvement of the existing individual-tree growth model for diameter increment. 155:248–256, 2014.

[14] Mats Söderström, Gustav Sohlenius, Lars Rodhe, and Kristin Piikki. Adaptation of regional digital soil mapping for precision agriculture. 17(5):588–607, 2016.

[15] John Cardarelli, Mark Thomas, Timothy Curry, Robert Kroutil, Jeff Stapleton, David Miller, Gary Small, and Brian Dess. Real-time radionuclide identification and mapping capabilities of the u.s. environmental protection agency's airborne spectral photometric environmental collection technology. In Samuel Apikyan and David Diamond, editors, *Nuclear Terrorism and National Preparedness*, NATO Science for Peace and Security Series B: Physics and Biophysics, pages 105–116. Springer Netherlands, 2015.

[16] R. S. Detwiler, D. M. Pfund, M. J. Myjak, J. A. Kulisek, and C. E. Seifert. Spectral anomaly methods for aerial detection using KUT nuisance rejection. 784:339–345, 2015.

[17] Peder Kock, Jan Lanke, and Christer Samuelsson. A real-time statistical alarm method for mobile gamma spectrometry—combining counts of pulses with spectral distribution of pulses. 681:55–60, 2012.

[18] J. A. Kulisek, J. E. Schweppe, S. C. Stave, B. E. Bernacki, D. V. Jordan, T. N. Stewart, C. E. Seifert, and W. J. Kernan. Real-time airborne gamma-ray background estimation using NASVD with MLE and radiation transport for calibration. 784:287–292, 2015.

[19] Bucher, B., Guillot, L., Strobl, C., Butterweck, G., Gutierrez, S., Thomas, M., and Hohmann, C., Krol, I., Rybach, L., Schwarz, G. International intercomparison exercise of airborne gammaspectrometric systems of germany, france and switzerland in the framework of the swiss exercise ARM07. 2009.

[20] R.L. Grasty, M. P. Bates, and A. Smetny-Sowa. Monitoring airborne gamma ray spectrometer sensitivities using the natural background. 2015(1):1, 2015.

[21] Peder Kock, Christopher Rääf, and Christer Samuelsson. On background radiation gradients – the use of airborne surveys when searching for orphan sources using mobile gamma-ray spectrometry. 128:84–90, 2014.

[22] D. C. W. Sanderson, A. J. Cresswell, and D. C. White. The effect of flight line spacing on radioactivity inventory and spatial feature characteristics of airborne gamma-ray spectrometry data. 29(1):31–46, 2008.

[23] G. A. Sandness, J. E. Schweppe, W. K. Hensley, J. D. Borgardt, and A. L. Mitchell. Accurate modeling of the terrestrial gamma-ray background for homeland security applications. In *2009 IEEE Nuclear Science Symposium Conference Record (NSS/MIC)*, pages 126–133, 2009.

[24] V. Strati, M. Baldoncini, G.P. Bezzon, C. Broggini, G.P. Buso, A. Caciolli, I. Callegari, L. Carmignani, T. Colonna, G. Fiorentini, E. Guastaldi, M. Kaçeli Xhixha, F. Mantovani, R. Menegazzo, L. Mou, C. Rossi Alvarez, G. Xhixha, and A. Zanon. Total natural radioactivity, veneto (italy). *Journal of Maps*, 11(4):545–551, 2015.

[25] Ye Cao, Xiao-Bin Tang, Peng Wang, Jia Meng, Xi Huang, Liang-Sheng Wen, and Da Chen. Spectrum correction algorithm for detectors in airborne radioactivity monitoring equipment NH-UAV based on a ratio processing method. 797:290–296, 2015.

[26] ChunHui Gong, GuoQiang Zeng, LiangQuan Ge, Xiaobin Tang, and ChengJun Tan. Minimum detectable activity for NaI(tl) airborne γ-ray spectrometry based on monte carlo simulation. 57(9):1840–1845, 2014.

[27] Xiao-Bin Tang, Jia Meng, Peng Wang, Ye Cao, Xi Huang, Liang-Sheng Wen, and Da Chen. Efficiency calibration and minimum detectable activity concentration of a real-time UAV airborne sensor system with two gamma spectrometers. 110:100–108, 2016.

[28] Enrico Guastaldi, Marica Baldoncini, Giampietro Bezzon, Carlo Broggini, Giampaolo Buso, Antonio Caciolli, Luigi Carmignani, Ivan Callegari, Tommaso Colonna, Kujtim Dule, Giovanni Fiorentini, Merita Kaçeli Xhixha, Fabio Mantovani, Giovanni Massa, Roberto Menegazzo, Liliana Mou, Carlos Rossi Alvarez, Virginia Strati, Gerti Xhixha, and Alessandro Zanon. A multivariate spatial interpolation of airborne γ-ray data using the geological constraints. *Remote Sensing of Environment*, 137(0):1–11, 2013.

[29] Eugene Druker. Processing of airborne gamma-ray spectrometry using inversions. *ASEG-PESA-AIG*, 2016.

[30] Johan Beekhuizen, Gerard B. M. Heuvelink, Jan Biesemans, and Ils Reusen. Effect of dem uncertainty on the positional accuracy of airborne imagery. *IEEE Transactions on Geoscience and Remote Sensing*, 49(5):1567–1577, 2011.

[31] Arun Vydhyanathan, Giovanni Bellusci, Henk Luinge, and Per Slycke. The next generation xsens motion trackers for industrial applications. *Xsens*, 2015.

[32] Florent Lyard, Fabien Lefevre, Thierry Letellier, and Olivier Francis. Modelling the global ocean tides: modern insights from fes2004. *Ocean Dynamics*, 56(5-6):394–415, 2006.

[33] Eugenio Realini and Mirko Reguzzoni. gogps: open source software for enhancing the accuracy of low-cost receivers by single-frequency relative kinematic positioning. *Measurement Science and Technology*, 24(11):115010, 2013.

[34] Nikolaos K. Pavlis, Simon A. Holmes, Steve C. Kenyon, and John K. Factor. The development and evaluation of the earth gravitational model 2008 (egm2008). *Journal of Geophysical Research: Solid Earth*, 117(B4):n/a–n/a, 2012.

[35] David C. Hoaglin, Boris Iglewicz, and John W. Tukey. Performance of some resistant rules for outlier labeling. *Journal of the American Statistical Association*, 81(396):991–999, 1986.

[36] M. Smyrnaios and S. Schön. Gnss antenna impact on the resulting multipath effects in carrier-phase and signal amplitude. 143:735–742, 2015.

[37] Johan S. Lofgren, Rüdiger Haas, and Jan M. Johansson. Monitoring coastal sea level using reflected gnss signals. *Advances in Space Research*, 47(2):213–220, 2011.

[38] Johan S. Lofgren, Rüdiger Haas, and Hans-Georg Scherneck. Sea level time series and ocean tide analysis from multipath signals at five gps sites in different parts of the world. *Journal of Geodynamics*, 80:66–80, 2014.

[39] J. P. CARR J. M. TRANQUILLA. Gps multipath field observations at land and water sites. *NAVIGATION: Journal of The Institute of Navigation*, 37, 1990.

[40] Maddalena Gilardoni, Mirko Reguzzoni, and Daniele Sampietro. Geco: a global gravity model by locally combining goce data and egm2008. *Studia Geophysica et Geodaetica*, 60(2):228–247, 2016.

[41] Portland State Aerospace Society. A quick derivation relating altitude to air pressure. 2004.

[42] J. Parviainen, J. Kantola, and J. Collin. Differential barometry in personal navigation. pages 148–152, 2008.

[43] National Institute of Standard and Technology website.

[44] International Atomi Energy Agency. *Guidelines for Radioelement Mapping Using Gamma Ray Spectrometry Datag*. Number 1363 in Technical Reports Series. International Atomic Energy Agency, Vienna, 2003.

[45] D. J. Bird, S. C. Corbató, H. Y. Dai, B. R. Dawson, J. W. Elbert, T. K. Gaisser, K. D. Green, M. A. Huang, D. B. Kieda, S. Ko, C. G. Larsen, E. C. Loh, M. Luo, M. H. Salamon, D. Smith, P. Sokolsky, P. Sommers, T. Stanev, J. K. K. Tang, S. B. Thomas, and S. Tilav. Evidence for correlated changes in the spectrum and composition of cosmic rays at extremely high energies. 71(21):3401–3404, 1993.

[46] Pierre Auger Collaboration. Measurement of the energy spectrum of cosmic rays above 1018 eV using the pierre auger observatory. 685(4):239–246, 2010.

[47] UNSCEAR. Sources and effects of ionizing radiation - annex b - exposures of the public and workers from various sources of radiation. United Nation Scientific Committee of the Effects of Atomic Radiation, 2008.

[48] Tatsuhiko Sato. Evaluation of world population-weighted effective dose due to cosmic ray exposure. 6:33932, 2016.

[49] F. Cavalcante, N. C. Silva, H. L. C. Alberti, and A. De Almeida. Effective dose rate evaluation from natural gamma radiation in the region of ribeirao preto, SP-brazil. 46(6):S145–S150, 2011.

[50] P Strand, B. J Howard, A Aarkrog, M Balonov, Y Tsaturov, J. M Bewers, A Salo, M Sickel, R Bergman, and K Rissanen. Radioactive contamination in the arctic—sources, dose assessment and potential risks. 60(1):5–21, 2002.

[51] K.C. Tsui, M.C. Wong, and B.Y. Lee. Field estimation of cosmic contribution to total external gamma radiation in hong kong. 1991.

[52] B. R. S. Minty, A. P. J. Luyendyk, and R. C. Brodie. Calibration and data processing for airborne gamma-ray spectrometry. 17(2):51–62, 1997.

[53] FAA. CARI-6 program to calculate galactic cosmic radiation. Federal Aviation Administration, 2014.

[54] Tatsuhiko Sato. Analytical model for estimating terrestrial cosmic ray fluxes nearly anytime and anywhere in the world: Extension of PARMA/EXPACS. *PLOS ONE*, 10(12):e0144679.

[55] R.L. Grasty and Brian Minty. A guide to the technical specifications for airborne gamma-ray surveys. 1995.

[56] International Atomic Energy Agency. *Airborne Gamma Ray Spectrometer Surveying*. Number 323 in Technical Reports Series. International Atomic Energy Agency, Vienna, 1991.

[57] R. L. Grasty, B. R. Walters, J. Hovgaard, and J. R. LaMarre. Calibration of a 7.6 cm x 7.6 cm (3 inch x 3 inch) sodium iodide gamma ray spectrometer for air kerma rate. 94(4):309–316, 2001.

[58] Nguyen Duc Tuan, Nguyen Van Sy, Vu Van Tien, Nguyen Thi Thuy Mai, Nguyen Thi Bao My, Chu Vu Long, and Nguyen Bach Viet. Design and construction of the portable gamma-ray spectrometer for environmental dose rate measurement and radioisotope identification. Nguyen Thi Phuong Lan (Ed.). Vietnam, 2013.

[59] N Mercier and C Falguères. Field gamma dose-rate measurement with a NaI (tl) detector: re-evaluation of the “threshold” technique. pages 1–4, 2007.

[60] F. Spurný and T. Daschev. On board aircrew dosimetry with a semiconductor spectrometer. 100(1):525–528, 2002.

[61] R. Kleinschmidt and D. Watson. Terrestrial gamma radiation baseline mapping using ultra low density sampling methods. 151 Pt 3:609–622, 2016.

[62] J. F. Bottollier-Depois, P. Beck, B. Bennett, L. Bennett, R. Bütikofer, I. Clairand, L. Desorgher, C. Dyer, E. Felsberger, E. Flückiger, A. Hands, P. Kindl, M. Latocha, B. Lewis, G. Leuthold, T. Maczka, V. Mares, M. J. McCall, K. O'Brien, S. Rollet, W. Rühm, and F. Wissmann. Comparison of codes assessing galactic cosmic radiation exposure of aircraft crew. 136(4):317–323, 2009.

[63] Alastair G. Williams, Wlodek Zahorowski, Scott Chambers, Alan Griffiths, Jörg M. Hacker, Adrian Element, and Sylvester Werczynski. The vertical distribution of radon in clear and cloudy daytime terrestrial boundary layers. 68(1):155–174, 2010.

[64] W. Jacobi and K. André. The vertical distribution of radon 222, radon 220 and their decay products in the atmosphere. *Journal of Geophysical Research*, 68(13):3799–3814, 1963.

[65] K. K. Turekian, Y. Nozaki, and L. K. Benninger. Geochemistry of atmospheric radon and radon products. *Annual Review of Earth and Planetary Sciences*, 5(1):227–255, 1977.

[66] Conen Szegvary and Ciaia. European 222rn inventory for applied atmospheric studies. *Atmospheric Environment*, pages 1536–1539, 2009.

[67] H.A.J.Meijer Manohar, S.N. and M.A.Herber. Radon flux maps for the netherlands and europe using terrestrial gamma radiation derived from soil radionuclides. *Atmospheric Environment*, pages 399–412, 2013.

[68] UNSCEAR. Sources and efffects of ionizing radiation - annex b. United Nations Scientific Committee on the Effects of Atomic Radiation, 2008.

[69] WHO. Handbook on indoor radon: a public health perspective. World Health Organization, 2009.

[70] Jing Chen, Naureen M. Rahman, and Ibrahim Abu Atiya. Radon exhalation from building materials for decorative use. *Journal of Environmental Radioactivity*, 101(4):317–322, 2010.

[71] J. Hulka. Radon in context of natural radiation exposure: the czech experience. *Radiation Protection Dosimetry*, 130(1):14–17, 2008.

[72] Cristina Nuccetelli and Chiara Bolzan. In situ gamma spectroscopy to characterize building materials as radon and thoron sources. *Science of The Total Environment*, 272(1):355–360, 2001.

[73] S Rizzo, M Brai, S Basile, S Bellia, and S Hauser. Gamma activity and geochemical features of building materials: estimation of gamma dose rate and indoor radon levels in sicily. *Applied Radiation and Isotopes*, 55(2):259–265, 2001.

[74] Kyle P. Messier, Ted Campbell, Philip J. Bradley, and Marc L. Serre. Estimation of groundwater radon in north carolina using land use regression and bayesian maximum entropy. *Environmental Science & Technology*, 49(16):9817–9825, 2015.

[75] M. A. Smethurst, R. J. Watson, V. C. Baranwal, A. L. Rudjord, and I. Finne. The predictive power of airborne gamma ray survey data on the locations of domestic radon hazards in norway: A strong case for utilizing airborne data in large-scale radon potential mapping. *Journal of Environmental Radioactivity*, 166, Part 2:321–340, 2017.

[76] J. D. Appleton, E. Doyle, D. Fenton, and C. Organo. Radon potential mapping of the tralee - castleisland and cavan areas (ireland) based on airborne gamma-ray spectrometry and geology. *Journal of Radiological Protection*, 31(2):221, 2011.

[77] IAEA. Sources and measurements of radon and radon progeny applied to climate and air quality studies. *Proceedings of a technical meeting held in Vienna, organized by the International Atomic Energy Agency and co-sponsored by the World Meteorological Organization*, 2012.

[78] S. D. Schery and S. Huang. An estimate of the global distribution of radon emissions from the ocean. *Geophysical Research Letters*, 31(19):L19104, 2004.

[79] Harold L. Beck. Gamma radiation from radon daughters in the atmosphere. *Journal of Geophysical Research*, 79(15):2215–2221, 1974.

[80] C. V. Gogolak. Variation of radon and radon daughter concentrations with height above ground. *Health and Safety Laboratory, U. S. Energy Research and Development Administration New York*, 1977.

[81] B. Minty. Multichannel models for the estimation of radon background in airborne gamma-ray spectrometry. *Geophysics*, 63(6):1986–1996, 1998.

[82] Roland B. Stull. *An Introduction to Boundary Layer Meteorology*. Springer Science & Business Media, 2012.

[83] Cheng J. P. Jia M. Y. Wu R. Feng Y. J. Su C. Y. Feng, T. C. and Chen W. Relationship between soil bulk density and pvr of in situ γ spectra. Nuclear Instruments and Methods in Physics Research Section A: Accelerators, Spectrometers, Detectors and Associated Equipment, 2009.

[84] Xuemeng Chen, Jussi Paatero, Veli-Matti Kerminen, Laura Riuttanen, Juha Hatakka, Veijo Hiltunen, Pauli Paasonen, Anne Hirsikko, Alessandro Franchin, Hanna E. Manninen, Tuukka Petäjä, Yrjo Viisanen, and Markku Kulmala. Responses of the atmospheric concentration of radon-222 to the vertical mixing and spatial transportation. *Boreal Environment Research*, 21:299–318, 2016.

[85] A. Caciolli, M. Baldoncini, G. P. Bezzon, C. Broggini, G. P. Buso, I. Callegari, T. Colonna, G. Fiorentini, E. Guastaldi, F. Mantovani, G. Massa, R. Menegazzo, L. Mou, C. Rossi Alvarez, M. Shyti, A. Zanon, and G. Xhixha. A new fsa approach for in situ gamma ray spectroscopy. *Science of The Total Environment*, 414(0):639–645, 2012.

[86] A. Caciolli, M. Baldoncini, G. P. Bezzon, C. Broggini, G. P. Buso, I. Callegari, T. Colonna, G. Fiorentini, E. Guastaldi, F. Mantovani, G. Massa, R. Menegazzo, L. Mou, C. Rossi Alvarez, M. Shyti, A. Zanon, and G. Xhixha. A new fsa approach for in situ γ ray spectroscopy. *Science of The Total Environment*, 414(0):639–645, 2012.

[87] Gerti Xhixha, Matteo Alberi, Marica Baldoncini, Kozeta Bode, Elida Bylyku, Florinda Cfarku, Ivan Callegari, Fadil Hasani, Sheldon Landsberger, Fabio Mantovani, Eva Rodriguez, Ferat Shala, Virginia Strati, and Merita Xhixha Kaçeli. Calibration of hpge detectors using certified reference materials of natural origin. *Journal of Radioanalytical and Nuclear Chemistry*, 2015.

[88] L. Casini, Stefano Cuccuru, Matteo Maino, Giacomo Oggiano, Antonio Puccini, and Philippe Rossi. Structural map of variscan northern sardinia (italy). *Journal of Maps*, 11(1):75–84, 2015.

[89] M. Maino, L. Casini, A. Ceriani, A. Decarlis, A. Di Giulio, S. Seno, M. Setti, and F. M. Stuart. Dating shallow thrusts with zircon (u-th)/he thermochronometry–the shear heating connection. *Geology*, 43(6):495–498, 2015.

[90] Xian-Hua Li, Michel Faure, and Wei Lin. From crustal anatexis to mantle melting in the variscan orogen of corsica (france): Sims u–pb zircon age constraints. *Tectonophysics*, 634(0):19–30, 2014.

[91] O. Lexa, K. Schulmann, V. JanouŠEk, P. ŠTÍPskÁ, A. Guy, and M. Racek. Heat sources and trigger mechanisms of exhumation of hp

granulites in variscan orogenic root. *Journal of Metamorphic Geology*, 29(1):79–102, 2011.

[92] Fernando Bea. The sources of energy for crustal melting and the geochemistry of heat-producing elements. *Lithos*, 153:278–291, 2012.

[93] Cecilia Pérez-Soba, Carlos Villaseca, David Orejana, and Teresa Jeffries. Uranium-rich accessory minerals in the peraluminous and perphosphorous belvís de monroy pluton (iberian variscan belt). *Contributions to Mineralogy and Petrology*, 167(5), 2014.

[94] Romain Tartèse, Philippe Boulvais, Marc Poujol, and Jean-Louis Vigneresse. Granite petrogenesis revealed by combined gravimetric and radiometric imaging. *Tectonophysics*, 501(1-4):98–103, 2011.

[95] Borexino Collaboration. Spectroscopy of geoneutrinos from 2056 days of borexino data. *Physical Review D*, 92(3), 2015.

[96] M. Coltorti, R. Boraso, F. Mantovani, M. Morsilli, G. Fiorentini, A. Riva, G. Rusciadelli, R. Tassinari, C. Tomei, G. Di Carlo, and V. Chubakov. U and th content in the central apennines continental crust: A contribution to the determination of the geo-neutrinos flux at lngs. *Geochimica et Cosmochimica Acta*, 75(9):2271–2294, 2011.

[97] F. Bochicchio, G. Campos-Venuti, S. Piermattei, C. Nuccetelli, S. Risica, L. Tommasino, G. Torri, M. Magnoni, G. Agnesod, G. Sgorbati, M. Bonomi, L. Minach, F. Trotti, M. R. Malisan, S. Maggiolo, L. Gaidolfi, C. Giannardi, A. Rongoni, M. Lombardi, G. Cherubini, S. D'Ostilio, C. Cristofaro, M. Pugliese, V. Martucci, A. Crispino, P. Cuzzocrea, A. Sansone Santamaria, and M. Cappai. Annual average and seasonal variations of residential radon concentration for all the italian regions. *Radiation Measurements*, 40(2-6):686–694, 2005.

[98] Ivan Callegari, Gian Pietro Bezzon, Carlo Broggini, Gian Paolo Buso, Antonio Caciolli, Luigi Carmignani, Tommaso Colonna, Giovanni Fiorentini, Enrico Guastaldi, Merita Kaçeli Xhixha, Fabio Mantovani, Giovanni Massa, Roberto Menegazzo, Liliana Mou, Altair Pirro, Carlos Rossi Alvarez, Virginia Strati, Gerti Xhixha, and Alessandro Zanon. Total natural radioactivity, tuscany, italy. *Journal of Maps*, 9(3):438 – 443, 2013.

[99] F. Finger, M. P. Roberts, B. Haunschmid, A. Schermaier, and H. P. Steyrer. Variscan granitoids of central europe: their typology, potential sources and tectonothermal relations. *Mineralogy and Petrology*, 61(1-4):67–96, 1997.

[100] Michel Corsini and Yann Rolland. Late evolution of the southern european variscan belt: Exhumation of the lower crust in a context of oblique convergence. *Comptes Rendus Geoscience*, 341(2-3):214–223, 2009.

[101] L. Casini, Stefano Cuccuru, Matteo Maino, Giacomo Oggiano, and Massimo Tiepolo. Emplacement of the arzachena pluton (corsica–sardinia batholith) and the geodynamics of incoming pangaea. *Tectonophysics*, 544–545(0):31–49, 2012.

[102] Philippe Rossi and Alain Cocherie. Genesis of a variscan batholith: Field, petrological and mineralogical evidence from the corsica-sardinia batholith. *Tectonophysics*, 195(2–4):319–346, 1991.

[103] B. Bonin. A-type granites and related rocks: Evolution of a concept, problems and prospects. *Lithos*, 97(1-2):1–29, 2007.

[104] Gabriele Cruciani, Marcello Franceschelli, Hans-Joachim Massonne, Rodolfo Carosi, and Chiara Montomoli. Pressure–temperature and deformational evolution of high-pressure metapelites from variscan ne sardinia, italy. *Lithos*, 175–176:272–284, 2013.

[105] Don L. Anderson. Speculations on the nature and cause of mantle heterogeneity. *Tectonophysics*, 416(1-4):7–22, 2006.

[106] A. Gerdes, G. Worner, and A. Henk. Post-collisional granite generation and ht-lp metamorphism by radiogenic heating: the variscan south bohemian batholith. *Journal of the Geological Society*, 157(3):577–587, 2000.

[107] S Barca, L Carmignani, G Oggiano, PC Pertusati, I Salvatori, and L Carmignani. Carta geologica della sardegna, servizio geologico nazionale. *Litografia Artistica Cartografica, Firenze*, 1996.

[108] G. Xhixha, G. P. Bezzon, C. Broggini, G. P. Buso, A. Caciolli, I. Callegari, S. Bianchi, G. Fiorentini, E. Guastaldi, M. Kaçeli Xhixha, F. Mantovani, G. Massa, R. Menegazzo, L. Mou, A. Pasquini, C. Rossi Alvarez, and M. Shyti. The worldwide norm production and a fully automated gamma-ray spectrometer for their characterization. *Journal of Radioanalytical and Nuclear Chemistry*, 295(1):445–457, 2013.

[109] IAEA. Guidelines for radioelement mapping using gamma ray spectrometry data. IAEA-TECDOC-1363, 2003.

[110] J. Deraisme and M. Strydom. Estimation of iron ore resources integrating diamond and percussion drillholes. In *APCOM*.

[111] Roberta L. Rudnick and S. Gao. Composition of the continental crust, 2003.

[112] Tsoulfanidis N. and Landsberger S. *Measurement and Detection of Radiation, Fourth Edition.* Boca Raton, FL: CRC Press, Taylor and Francis Group, 2015.

[113] Tumsavas Z Kucuk N and Cakir. Determining photon energy absorption parameters for different soil samples. *J. Radiat.*, 54:578–586, 2013.

[114] Moshonas N Yiasemides Adamides E, Koutroubas S. Gamma-ray attenuation measurements as a laboratory experiment: some remarks. *Phys. Educ*, 46:398–402, 2011.

[115] IAEA. *Radioelement mapping.* IAEA nuclear energy series No. NF-T-1.3 Vienna, 2010.

[116] Minty B Nicolet JP Reford WS Erdi-Krausz G, Matolin M and Schetselaar. *Guidelines for radioelement mapping using gamma ray spectrometry data.* International Atomic Energy Agency (IAEA), 2003.

[117] David Filiberto Michelle Newton Benjamin Wolfe Elizabeth Karabinakis Steven Clark Elaine Poon Elizabeth Abbett David Pimentel, Bonnie Berger and Sudha Nandagopal. Water resources: Agricultural and environmental issues. *BioScience*, 2004.

[118] Marco Bittelli. Measuring soil water content: A review. *Hort Technology*, 21(3):293–300, 2011.

[119] M. K. Shukla. *Soil physics: An introduction.* CRC Press, 2013.

[120] R. Lal and M. Shukla. *Principles of Soil Physics.* CRC Press, 2004.

[121] D. Hillel. *Introduction to environmental soil physics.* Academic press, 2003.

[122] WI Madison. *Soil Science Society of America, Ed., Glossary of soil science terms.* Soil Science Society of America, 2008.

[123] P. A. Domenico and F. W. Schwartz. *Physical and chemical hydrogeology, 2nd ed.* New York: Wiley, 1998.

[124] D. Raes R. G. Allen, L. S. Pereira and M. Smith. Crop evapotranspiration-guidelines for computing crop water requirements-fao irrigation and drainage paper 56'. *FAO Rome*, 300(9):D05109, 1998.

[125] THOMAS R. CARROL L. Airborne soil moisture measurement using natural terrestrial gamma radiation. *Soil Science*, 132(5), 1981.

[126] L. Loevborg. Design and use of concrete pads for the calibration of radiometric survey instrumentation. *International Atomic Energy Agency (IAEA)*, 1984.

[127] Katsuhiro Yoshioka. Study of time variation of terrestrial gamma radiation due to depth distribution of soil moisture content. *Radioisotopes*, 1994.

[128] Alexis L. Coplin Terry D. Melendy Jay L. Clausen, Terrance Sobecki and Troy Arnold. Passive gamma-ray emission for soil-disturbance detection. *U.S. Army Engineer Research and Development Center Hanover United States*, 2016.

[129] Dan G. Blumberg Alexey Kotlyar Valentin Freilikher Leonid Vulfson, Arthur Genis and Jiftah Ben-Asher. Remote sensing in microwave and gamma ranges for the monitoring of soil water content of the root zone. *International Journal of Remote Sensing*, 2013.

[130] Netsens s.r.l., user guide meteosense 2.0. `http://www.netsens.it/`. Accessed: Nov-2017.

[131] Bryan Minty. Fundamentals of airborne gamma-ray spectrometry. *AGSO Journal of Australian Geology and Geophysics*, 17(2):39–50, 1997.

[132] F.Li J.M.Norman W.P.Kustas H.Jayanthi J.Chavez M.C.Anderson, C.M.U.Neale. Upscaling ground observations of vegetation water content, canopy height, and leaf area index during smex02 using aircraft and landsat imagery. *Remote Sensing of Environment*, 92, 2004.

[133] Ep Heuvelink Tao Li and Leo F. M. Marcelis. Quantifying the source–sink balance and carbohydrate content in three tomato cultivars. *Frontiers in Plant Science*, 6, 2015.

[134] Fausto Tomei Pier Paolo Roggero Roberto Orsini Marco Toderi Gabriele Antolini Marco Bittelli, Alberto Pistocchi and Markus Flury. *Soil hydrology, land use and agriculture: measurement and modelling*, chapter 11, pages 253–266. 2011.

[135] Dirk Raesc Pasquale Steduto, Theodore C. Hsiaob and Elias Fereresd. Aquacrop—the fao crop model to simulate yield response to water: I. concepts and underlying principles. *Agronomy Journal*, 101(3), 2008.

[136] J.S. Romberger K. E. Saxton, W.J. Rawls and R.I. Papendick. Estimating generalized soil-water characteristics from texture. *Soil. Sci. Soc. Am. J.*, 1982.

Appendices

Appendix A

For the flights with data under 340 m are shown the values of the linear regressions between each pair of sensors in the DATASET 2α: m (slope) and q (y-intercept) with their uncertainties and the r^2 (correlation coefficient). The sensors on the first row of each table give us the x values and the sensors on the first column give the y values.

Table 1: Linear regression data of F11 (DATASET 2α)

		GPSB	GPSA	GPSIMU	ALT	PT	PTIMU
GPSC	m	0.994 ± 0.002	0.992±0.003	0.981±0.003	0.987±0.002	0.996±0.003	1.001±0.003
	q	0.21 ± 0.38	-1.56±0.49	2.62±0.58	1.72±0.39	0.48±0.51	0.05±0.55
	r^2	0.998	0.997	0.996	0.998	0.997	0.996
GPSB	m		0.998±0.003	0.987±0.003	0.993±0.002	1.001±0.003	1.007±0.003
	q		1.46±0.44	2.49±0.51	1.63±0.33	-0.43±0.52	0.00±0.56
	r^2		0.998	0.997	0.999	0.997	0.996
GPSA	m			0.988±0.003	0.993±0.002	1.001±0.003	1.008±0.003
	q			1.28±0.545	0.40±0.36	-0.85±0.49	-1.31±0.51
	r^2			0.996	0.998	0.997	0.997
GPSIMU	m				1.003±0.003	1.012±0.002	1.019±0.002
	q				-0.48±0.46	-1.95±0.37	-2.42±0.38
	r^2				0.997	0.998	0.998
ALT	m					1.008±0.002	1.014±0.003
	q					-1.20±0.40	-1.63±0.46
	r^2					0.998	0.997
PT	m						1.007±0.001
	q						0.44±0.19
	r^2						1.000

Table 2: Linear regression data of F12 (DATASET 2α)

		GPSB	GPSA	GPSIMU	ALT	PT	PTIMU
GPSC	m	1.016 ± 0.005	0.996±0.006	1.015±0.006	1.056±0.007	1.015±0.007	0.998±0.007
	q	-2.67 ± 0.81	1.15±1.01	-3.65±1.01	-9.25±1.27	-1.70±1.25	0.28±1.21
	r^2	0.997	0.995	0.995	0.993	0.993	0.993
GPSB	m		0.980±0.004	0.998±0.005	1.037±0.008	0.997±0.007	0.981±0.007
	q		3.80±0.70	-0.77±0.90	-6.08±1.36	1.25±1.25	3.18±1.19
	r^2		0.998	0.996	0.992	0.993	0.993
GPSA	m			1.017±0.005	1.057±0.007	1.016±0.008	1.000±0.007
	q			-4.43±0.95	-9.93±1.33	-2.27±1.38	-0.35±1.28
	r^2			0.996	0.993	0.991	0.992
GPSIMU	m				1.036±0.008	1.000±0.004	0.983±0.003
	q				-4.90±1.42	1.98±0.75	3.85±0.63
	r^2				0.991	0.997	0.998
ALT	m					0.957±0.008	0.941±0.008
	q					7.96±1.38	9.92±1.41
	r^2					0.99	0.99
PT	m						0.983±0.002
	q						2.07±0.44
	r^2						0.999

Table 3: Linear regression data of F15 (DATASET 2α)

		GPSB	GPSA	GPSIMU	ALT	PT	PTIMU
GPSC	m	0.896 ± 0.017	0.956±0.008	1.015±0.014	0.982±0.007	0.991±0.027	1.022±0.026
	q	5.68 ± 0.89	0.65±0.43	-7.34±0.82	3.65±0.35	3.92±1.32	3.14±1.25
	r^2	0.958	0.992	0.978	0.994	0.928	0.962
GPSB	m		1.027±0.019	1.108±0.016	1.057±0.019	1.079±0.031	1.113±0.030
	q		-3.47±1.05	-13.05±0.95	-0.34±0.92	-0.63±1.50	-1.51±1.41
	r^2		0.958	0.975	0.964	0.968	0.921
GPSA	m			1.054±0.017	1.022±0.008	1.032±0.028	1.061±0.028
	q			-7.89±0.97	3.37±0.40	3.36±1.38	2.97±1.35
	r^2			0.971	0.993	0.916	0.922
GPSIMU	m				0.952±0.11	0.970±0.025	1.001±0.023
	q				11.57±0.54	11.38±1.21	10.57±1.11
	r^2				0.984	0.927	0.939
ALT	m					1.009±0.027	1.040±0.026
	q					0.33±1.31	-0.45±1.24
	r^2					0.921	0.931
PT	m						1.020±0.009
	q						-0.28±0.45
	r^2						0.99

Appendix B

For the flights with data over 340 m are shown the values of the linear regressions between each pair of sensors in the DATASET 2β: m (slope) and q (y-intercept) with their uncertainties and the r^2 (correlation coefficient). The sensors on the first row of each table give us the x values and the sensors on the first column give the y values.

Table 4: Linear regression data of F11 (DATASET 2β)

		GPSB	GPSA	GPSIMU	PT	PTIMU
GPSC	m	0.9996 ± 0.0001	1.0007±0.0001	1.0009±0.0002	0.9994±0.0002	0.9987±0.0002
	q	0.75 ± 0.11	0.11±0.14	0.15±0.21	1.57±0.24	3.50±0.27
	r^2	1.000	1.000	1.000	1.000	1.000
GPSB	m		1.0011±0.0002	1.0013±0.0001	0.9998±0.0002	0.9992±0.0002
	q		-0.64±0.18	-0.60±0.16	0.82±0.21	2.75±0.23
	r^2		1.000	1.000	1.000	1.000
GPSA	m			1.0002±0.0002	0.9987±0.0003	0.9980±0.0003
	q			0.05±0.28	1.48±0.30	3.40±0.33
	r^2			1.000	1.000	1.000
GPSIMU	m				0.9985±0.0001	0.9979±0.0001
	q				1.41±0.12	3.34±0.11
	r^2				1.000	1.000
PT	m					0.9994±0.0001
	q					1.93±0.11
	r^2					1.000

Table 5: Linear regression data of F14 (DATASET 2β)

		GPSB	GPSA	GPSIMU	PT	PTIMU
GPSC	m	0.99997 ± 0.00005	0.9996±0.0001	0.9977±0.0001	0.9975±0.0002	0.9982±0.0002
	q	0.18 ± 0.08	0.65±0.10	5.64±0.20	4.25±0.26	3.37±0.24
	r^2	1.000	1.000	1.000	1.000	1.000
GPSB	m		0.9996±0.0004	0.9977±0.0001	0.9976±0.0002	0.9982±0.0002
	q		0.44±0.06	5.47±0.22	4.07±0.28	3.19±0.25
	r^2		1.000	1.000	1.000	1.000
GPSA	m			0.9981±0.0001	0.9980±0.0002	0.9986±0.0002
	q			5.03±0.21	3.63±0.29	2758±0.25
	r^2			1.000	1.000	1.000
GPSIMU	m				0.9998±0.0001	1.0005±0.0001
	q				-1.40±0.21	-2.28±0.18
	r^2				1.000	1.000
PT	m					1.0007±0.0001
	q					-0.87±0.17
	r^2					1.000

Appendix C

The purpose of this appendix is to investigate the possibility of inferring the cosmic effective dose starting from a direct count rate measurement performed with an AGRS detector. In Fig. 1 we report the CED, calculated with the CARI-6P and EXPACS dosimetry softwares as function of the measured $\mathrm{n}^{\mathrm{CEW}}$, together with the linear fitting curves defined according to the following equation:

$$CED = a_{CED} + b_{CED} n^{CEW} \tag{17}$$

An excellent linear relation between CED and $\mathrm{n}^{\mathrm{CEW}}$ characterized by a r^2 coefficient of determination greater than 0.99 is observed for both dosimetry tools.

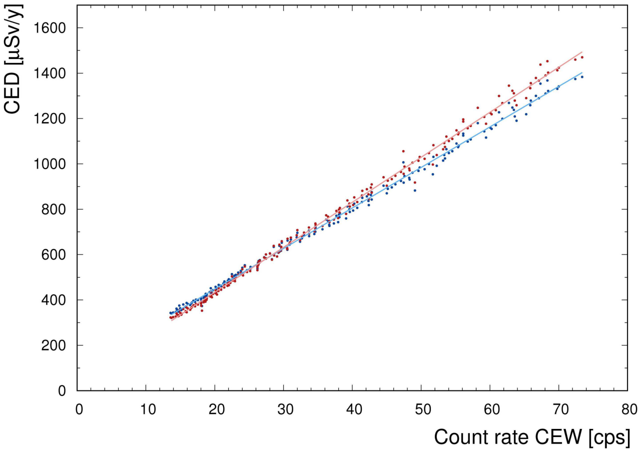

Figure 1: CED obtained by running the CARI-6P (blue points) and the EXPACS (red points) softwares with fixed location (Viareggio, 43°56'N - 10°14'E) and fixed date (31 March 2016) corresponding to the data taking conditions versus the experimental CR in the CEW. The linear fitting curves (see Eq. 17) have best fit parameters equal to a_{CED} = (90.9 ± 3.1) μSv/y and b_{CED} = (17.9 ± 0.1) μSv/(y·cps) for CARI-6P (light blue solid line) and a_{CED} = (36.6 ± 3.4) μSv/y and b_{CED} = (19.9 ± 0.1) μSv/(y·cps) for EXPACS (light red solid line).

With the purpose of testing how a change of latitude in AGRS surveys could affect the CED estimation, we reconstruct the $\mathrm{CED}^{\mathrm{EMS}}$/CED ratios along a meridian at different altitudes. In Fig. 2 we show the $\mathrm{CED}^{\mathrm{EMS}}$/CED ratios calculated with the CARI-6P and EXPACS dosimetry softwares as function of the geographic latitudes in the (0 - 3000) m range. In both cases it is possible to observe that the ratio generally increases for increasing altitude and that it reaches a plateau for latitudes greater than 50°. For varying solar activities, the calculated CED^{EMS}/CED profiles follow the same trends with a negligible variation with respect to the medium solar activity scenario of Fig. 2. Finally, as the CED^{EMS}/CED profile is reasonably smooth in the typical AGRS altitude range (z $<$ 200 m), this evidence adds a point in favor of the presented method for the estimation of the CED by using direct gamma-ray measurements.

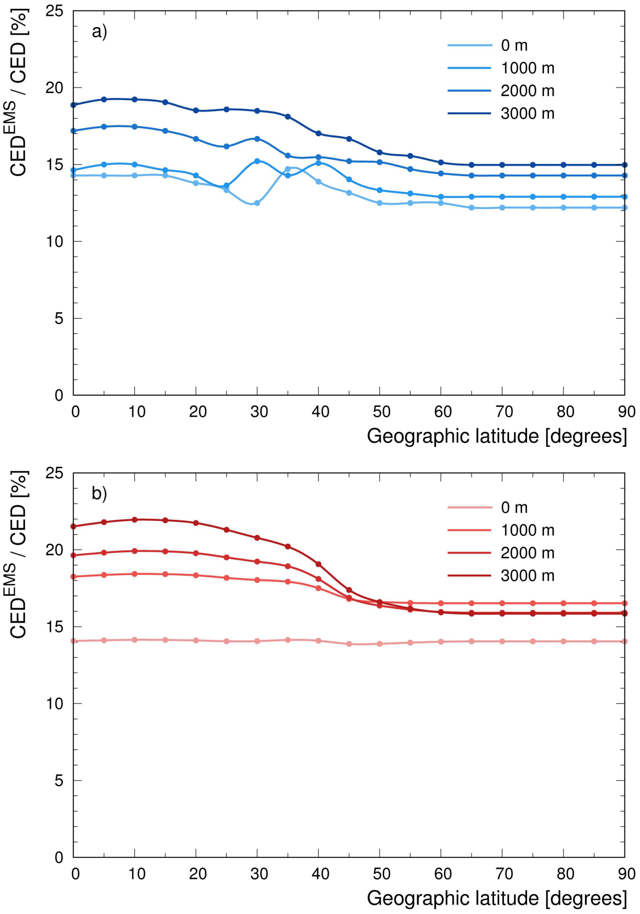

Figure 2: CED^{EMS}/CED ratios as function of the geographic latitude calculated for a medium solar activity (31 March 2016) and for four different altitudes (0 m, 1000 m, 2000 m and 3000 m) by using the CARI-6P (panel a) and the EXPACS (panel b) dosimetry tools.

Appendix D

Table 6: rainfall event table.

Date	Start time [hh:mm]	End time [hh:mm]	Total time [hh:mm]	[mm]
05/04/2017	05:00:00	06:00:00	1	0.25
07/04/2017	07:00:00	08:00:00	1	0.2
12/04/2017	06:00:00	07:00:00	1	0.2
16/04/2017	23:00:00	02:00:00	3	8
17/04/2017	03:00:00	04:00:00	1	0.25
18/04/2017	07:00:00	08:00:00	1	0.2
18/04/2017	12:00:00	16:00:00	4	9
18/04/2017	17:00:00	12:00:00	3	8.25
18/04/2017	19:00:00	20:00:00	1	4.4
27/04/2017	04:00:00	07:00:00	3	4
27/04/2017	21:00:00	00:00:00	3	7.75
28/04/2017	05:00:00	06:00:00	1	0.2
01/05/2017	16:00:00	17:00:00	1	0.75
03/05/2017	02:00:00	03:00:00	1	0.25
04/05/2017	03:00:00	05:00:00	2	2
04/05/2017	12:00:00	13:00:00	1	0.75
04/05/2017	14:00:00	15:00:00	1	0.75
04/05/2017	23:00:00	00:00:00	1	6.25
05/05/2017	01:00:00	03:00:00	2	1.25
06/05/2017	04:00:00	05:00:00	1	0.2
06/05/2017	16:00:00	02:00:00	10	40.25
07/05/2017	11:00:00	16:00:00	5	5
08/05/2017	13:00:00	14:00:00	1	0.2
27/05/2017	10:00:00	12:00:00	3	4.25
04/06/2017	13:00:00	15:00:00	2	0.5
19/06/2017	12:00:00	13:00:00	1	0.25
25/06/2017	13:00:00	15:00:00	2	3.75
27/06/2017	09:00:00	10:00:00	1	0.25
27/06/2017	16:00:00	18:00:00	2	1
28/06/2017	13:00:00	15:00:00	2	1.75
28/06/2017	16:00:00	17:00:00	1	0.25
28/06/2017	18:00:00	21:00:00	3	15.25
29/06/2017	03:00:00	04:00:00	1	0.25
29/06/2017	10:00:00	11:00:00	1	0.2
11/07/2017	15:00:00	16:00:00	1	0.75
11/07/2017	17:00:00	19:00:00	2	22.75
06/08/2017	18:00:00	21:00:00	3	18.25
10/08/2017	13:00:00	15:00:00	2	13
01/09/2017	04:00:00	10:00:00	6	9
02/09/2017	12:00:00	13:00:00	1	0.25
02/09/2017	20:00:00	23:00:00	2	4.5
02/09/2017	22:00:00	23:00:00	1	3.2
03/09/2017	02:00:00	04:00:00	2	2
07/09/2017	23:00:00	01:00:00	2	5.5
08/09/2017	06:00:00	07:00:00	1	0.25
09/09/2017	22:00:00	14:00:00	16	63.75
11/09/2017	02:00:00	04:00:00	2	0.5
11/09/2017	10:00:00	11:00:00	1	0.25
12/09/2017	04:00:00	05:00:00	1	0.2
12/09/2017	10:00:00	11:00:00	1	0.25
13/09/2017	06:00:00	07:00:00	1	0.2
15/09/2017	20:00:00	22:00:00	2	0.5
16/09/2017	00:00:00	03:00:00	3	1.25
16/09/2017	08:00:00	09:00:00	1	0.25
18/09/2017	15:00:00	17:00:00	2	0.75
18/09/2017	18:00:00	13:00:00	19	28.75
20/09/2017	01:00:00	03:00:00	2	0.75
24/09/2017	12:00:00	14:00:00	2	9
26/09/2017	03:00:00	04:00:00	1	0.25
01/10/2017	10:00:00	15:00:00	5	0.75
06/10/2017	16:00:00	20:00:00	4	19
11/10/2017	08:00:00	09:00:00	1	0.25
14/10/2017	08:00:00	09:00:00	1	0.25
18/10/2017	03:00:00	04:00:00	1	0.25
18/10/2017	10:00:00	11:00:00	1	0.25
22/10/2017	22:00:00	23:00:00	1	0.5
23/10/2017	02:00:00	03:00:00	1	0.75

Table 7: abundance and activity for the 19 samples taken 30/03/2017 analyzed with HPGe.

ID	Mass[g]	Act ^{40}K [Bq/kg]	Ab ^{40}K [%]	Act ^{214}Bi [Bq/kg]	Ab eU [ppm]	Act ^{208}Tl [Bq/kg]	Ab eTh[ppm]
B01	190.36	539.87 ± 34.68	1.72 ± 0.11	33.75 ± 3.28	2.73 ± 0.27	43.09 ± 3.73	10.61 ± 0.92
B02	180.08	559.31 ± 36.02	1.79 ± 0.12	31.03 ± 3.17	2.51 ± 0.26	37.17 ± 3.56	9.16 ± 0.88
B03	180.38	522.71 ± 33.99	1.67 ± 0.11	34.37 ± 3.39	2.78 ± 0.27	41.95 ± 3.78	10.33 ± 0.93
B04	220.29	534.84 ± 33.87	1.71 ± 0.11	36.76 ± 3.48	2.98 ± 0.28	45.21 ± 3.77	11.14 ± 0.93
B05	234.09	558.56 ± 34.98	1.78 ± 0.11	29.09 ± 2.9	2.36 ± 0.23	40.74 ± 3.48	10.03 ± 0.86
B06	215.52	575.01 ± 36.14	1.84 ± 0.12	31.77 ± 3.1	2.57 ± 0.25	43.67 ± 3.63	10.76 ± 0.89
B07	189.85	520.97 ± 33.7	1.66 ± 0.11	31.00 ± 3.15	2.51 ± 0.26	37.50 ± 3.56	9.24 ± 0.88
B08	206.46	480.9 ± 31.25	1.54 ± 0.1	32.14 ± 3.11	2.6 ± 0.25	40.95 ± 3.63	10.09 ± 0.89
B09	206.46	447.48 ± 29.36	1.43 ± 0.09	31.07 ± 3.07	2.52 ± 0.25	37.13 ± 3.45	9.15 ± 0.85
B10	195.67	510.8 ± 33.07	1.63 ± 0.11	31.02 ± 3.08	2.51 ± 0.25	38.38 ± 3.5	9.45 ± 0.86
B11	214.32	402.13 ± 26.81	1.28 ± 0.09	25.80 ± 2.72	2.09 ± 0.22	29.44 ± 2.97	7.25 ± 0.73
B12	209.07	459.33 ± 29.99	1.47 ± 0.1	34.07 ± 3.31	2.76 ± 0.27	34.75 ± 3.24	8.56 ± 0.80
B13	203.71	556.61 ± 35.38	1.78 ± 0.11	33.16 ± 3.22	2.69 ± 0.26	38.63 ± 3.48	9.51 ± 0.86
B14	197.04	458.09 ± 30.25	1.46 ± 0.1	27.19 ± 2.76	2.2 ± 0.22	38.86 ± 3.54	9.57 ± 0.87
B15	213.64	433.01 ± 28.53	1.38 ± 0.09	25.18 ± 2.63	2.04 ± 0.21	34.77 ± 3.22	8.56 ± 0.79
B16	212.43	557.57 ± 35.32	1.78 ± 0.11	31.28 ± 3.13	2.53 ± 0.25	36.48 ± 3.33	8.99 ± 0.82
B17	200.07	467.29 ± 30.58	1.49 ± 0.1	26.97 ± 2.83	2.18 ± 0.23	35.62 ± 3.49	8.77 ± 0.86
B18	211.2	0474.45 ± 30.84	1.52 ± 0.1	29.68 ± 3.01	2.4 ± 0.24	30.84 ± 3.14	7.60 ± 0.77
B19	204.27	521.02 ± 33.38	1.66 ± 0.11	33.00 ± 3.24	2.67 ± 0.26	45.4 ± 3.84	11.18 ± 0.95
Mean	204.47	504.21	1.61	30.96	2.51	38.45	9.47
Median	206.40	520.97	1.66	31.07	2.52	38.38	9.45
STV	13.56	50.22	0.16	3.07	0.25	4.40	1.08

Table 8: result of the measure of water content on samples collected 24/07/2017

	Gravimetric water content [%]			**Volumetric water content [%]**		
ID	**0-10 cm**	**10-20 cm**	**20-30 cm**	**0-10 cm**	**10-20 cm**	**20-30 cm**
B-20	12	13	16	17	18	22
B-21	13	13	15	18	17	20
B-22	13	11	15	18	15	20
B-23	12	16	19	16	21	25
B-24	9	13	18	11	18	24
B-25	11	14	18	15	19	24
B-26	10	12	14	13	16	19
B-27	11	14	17	15	19	23
B-28	14	13	14	19	18	19
B-29	15	15	18	21	20	24
B-30	12	13	15	17	18	20
B-31	15	15	17	20	20	23
B-32	11	16	18	15	22	25
B-33	8	10	11	11	14	15
B-34	9	11	12	12	15	16
B-35	14	14	20	19	19	27
Mean	12	13	16	16	18	22
Median	12	13	17	16	18	22
STV	2	2	3	3	2	3

Table 9: result of the measure of water content on samples collected 26/07/2017.

	Gravimetric water content [%]			Volumetric water content [%]		
ID	**0-10 cm**	**10-20 cm**	**20-30 cm**	**0-10 cm**	**10-20 cm**	**20-30 cm**
C-20	18	17	18	25	22	24
C-21	21	17	19	28	23	26
C-22	19	18	20	26	24	27
C-23	19	19	19	26	25	25
C-24	21	22	19	28	29	25
C-25	24	24	19	32	33	26
C-26	22	18	19	30	24	26
C-27	20	18	16	26	24	21
C-28	15	16	17	21	22	23
C-29	23	19	20	31	25	27
C-30	21	19	20	28	26	26
C-31	19	18	21	25	24	28
C-32	20	18	20	27	25	27
C-33	21	17	16	28	22	22
C-34	18	15	14	25	20	19
C-35	20	16	14	27	22	19
Mean	20	18	18	27	24	24
Median	20	18	19	27	24	25
STV	2	2	2	3	3	3

Table 10: result of the measure of water content on samples collected 28/07/2017

	Gravimetric water content [%]			**Volumetric water content [%]**		
ID	**0-10 cm**	**10-20 cm**	**20-30 cm**	**0-10 cm**	**10-20 cm**	**20-30 cm**
D-20	12	16	19	17	21	25
D-21	15	16	18	20	21	25
D-22	15	17	19	20	24	25
D-23	16	17	19	21	23	25
D-24	13	15	15	18	20	20
D-25	13	14	14	18	19	19
D-26	12	14	14	17	19	19
D-27	15	17	19	20	23	25
D-28	7	14	16	10	19	22
D-29	15	17	19	21	23	25
D-30	15	18	20	20	24	27
D-31	13	17	19	18	23	25
D-32	15	16	18	20	22	24
D-33	16	18	19	21	24	25
D-34	13	13	13	17	17	18
D-35	11	12	13	15	17	17
Mean	14	16	17	18	21	23
Median	14	16	18	19	22	25
STV	2	2	2	3	2	3

Table 11: result of the measure of water content on samples collected 18/09/2017

ID	**Gravimetric water content** [%] **0-20 cm**	**Volumetric water content** [%] **0-20 cm**
E-20	16	21
E-21	16	21
E-22	15	20
E-23	16	22
E-24	16	21
E-25	15	21
E-26	17	24
E-27	17	22
E-28	18	24
E-29	17	23
E-30	16	21
E-31	17	23
E-32	16	22
E-33	16	22
E-34	16	22
E-35	16	22
Mean	18	24
Median	18	24
STV	1	2

Table 12: result of the measure of water content on samples collected 21/09/2017

ID	**Gravimetric water content [%]** **0-20 cm**	**Volumetric water content [%]** **0-20 cm**
F-20	17	23
F-21	18	24
F-22	17	23
F-23	19	26
F-24	16	22
F-25	17	23
F-26	19	25
F-27	18	24
F-28	20	27
F-29	19	25
F-30	18	24
F-31	17	23
F-32	16	22
F-33	16	22
F-34	18	24
F-35	17	23
Mean	18	24
Median	18	24
STV	1	2

Table 13: results of measurements carried out on samples collected on 18-09-2017, measurements made by ANALITICA S.a.s.

			Samples ID		
Major elements of oxides	**E 36** % by weight	**E 37** % by weight	**E 38** % by weight	**E 39** % by weight	**E 40** % by weight
Na_2O	0.96	0.91	0.95	0.98	0.99
MgO	2.83	2.91	2.83	2.81	2.84
Al_2O_3	11.66	11.73	11.73	11.75	11.8
SiO_2	55.42	55.19	55.49	55.91	56.59
P_2O_5	0.26	0.33	0.25	0.26	0.26
K_2O	2.05	2.04	2.11	2.07	2.13
CaO	9.72	9.63	9.57	9.66	9.51
TiO_2	0.49	0.53	0.51	0.51	0.51
MnO	0.12	0.12	0.12	0.11	0.12
Fe_2O_3	4.22	4.53	4.37	4.29	4.33
LOI	12.28	12.08	12.09	11.64	10.93